Numerical Methods for Hyperbolic Conservation Laws with a Discontinuous Flux Function

Master of Science Thesis in Reservoir Mechanics

Svenn Tveit

Center for Integrated Petroleum Research

Department of Mathematics
University of Bergen

June 2011

Acknowledgements

First of all I would like to thank my supervisor Ivar Aavatsmark for his help, and the time he has put into discussing the problems I encountered in my work. I am also grateful for advices he has given in my studies.
I would like to thank CIPR for giving me a place to read, and for supplies which made my master years much easier. I thank the CIPR administration for always being positive and accommodating.

The five years on the university would have been a boring experience without my fellow students. Especially, I would like to thank Kristian Fossum and Brede Rem Bergo for some really fun moments, and always being available for academical and non-academical discussions. To the rest of the students on CIPR: thank you!

Last, but not least, I would like to thank my parents for always being supportive, and my friends for taking my mind of the studies.

Svenn,
June 2011

Contents

Chapter 1

Introduction

Nonlinear, scalar conservation laws arise in several different physics and engineering problems. The classical theory on conservations laws includes a flux function only dependent on the conserved material (autonomous), but in many physical models this is not always the case. In general the flux function may depend on a spatial variable through a coefficient which can be discontinuous. Thus, the classical theory must be expanded to include such a discontinuous flux function. In this thesis the simplest case of spatial discontinuity is studied, namely the "two flux"-case. The flux function then consist of two autonomous flux functions separated at some spatial point. In addition to discontinuities occurring in the solution, the transition between the two flux functions generates a problem of finding a unique solution. Thus, several papers have been written addressing conservation laws with discontinuous flux. The paper by Adimurthi, Mishra and Gowda [3] is widely recognized for unifying the different theories proposed in previous papers. They noted that the solution of the conservation law with a spatial dependent flux function depends on the physical model it is derived from, even though the circumstances, mathematically speaking, may seem equal.

The application of the theory on physical models calls, in most cases, for numerical approximations. Hence, numerical methods have been developed to converge to the unique solution according to the established theory. Among the most widely used, and recognized schemes, is the Godunov and Engquist-Osher schemes. With novel modification, both of the schemes can be used to approximate the desired solution of conservation laws with discontinuous flux.

The physical model we study in this thesis is a heterogeneous two-phase flow in porous medium. When neglecting capillary pressure, the flow in a heterogeneous petroleum reservoir is modeled as a conservation law with discontinuous flux, representing the change in rock type. Numerically, the flux is commonly

approximated by the *Upstream Mobility flux*. This is an ad hoc flux approximation, made by petroleum engineers from physical consideration. Even so, the mathematical justification for using this approximation is found in [22], but only for homogeneous porous medium. Although the Upstream Mobility scheme has been studied in the heterogeneous case in [18], no mathematical proof of convergence could be made. Numerical experiments done by the authors suggested unphysical behavior of the scheme. These experiments simulated the simplest possible situation of vertical flow, only driven by gravity, in a core with changing rock type. The main focus of this thesis is the general Riemann problem associated with flow in porous medium, not only driven by gravity, but also inflow. Thus, we can evaluate the performance of the Upstream Mobility scheme in more relevant flow situations. To evaluate the performance, we compare the scheme with the Godunov and Engquist-Osher schemes, which have been modified to capture the physically relevant solution in two-phase flow.

We also introduce a new scheme for solving conservation laws with discontinuous flux. The scheme is a Lax-Friedrichs-type method called *Local Lax-Friedrichs' (Rusanov's) method*. It is well known that the regular Lax-Friedrichs scheme produces to much numerical dispersion when approximating even the simplest physical models to be of any practical use. Thus, we could not have hoped for good results if applied to e.g. heterogeneous two-phase flow. The Local Lax-Friedrichs scheme modifies the regular scheme such that the numerical dispersion is significantly less, at least in the homogeneous case (see [17] for comparison of Lax-Friedrichs and Local Lax-Friedrichs). In this thesis, we extend the scheme such that it is applicable for approximating conservation laws with discontinuous flux. We evaluate the performance of the scheme in the same numerical experiments as the Upstream mobility scheme.

The thesis consists of four chapters:

- In Chapter 2 we go through the theory on conservation laws with and without a spatially discontinuous flux function. The theory on conservation laws without the discontinuous flux is assumed familiar, and therefore only briefly discussed. Conservation laws with the discontinuous flux functions is not assumed familiar, thus more elaborate description of this theory is presented. Multiple examples is given for better understanding, and practical use of the theory.

- In Chapter 3 we present the numerical methods we will use in the experiments. The methods are: Godunov, Engquist-Osher, Local Lax-Friedrichs and Upstream Mobility. In addition, we check the properties of consistency and monotonicity for the Godunov, Engquist-Osher and Upstream Mobility scheme.

- In Chapter 4 the numerical experiments are presented. We focus on Riemann problems associated with heterogeneous two-phase flow in a porous medium.
- In Chapter 5 we sum up and make some final conclusions.

Chapter 2

Theory

In this chapter we go through some theory on scalar hyperbolic conservation laws, both *with* and *without* a discontinuous flux function. It is important to review the theory closely, due to the connection between the theory and the numerical methods . Numerical methods must meet the same properties as the partial differential equation (PDE), such as local conservation, entropy conditions and so forth. This is somewhat unique for hyperbolic conservation laws, in contrary to other PDEs. The first part of the chapter describes the properties and solution strategy for scalar hyperbolic conservation laws with a flux function without spatial discontinuity. The last part of the chapter focus on properties of the PDE when a spatial discontinuity in the flux functions is present.

2.1 Scalar Hyperbolic Conservation Laws *without* Spatial Discontinuity

Consider the hyperbolic PDE and corresponding initial condition

$$\begin{aligned} &u_t + f(u)_x = 0, \quad \text{for } (x,t) \in \Pi_T := \mathbb{R} \times (0,T)\,, \\ &u(x,0) = u_0(x), \quad \text{for } x \in \mathbb{R}\,,\ t = 0, \end{aligned} \tag{2.1.1}$$

where $u = u(x,t)$ is the conserved property and $f(u)$ is the nonlinear flux function, only depending on u. The initial condition $u_0(x)$ can be continuous or discontinuous. If a hyperbolic PDE is written in the form of (2.1.1), then it is called a *conservation law*.

2.1.1 Continuous and Weak Solutions

(2.1.1) can be modified and written on quasilinear form

$$u_t + f'(u)u_x = 0,$$

$f^{'}(u)$ is called the characteristic speed, and the characteristics are given as $x = \xi + f'(u)t$. By the *methods of characteristics*, the solution $u(x,t)$ to (2.1.1) is constant along the characteristics, and is therefore given by

$$u(x,t) = u_0(\xi) = u_0(x - f'(u)t). \tag{2.1.2}$$

This is called the *classical solution* of (2.1.1).

It is well known that even starting with smooth initial condition u_0, discontinuities in the solution can occur because of the nonlinear $f(u)$. These discontinuous solutions are called *shocks,* and is where the classical theory breaks down. Since the classical solution have to be C^1 (i.e. continuously differentiable), we have to avoid them by introducing weak solutions.

Definition 1. Weak solutions *A bounded measurable function, $u(x,t)$, is called a weak solution of* (2.1.1) *if it satisfies the integral identity*

$$\int\int_{\Pi_T} \left(u\phi_t + f(u)\phi_x\right) dxdt + \int_{\mathbb{R}} u_0(x)\phi(x,0)dx = 0, \tag{2.1.3}$$

for all test functions $\phi \in C_0^1(\Pi_T)$.

With this definition, the derivatives have been moved from u to the test function ϕ. The flux function must always be sufficiently smooth, i.e. Lipschitz continuous[1].

2.1.2 Rankine-Hugoniot and Entropy Conditions

To make sure that the conservation principle is preserved for discontinuous solutions, we have to impose some constrains on the solution. The first constraint ensures us that u is conserved through a shock solution, and the second constraint gives us a condition to obtain the physically correct weak solution.

[1] A function $f : X \to Y$ is called Lipschitz continuous if there exists a constant C such that for each $x, y \in X$ one has: $|f(x) - f(y)| \leq K|x - y|$

2.1.2.1 Rankine-Hugoniot Condition

By integrating (2.1.1) over a curve in the (x,t)-plane where $u(x,t)$ has a discontinuity, we can derive the following condition

Theorem 1. Rankine Hugoniot condition *Let u_L and u_R be values of $u(x,t)$ on the left and right side of the shock, respectively, and let σ be the shock velocity. A weak shock solution of* (2.1.1) *is only valid if*

$$\sigma(u_R - u_L) = f(u_R) - f(u_L) \tag{2.1.4}$$

A proof of the Rankine-Hugoniot condition is found in e.g. [17, 16, 1].

2.1.2.2 Entropy Condition

Generally, the weak solution is not unique and we need an additional constraint together with the Rankine-Hugoniot condition to single out the physically correct solution. Consider the second order PDE

$$u_t^\epsilon + f(u^\epsilon)_x = \epsilon g(u^\epsilon)_{xx}. \tag{2.1.5}$$

We want the solution in (2.1.5) to approach the solution in (2.1.1) as $\epsilon > 0$ tends to zero. $g(u^\epsilon)_{xx} = (g'(u^\epsilon)u_x^\epsilon)_x$ must satisfy $g'(u) \geq 0$ to get diffusion of u for growing t. We define the convex entropy function $\eta(u)$, such that $\eta''(u) \geq 0$ and the corresponding entropy flux function $\psi(u)$ satisfying $\psi'(u) = \eta'(u)f'(u)$. If we multiply (2.1.5) with $\eta'(u)$ we get with some manipulation

$$\eta(u^\epsilon)_t + \psi(u^\epsilon)_x = \epsilon\eta'(u^\epsilon)\, g(u^\epsilon)_{xx}. \tag{2.1.6}$$

If we integrate (2.1.6) and let $\epsilon \to 0$, we get the entropy inequality

$$\frac{d}{dt}\int_a^b \eta(u)dx + [\psi(u)]_a^b \leq 0, \tag{2.1.7}$$

which u must satisfy for all a and b that does not lie on a discontinuity curve in the (x,t)-plane.

The Kruzkov entropy function is defined by

$$\eta(u) = |u - c|, \tag{2.1.8}$$

the corresponding entropy flux function is

$$\psi(u) = sign(u - c)(f(u) - f(c)). \tag{2.1.9}$$

The entropy function, $\eta(u)$, satisfy the entropy inequality (2.1.7) even though it is not differentiable when $u = c$. Using the Kruzkov entropy functions in (2.1.7), we get the famous *Oleinik entropy condition.*

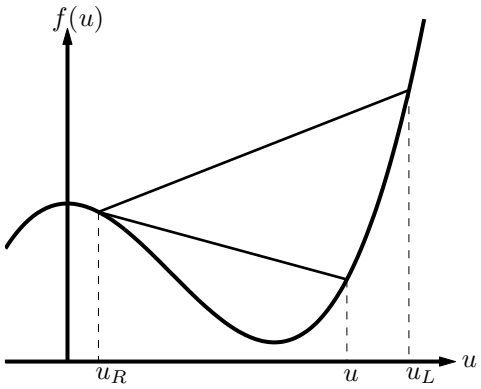

Figure 2.1.1: Allowed shock solution

Theorem 2. Oleinik entropy condition *A weak solution* $u(x,t)$ *is a entropy solution if the shock (with left value* u_L *and right value* u_R*) satisfy the Rankine-Hugoniot condition and the additional entropy condition*

$$\frac{f(u)-f(u_L)}{u-u_L} \geq \sigma \geq \frac{f(u)-f(u_R)}{u-u_R}, \tag{2.1.10}$$

where u *is between* u_L *and* u_R*, and* σ *is the shock velocity, which is given by* (2.1.4)*.*

This condition has a simple geometric interpretation. For a shock with left value u_L and right value u_R, the velocity, σ, is the slope of the line between $(u_L, f(u_L))$ and $(u_R, f(u_R))$ in the (u,f)-plane. The Oleinik entropy condition states that the slope of the line between $(u_R, f(u_R))$ and $(u, f(u))$ for u between u_L and u_R must always be less than the shock velocity. Figure 2.1.1 shows an example of the geometric interpretation of the Oleinik entropy condition.

A weaker condition than the Oleinik entropy condition can be obtained by letting $u \to u_L$ and $u \to u_R$ in (2.1.10) for the left and right inequality respectively

$$f'(u_L) \geq \sigma \geq f'(u_R). \tag{2.1.11}$$

This condition gives us important properties for the characteristics on each side of a shock. The characteristics can never go out of a shock, only go into or run parallel to it. In the part of this chapter where we look at conservation laws with spatial discontinuity, similar conditions like (2.1.11) will be discussed.

We finish this section by defining a general weak entropy solution. This is useful for later analysis, and generally it is used in developing entropy conditions for conservation laws. The definition is given as (see [13])

Definition 2. Kruzkov-type entropy inequality. *A weak solution $u(x,t)$ of 2.1.1 is called an entropy weak solution if, for any constant c and test functions $0 \leq \phi \in C_0^\infty(\Pi_T)$,*

$$\int\int_{\Pi_T} \left(|u-c|\,\phi_t + sign\,(u-c)\,(f(u)-f(c))\,\phi_x\right) dxdt \geq 0. \tag{2.1.12}$$

Note that Oleinik's entropy condition can be derived using 2.1.12. This is remarked under Definition 1 in [13].

2.1.3 The Riemann Problem

The initial value problems (IVP) of interest in this thesis is the *Riemann problem*. A Riemann problem is an IVP defined by the following

$$\begin{aligned} u_t + f(u)_x &= 0, \\ u(x,0) &= \begin{cases} u_L, & x < 0, \\ u_R, & x > 0. \end{cases} \end{aligned} \tag{2.1.13}$$

The solution of the Riemann problem is characterized by waves propagating from the origin with speed of x/t. With this knowledge, we use the ansatz $u(x,t) = u(x/t) = u(\zeta)$ in (2.1.13) and get the ordinary differential equation (ODE)

$$(f'(u) - \zeta)\,u_\zeta = 0, \tag{2.1.14}$$

where $u_\zeta = \partial u/\partial\zeta$. Boundary condition for (2.1.14) is

$$u(-\infty) = u_L, \qquad u(\infty) = u_R. \tag{2.1.15}$$

The solution to (2.1.14) and (2.1.15) consist of areas where either $u_\zeta = 0$ or $f'(u) = \zeta$. This gives us various waves where one has to account for shocks occurring in the solution. The different wave solutions are:

1. *Constant state.* The solution consists of areas where $u_\zeta \equiv 0$, that is $u(\zeta) = constant$.

2. *Rarefaction waves.* This is a solution where $f'(u) = \zeta$ or rather $u(\zeta) = (f')^{-1}(x/t)$. This solution is only unique when $f'(u)$ is a monotone increasing or decreasing function.

3. *Shock waves.* The solution is a discontinuity fulfilling the Rankine-Hugoniot condition (2.1.4) with shock velocity $\sigma = x/t$, and the Oleinik entropy condition holds with strict inequalities. With these two conditions, the solution is unique even when $f'(u)$ is not monotone.

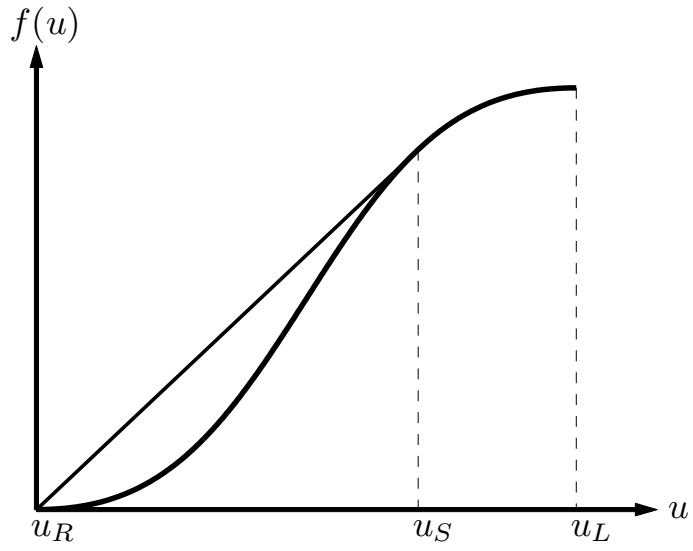

Figure 2.1.2: Flux function $f(u)$ with the solution drawn for example 1

4. *Contact discontinuity.* Fulfilling the same conditions as for shock waves, except the Oleinik entropy condition holds with strict equality.

The easiest way of solving a Riemann problem is by looking at $f(u)$ between u_L and u_R. For $u_L < u_R$ we create the largest convex function that lies under $f(u)$ for $u \in [u_L, u_R]$ called the *convex hull*, and for $u_R < u_L$ we create the least concave function that lies over $f(u)$ for $u \in [u_R, u_L]$, called the *concave hull*. If $f(u)$ is nonlinear, we have a rarefaction wave where the hulls coincides with $f(u)$ and shock waves where the hulls is a chord. When the solution goes from a rarefaction wave to a shock wave (or vice versa), the shock velocity must be equal to $f'(u)$ in the point of transition. If $f(u)$ is linear, the hulls will coincide with $f(u)$, creating contact discontinuities. The solution procedure is best illustrated with an example.

Example 1. Consider the Riemann problem (2.1.13) with $f(u)$ given as in figure 2.1.2. Since $u_R < u_L$ we create the concave hull from u_R to u_L. From u_R to u_S we have a shock wave, and from u_S to u_L the solution is a rarefaction wave. The shock velocity, given by (2.1.4), is

$$\sigma = \frac{f(u_R) - f(u_S)}{u_R - u_S} = \frac{f(u_S)}{u_S} = f'(u_s). \tag{2.1.16}$$

Summing up, the solution of (2.1.13) is

$$u(x,t) = \begin{cases} u_L, & x < 0, \\ (f')^{-1}\left(\frac{x}{t}\right), & 0 \le x \le f'(u_S)\, t\,, \\ u_R, & x > f'(u_S)\, t. \end{cases} \tag{2.1.17}$$

Figure 2.1.3 shows the initial value, solution and the characteristics.

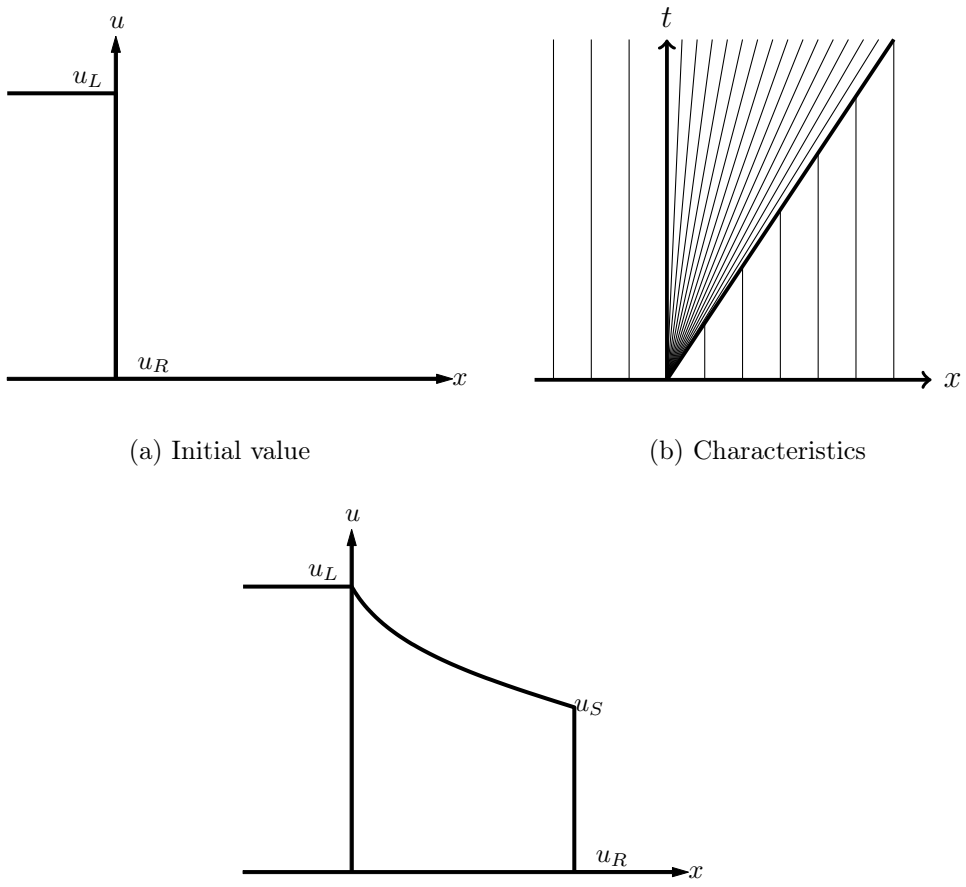

(a) Initial value

(b) Characteristics

(c) Solution

Figure 2.1.3: Solution to the Riemann problem (2.1.13) with the initial conditions given in figure 2.1.2

2.2 Scalar Hyperbolic Conservation Laws *with* Spatial Discontinuity

In this section we go through the theory on conservation laws with flux functions discontinuous in the spatial dimension. Most of the basic theory is taken from [3]. Here the authors have tried stringing together the numerous article written on the topic, and present a framework for entropy solutions.

2.2.1 Weak Solutions

We are interested in the scalar hyperbolic conservation law of the type

$$\begin{aligned} u_t + \left(H\left(x\right) f\left(u\right) + \left(1 - H\left(x\right)\right) g\left(u\right)\right)_x = 0, \quad & \text{for } \left(x,t\right) \in \Pi_T := \mathbb{R} \times \left(0,T\right), \\ u\left(x,0\right) = u_0\left(x\right), \quad & \text{for } x \in \mathbb{R}\,,\ t = 0, \end{aligned} \tag{2.2.1}$$

where $H\left(x\right)$ is the Heaviside function, f and g are Lipschitz continuous, nonlinear flux functions. Letting $F\left(x,u\right) := H\left(x\right) f\left(u\right) + \left(1 - H\left(x\right)\right) g\left(u\right)$, (2.2.1) can be written in a more compact form

$$u_t + F\left(x,u\right)_x = 0. \tag{2.2.2}$$

As for (2.1.1), discontinuous solutions can develop after a finite time, even for smooth u_0, and we have to seek solution to (2.2.1) in the weak form. Using definition 1, a weak solution to (2.2.1) must satisfy

$$\int\int_{\Pi_T} \left(u\phi_t + F\left(x,u\right)\phi_x\right) dxdt + \int_{\mathbb{R}} u_0(x)\phi(x,0)dx = 0, \tag{2.2.3}$$

for all test functions $\phi \in C_0^1\left(\Pi_T\right)$. With the above definition we can say that u satisfy (2.2.3) if and only if, in the weak sense u satisfies

$$\begin{aligned} u_t + g\left(u\right)_x = 0, \quad x < 0, \quad t > 0, \\ u_t + f\left(u\right)_x = 0, \quad x > 0, \quad t > 0. \end{aligned} \tag{2.2.4}$$

At $x = 0$, we must have mass conservation. That is, according to the Rankine-Hugoniot condition (2.1.4) with $\sigma = 0$, u must satisfy for almost all t

$$f\left(u^+\left(t\right)\right) = g\left(u^-\left(t\right)\right), \tag{2.2.5}$$

where $u^+\left(t\right) = \lim_{x \to 0^+} u\left(x,t\right)$ and $u^-\left(t\right) = \lim_{x \to 0^-} u\left(x,t\right)$.

In section 2.1.2.2 we got an entropy condition for the hyperbolic problem (2.1.1). This condition is not sufficient to guarantee uniqueness for (2.2.1), but it is natural to assume that this condition holds away from the interface ($x = 0$). This means that for each of the two conservation laws in (2.2.4), the Oleinik entropy condition (2.1.10) must hold in the regions $(-\infty, 0)$ and $(0, \infty)$. The following theorem clears up what the Oleinik entropy condition looks like in both regions [12]

Theorem 3. The interior entropy condition. *Let $u\left(x,t\right)$ be discontinuous at $\xi = x/t \neq 0$ and define u_L and u_R as left and right values of u at the discontinuity, respectively. Let $\sigma = x/t$ be the shock velocity. If $\sigma < 0$, then we define*

$$\sigma = \sigma_L = \frac{g\left(u_R\right) - g\left(u_L\right)}{u_R - u_L},$$

and if $\sigma > 0$ *we define*

$$\sigma = \sigma_R = \frac{f(u_R) - f(u_L)}{u_R - u_L},$$

A valid shock in region $(-\infty, 0)$ *must satisfy*

$$\frac{g(u) - g(u_L)}{u - u_L} \geq \sigma_L \geq \frac{g(u) - g(u_R)}{u - u_R}, \tag{2.2.6}$$

and in region $(0, \infty)$ *the shock must satisfy*

$$\frac{f(u) - f(u_L)}{u - u_L} \geq \sigma_R \geq \frac{f(u) - f(u_R)}{u - u_R}, \tag{2.2.7}$$

for all u *between* u_L *and* u_R.

Thus, if a shock is to be valid in region $(-\infty, 0)$ its speed has to be negative and satisfy (2.2.6), and similar for region $(0, \infty)$, a shock is valid only if its speed is positive and satisfy (2.2.7).
We are therefore left with defining an entropy condition *at* the interface ($x = 0$), and it is here several authors have different conditions giving different entropy solutions for (2.2.1). Following [3], we split the problem in two: constructing a general entropy framework and then defining which physical model you want the entropy solution for. In the next two sections, we investigate these two problems separately.

2.2.2 The Entropy Framework

We start off this section with some hypothesis on the flux functions ([2, 3]).

Hypotheses. Let f and g be Lipschitz continuous functions on $I = [s, S]$ satisfying

(H_1) $f(s) = g(s), \qquad f(S) = g(S).$

(H_2) f and g have only one global maximum and no local minimum in (s, S). We call these concave type fluxes ($CC(I)$).

(H_3) f and g have only one global minimum and no local maximum in (s, S). We call these convex type fluxes ($CV(I)$).

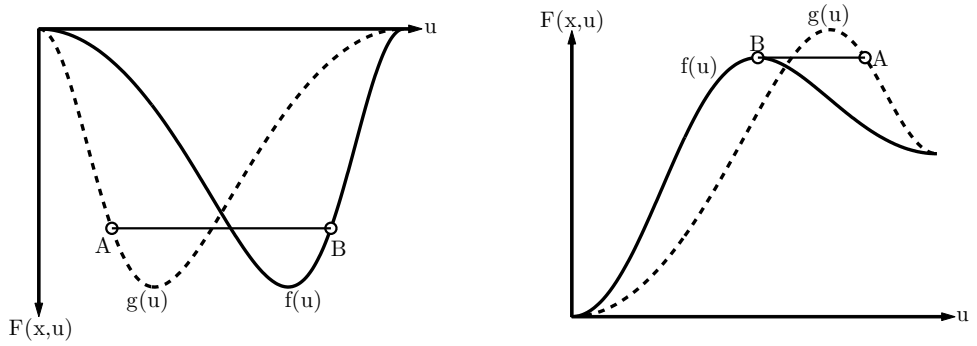

(a) An example of flux functions of type $CV(I)$ satisfying (H_1)

(b) An example of flux functions of type $CC(I)$ satisfying (H_1)

Figure 2.2.1: Flux functions satisfying definition 3

In figure 2.2.1, we see examples of flux functions satisfying either (H_2) or (H_3). Notice that (H_1) does not imply that the flux functions have the same value at s as in S, c.f. figure 2.2.1b. With these hypotheses on the flux functions we can continue with some definitions [3].

Definition 3. (A,B)-pair. *Let f and g satisfy (H_1, H_2) or (H_1, H_3) with θ_f and θ_g being the unique minimum or maximum, respectively. Then $(A, B) \in I$ is a connection if it satisfy the following*

1. $g(A) = f(B)$.
2. *For $f, g \in CV(I)$, $s \leq A \leq \theta_g$ and $\theta_f \leq B \leq S$.*
3. *For $f, g \in CC(I)$, $\theta_g \leq A \leq S$ and $s \leq B \leq \theta_f$.*

The definition above introduces the so-called (A, B)-pair, and in the following we use these connections in defining a class of entropy connections. Note that a (A, B)-pair satisfy the Rankine-Hugoniot condition, (2.2.5), due to entry 1. In figure 2.2.2 two such (A, B)-pair are drawn. Here (A_1, B_1) satisfy entries 1 and 2, and (A_2, B_2) satisfies entry 1, but not 2, thus is invalid as a (A, B)-connection.

We introduce two more definition before we look at examples on the application of (A, B)-connections.

Definition 4. Interface entropy functional. *Assume that $u^+(t) = \lim_{x \to 0^+} u(x, t)$ and $u^-(t) = \lim_{x \to 0^-} u(x, t)$ exists for a.e. t. The interface entropy functional is then defined as*

$$\begin{aligned} I_{AB}(t) :=& sign\left(u^-(t) - A\right)\left(g\left(u^-(t)\right) - g(A)\right) \\ & - sign\left(u^+(t) - B\right)\left(f\left(u^+(t)\right) - f(B)\right). \end{aligned} \tag{2.2.8}$$

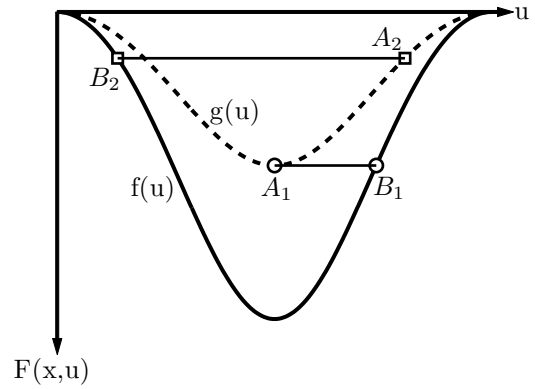

Figure 2.2.2: Flux functions with two (A, B)-connections. (A_1, B_1) is valid, but (A_2, B_2) is invalid

With the two above definitions, we define:

Definition 5. Interface entropy condition. *For* ***each*** *connection* (A, B) *we have the following interface entropy condition for a.e.* t

$$I_{AB}(t) \geq 0. \tag{2.2.9}$$

Definition 4 and 5 gives us restriction on which solutions we allow at $x = 0$. The solutions at each side of the interface $(x = 0)$ are represented by $u^+(t)$ and $u^-(t)$, called the *right* and *left traces*, respectively. To illustrated the use of the interface entropy condition and the solution procedure for conservation laws with discontinuous flux functions, we look at some examples:

Example 2. We solve the IVP (2.2.1), with the same flux functions given in figure 2.2.2, where we now concentrate on the valid (A, B)-connection, (A_1, B_1), from now on denoted (A, B). These are the same flux functions given in [12]. To emphasize that a jump at $x = 0$ does not always occur between (A, B) we look at the initial condition

$$u_0(x) = \begin{cases} 0, & x < 0, \\ 0.25, & x > 0. \end{cases} \tag{2.2.10}$$

A jump between g and f at A and B is illustrated in figure 2.2.3a. We immediately see that the entropy condition (2.2.7) is violated due to the negative shock speed of σ_R. Thus, the only valid solution with the initial condition (2.2.10) is

$$u(x,t) = \begin{cases} 0, & \text{if } x \leq \frac{g\left(u^-(t)\right) - g(0)}{u^-(t)} t, \\ u^-(t) \approx 0.4, & \text{if } \frac{g\left(u^-(t)\right) - g(0)}{u^-(t)} t < x < 0, \\ u^+(t) = u_R = 0.25, & \text{if } x \geq 0, \end{cases} \tag{2.2.11}$$

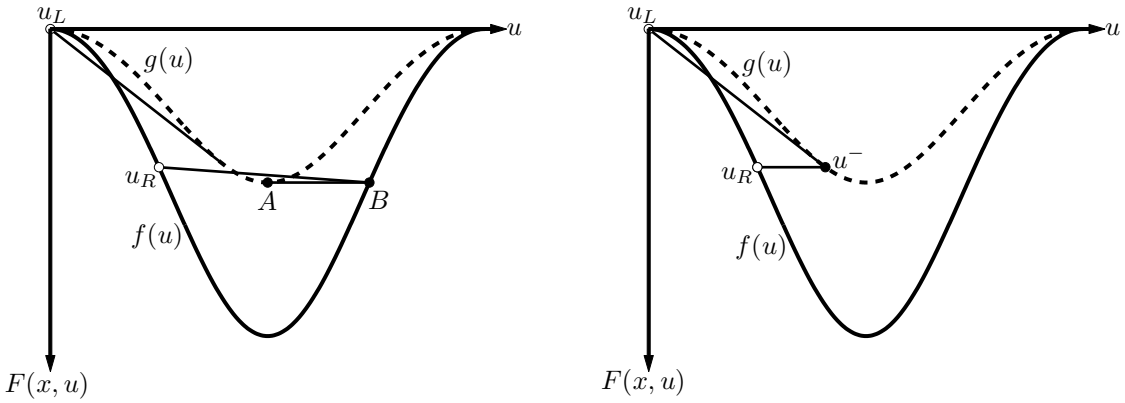

(a) Invalid solution (b) Valid solution

Figure 2.2.3: Flux functions for example 2

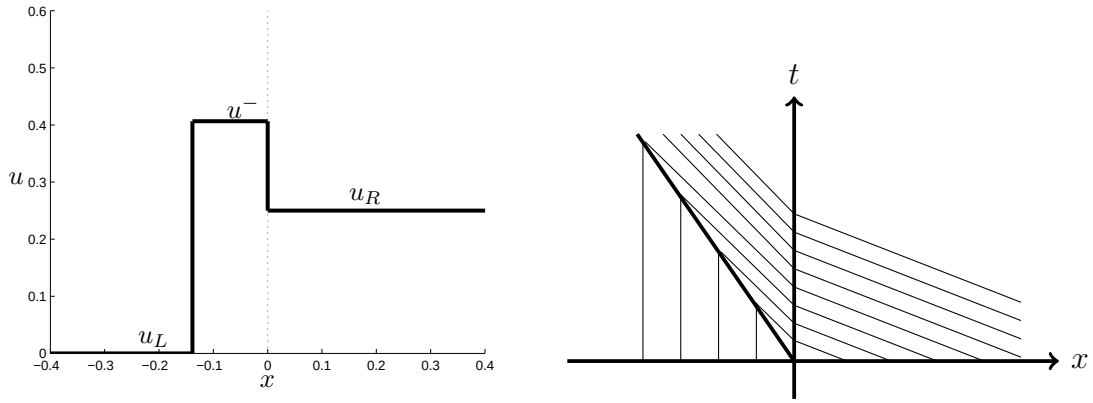

(a) Solution $u\,(x,t)$ at $t > 0$ (b) Characteristics

Figure 2.2.4: Solution and characteristics for example 2

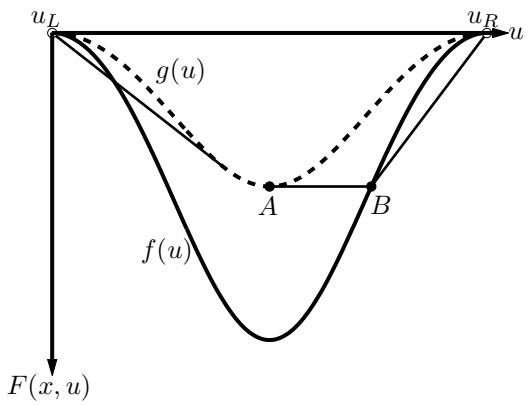

Figure 2.2.5: Flux functions for example 3, with the correct solution indicated

The correct jump between g and f is illustrated in figure 2.2.3b, and the solution together with the characteristics is shown in figure 2.2.4. Now we check the interface entropy functional defined in (2.2.8)

$$\begin{aligned} I_{AB}(t) &= \underbrace{sign\left(u^-(t)-A\right)}_{negative}\left(g\left(u^-(t)\right)-g(A)\right) \\ &\quad - \underbrace{sign\left(u^+(t)-B\right)}_{negative}\left(f\left(u^+(t)\right)-f(B)\right) \\ &= f\left(u^+(t)\right)-g\left(u^-(t)\right)+f(B)-g(A)=0. \end{aligned} \tag{2.2.12}$$

The last equality follow from the Rankine-Hugoniot condition (2.2.5) and entry 1 in definition 3. Hence the interface entropy condition (2.2.9) is satisfied with strict equality.

Example 3. The next initial condition we consider is

$$u_0 = \begin{cases} 0, & x<0, \\ 1, & x>0. \end{cases} \tag{2.2.13}$$

The flux functions are the same as for the previous example. The solution includes a jump at $x=0$ from A to B, and in the regions $(-\infty,0)$ and $(0,\infty)$ we must create convex hulls from u_L to A and B to u_R, respectively (cf. figure 2.2.5) The solution is given by

$$u(x,t) = \begin{cases} 0, & \text{if } x < \frac{g(u_s)-g(0)}{u_s}t, \\ (g')^{-1}\left(\frac{x}{t}\right), & \text{if } \frac{g(u_s)-g(0)}{u_s}t \le x \le 0, \\ B \approx 0.75, & \text{if } 0 < x \le \frac{f(1)-f(B)}{1-B}, \\ 1, & \text{if } x > \frac{f(1)-f(B)}{1-B}. \end{cases} \tag{2.2.14}$$

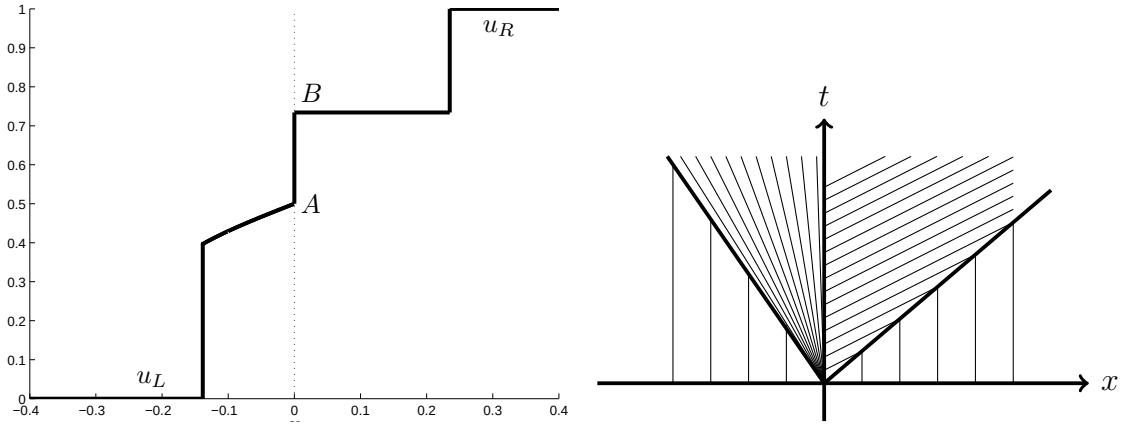

(a) Solution $u(x,t)$ at $t > 0$ (b) Characteristics

Figure 2.2.6: Solution and characteristics for example 3

and is illustrated in figure 2.2.6 with characteristics. If we check the interface entropy functional, it would have been equal zero, due to the jump being between A and B (i.e. $u^-(t) = A$ and $u^+(t) = B$) . Hence the interface entropy condition is satisfied.

Example 4. Before we continue, we look at one last example now with different flux functions. In figure 2.2.7 the flux functions intersect at $u = 0.5$, and $A = \theta_g$ and $B = \theta_f$. We wish to solve the IVP (2.2.1) for these flux functions with the initial condition

$$u_0(x) = 0.5. \tag{2.2.15}$$

The solution is simply

$$u(x,t) = u_0(x) = 0.5. \tag{2.2.16}$$

Let us see if it satisfies the interface entropy condition:

$$\begin{aligned} I_{AB}(t) &= \underbrace{sign\left(u^-(t) - A\right)}_{positive}\left(g\left(u^-(t)\right) - g(A)\right) \\ &- \underbrace{sign\left(u^+(t) - B\right)}_{negative}\left(f\left(u^+(t)\right) - f(B)\right) \\ &= 2\left(g\left(u^-(t)\right) - g(A)\right) > 0. \end{aligned} \tag{2.2.17}$$

The inequality above is easily verified with figure 2.2.7. Hence the interface entropy condition is satisfied with strict inequality. The entropy conditions away from $x = 0$ is also satisfied with this solution. If we had made a solution with shocks connecting u_0 with A in $(-\infty, 0)$ and u_0 with B in $(0, \infty)$ the shock speeds σ_L would have been positive and σ_R would have been negative. This violates the entropy conditions presented in theorem 3. Hence the solution (2.2.16) is unique.

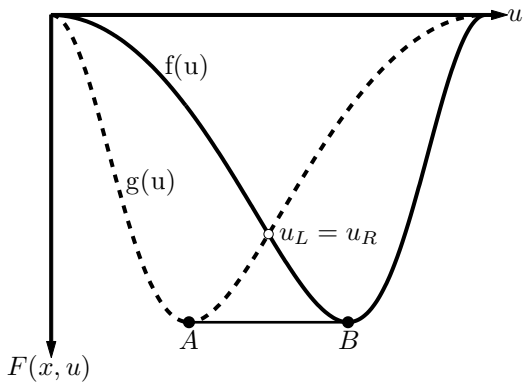

Figure 2.2.7: Flux function for example 4, with (A, B) indicated

We sum up the above analysis in the next definition [3].

Definition 6. AB-entropy solution. *A function* $u \in L^{\infty}(\Pi_T)$ *is defined as the entropy solution of* (2.2.1) *if the following holds*

1. u *is a weak solution of* (2.2.1)*, i.e. satisfying* (2.2.3)*.*
2. u *satisfies theorem 3 in the regions* $(-\infty, 0)$ *and* $(0, \infty)$*.*
3. u *satisfies the interface entropy condition* (2.2.9) *relative to the connection* (A, B) *at* $x = 0$*.*

With this definition, $u(x,t)$ is an entropy solution for a connection (A, B). Recall that for each choice of (A, B), we get a separate class of entropy solution, and (A, B) is a connection which must be chosen *before* the solution can be found. In the next chapter two of the possible (A, B)-connections relative to this thesis will be reviewed.

For existence, uniqueness and L^1-stability for each choice of (A, B), see [3] and references therein.

Remark. The interface entropy condition (2.2.9) is stated in [3] as a definition. In [9] they derive this condition using Kruzkov-type entropy inequality. We give a short review of the derivation in the following.
We start with defining a function, which handles the jump from A to B at $x = 0$, given as

$$c_{AB}(x) = H(x)\,B + (1 - H(x))\,A = \begin{cases} A, & \text{if } x < 0, \\ B, & \text{if } x > 0. \end{cases} \tag{2.2.18}$$

We use this function to define an entropy function similar to (2.1.8), given as

$$\eta(x,u) = |u - c_{AB}(x)|. \tag{2.2.19}$$

Thus, we can also define a entropy flux function similar to (2.1.9), given as

$$\psi(x,u) = sign(u - c_{AB}(x))(F(x,u) - F(x, c_{AB}(x))). \tag{2.2.20}$$

We can define a Kruzkov-type entropy inequality, similar to (2.1.12) defined in section 2.1.2.2, but now with the entropy functions given above:

$$\int\int_{\Pi_T} [|u - c_{AB}(x)|\phi_t + sign(u - c_{AB}(x))(F(x,u) - F(x, c_{AB}(x)))\phi_x]\, dxdt \geq 0, \tag{2.2.21}$$

for any test function $0 \leq \phi \in \Pi_T$. From this equation we can derive the interface entropy condition (see [9] and reference therein) given as

$$sign\left(u^+(t) - B\right)\left(f\left(u^+(t)\right) - f(B)\right) - sign\left(u^-(t) - A\right)\left(g\left(u^-(t)\right) - g(A)\right) \leq 0, \tag{2.2.22}$$

which is the same formula as (2.2.9), only here stated with $\leq$ instead of $\geq$ due to the order of the expressions. Hence, we can compare the procedure given above with the one leading to Oleinik's entropy condition in section 2.1.2.2.

2.2.3 The Physically Meaningful Entropy Solution

In the previous section we presented the general framework of (A, B)-entropy solutions, and showed that there exists infinitely many classes of entropy solutions corresponding to each choice of A and B that meet the conditions in section 2.2.2. But this is just the first step in choosing an entropy solution at $x = 0$. The second step is to single out the entropy solution corresponding to the physical model the conservation law is representing. Before we present the different entropy jump conditions, we shortly describe the physical models we encounter.

2.2.3.1 Two-phase Flow Model

We study capillary-free, immiscible fluid flow in a rigid isotropic porous medium. We only look at one dimensional flow. See e.g. [12] or [20]. We denote the non-wetting and wetting phase with nw and w, respectively. For an oil-water system, oil $= nw$ and water $= w$. The index l will be used to denote the two phases ($l = nw, w$). In this model saturation, S_l, is the conserved material.

The velocity of each phase follows Darcy's law

$$v_l = -\lambda_l \left(S_w\right) \left(\frac{\partial p_l}{\partial x} - \rho_l g \cos\theta \right). \tag{2.2.23}$$

Here, λ_l is the effective mobility of phase l, defined as

$$\lambda_l \left(S_w\right) = \frac{K k_l \left(S_w\right)}{\mu_l}, \tag{2.2.24}$$

where K denotes the absolute permeability, k_l the relative permeability and μ_l the viscosity of phase l. p_l is the pressure, $\rho_l = constant$ is the density of phase l, and $(g \cos\theta)$ is the influence of gravity at the angle of θ from the vertical axis.

Mass conservation to each phase is given by

$$\phi \frac{\partial S_l}{\partial t} + \frac{\partial v_l}{\partial x} = 0, \tag{2.2.25}$$

where $\phi = constant$ is the effective porosity and S_l is the saturation of each phase given by the state equation

$$S_w + S_{nw} = 1. \tag{2.2.26}$$

Adding together (2.2.25) for the two phases and using the identity (2.2.26) we get

$$\frac{\partial}{\partial x} \left(v_{nw} + v_w\right) = 0 \Rightarrow v_{nw} + v_w = v = constant, \tag{2.2.27}$$

defining v as the total Darcy velocity. This is *the pressure equation* for immiscible two-phase flow.
Subtracting (2.2.23) for each phase gives us

$$\frac{v_w}{\lambda_w} - \frac{v_{nw}}{\lambda_{nw}} - \left(g_w - g_{nw}\right) = 0, \tag{2.2.28}$$

where $g_l = \rho_l g \cos\theta$. By the assumption of capillary-free flow, $p_{nw} = p_w$, thus the derivatives of p_l cancel each other out. Using (2.2.27) we get

$$v_w = f\left(S_w\right) \left[v + \left(g_w - g_{nw}\right) \lambda_{nw} \right], \tag{2.2.29}$$

with the fractional flow function $f\left(S_w\right)$ defined by

$$f\left(S_w\right) = \frac{\lambda_w}{\lambda_w + \lambda_{nw}}. \tag{2.2.30}$$

The equation (2.2.25) for the wetting phase can be rewritten using (2.2.29) and denoting $S = S_w$

$$\phi \frac{\partial S}{\partial t} + \frac{\partial F\left(S\right)}{\partial x} = 0, \tag{2.2.31}$$

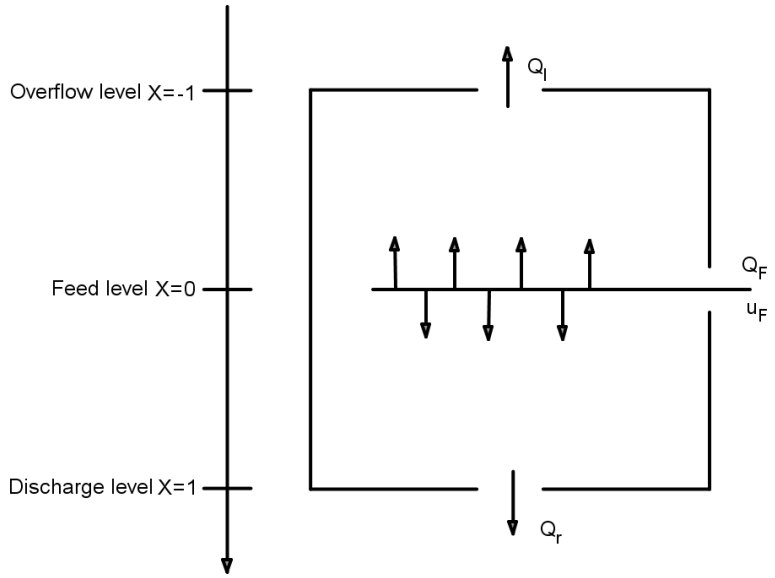

Figure 2.2.8: The one dimensional clarifier-thickener model

where $F(S)$ is the flux function for the wetting phase is

$$F(S) = f(S_w)\left[v + (g_w - g_{nw})\lambda_{nw}\right]. \tag{2.2.32}$$

Note that $F(S)$ is equal to v_w (in (2.2.29)). This is only the case when capillary pressure is neglected. The saturation equation (2.2.31) is of the form (2.1.1) for a homogeneous medium, but if we a dealing with a heterogeneous medium, (2.2.31) will be of the form (2.2.4). The discontinuity at $x = 0$ is a transition from one medium to another with different permeability attributes.

2.2.3.2 Clarifier-Thickener Model

In this section we give a short overview of the clarifier-thickener model with ideal units. This is the model for continuous sedimentation under ideal assumptions, that is, we have equal sized particles satisfying the one dimensional kinematic theory [15]. The main assumption is that the suspension is a mixture of two superpositioned continuous mediums, namely the fluid and the solid. We denote the concentration of the solid as u. For an extensive description of this model see e.g. [7] or [8]. In figure 2.2.8 we see the configuration for the one dimensional clarifier-thickener model. Here we have a feed suspension at $x = 0$ and two outlets at $x = 1$ and $x = -1$, where we find the discharge and overflow levels respectively. Denoting Q as the volumetric flow rate, we have volumetric balance of the mixture which requires that

$$Q_r = Q_l + Q_F, \tag{2.2.33}$$

where we have assumed that the rates are independent of time. The volumetric rates satisfy $Q_F \geq 0$, $Q_l \leq 0$ and $Q_r \geq 0$.

The continuity equation for the solids in $-1 < x < 1$ is

$$u_t + \left(q\left(x\right)u + h\left(u\right)\right)_x = \delta\left(x\right)\frac{Q_F u_F}{A}, \tag{2.2.34}$$

where $\delta\left(x\right)$ is the Dirac function, $h\left(u\right)$ is the nonlinear batch function, u_F is the concentration at the feed level, A is the cross-sectional area and $q\left(x\right)$ is the velocity defined by

$$q\left(x\right) = q_l + H\left(x\right)\left(q_r - q_l\right). \tag{2.2.35}$$

Here $H\left(x\right)$ is the Heaviside function. Using (2.2.33) and the fact that $q = Q/A$, (2.2.35) can be rewritten to

$$q\left(x\right) = q_l + H\left(x\right)\frac{Q_F}{A}. \tag{2.2.36}$$

Since $\delta\left(x\right)$ is the derivative of $H\left(x\right)$, we can insert (2.2.36) into the right side of (2.2.34) and end up with

$$u_t + \left(q\left(x\right)\left(u - u_F\right) + q_l u_F + h\left(u\right)\right)_x = 0, \tag{2.2.37}$$

for the interval $(-1, 1)$. The batch function is normally defined as

$$h\left(u\right) = \begin{cases} v_\infty u\left(1-u\right)^n, & \text{if } 0 < u < u_{max} = 1, \\ 0 & \text{otherwise.} \end{cases} \tag{2.2.38}$$

where $v_\infty > 0$ is the settling velocity of a particle in an unbounded, pure fluid and $n \geq 1$.
Outside the interval $(-1, 1)$ the batch flux function $h\left(u\right)$ is zero, so we can write a continuity equation for the whole model as

$$u_t + T\left(x, u\right)_x = 0, \tag{2.2.39}$$

where the flux function $T\left(x, u\right)$ is defined as

$$T\left(x,u\right) = \begin{cases} q_l u, & \text{for } x < -1, \\ F\left(q\left(x\right), u\right) = q\left(x\right)\left(u - u_F\right) + q_l u_F + h\left(u\right), & \text{for } -1 < x < 1, \\ q_r u + \left(q_l - q_r\right)u_F, & \text{for } x > 1. \end{cases} \tag{2.2.40}$$

The "interior" flux function, $F\left(q\left(x\right), u\right)$ has a discontinuity at $x = 0$ because of $q\left(x\right)$, defined in (2.2.35). As presented in (2.2.34), the reason the flux function F (and thereby T) has this discontinuity is because a source is present at $x = 0$, feeding material into the system.

2.2.3.3 The Jump Conditions

With the physical models described in the previous sections, we are ready to present the entropy jump conditions normally associated with the different models. We start off with presenting the entropy jump condition for the case of two-phase flow in porous medium

Optimal Entropy Condition

In the search for the appropriate solution of (2.2.1), Adimurthi et.al. [3] defines what they call *the interface entropy cost functional* $\boldsymbol{E}$. The idea is that functional E will be a measurement of the variation of the solution. By minimizing the maximal error for each choice of (A, B), they try to control the variation of the entropy solutions in an appropriate norm. By doing this they arrive at the following theorem

Theorem 4. The optimal connection(A_o, B_o)**.**

- For fluxes satisfying (H_2).

  If $f(\theta_f) \leq g(\theta_g)$*, then let* $\bar{\theta}_f \geq \theta_g$ *such that* $f(\theta_f) = g\left(\bar{\theta}_f\right)$ *, and if* $f(\theta_f) > g(\theta_g)$*,* $\bar{\theta}_g \geq \theta_f$ *such that* $f\left(\bar{\theta}_g\right) = g(\theta_g)$ *. There exist an unique optimal connection* (A_o, B_o) *given by*

$$(A_o, B_o) = \begin{cases} \left(\theta_g, \bar{\theta}_g\right), & \text{if } f(\theta_f) \geq g(\theta_g), \\ \left(\bar{\theta}_f, \theta_f\right), & \text{if } f(\theta_f) \leq g(\theta_g). \end{cases} \tag{2.2.41}$$

- For fluxes satisfying (H_3).

  If $f(\theta_f) \leq g(\theta_g)$*, then let* $\bar{\theta}_g \geq \theta_f$ *such that* $f\left(\bar{\theta}_g\right) = g(\theta_g)$*, and if* $f(\theta_f) > g(\theta_g)$*, then let* $\bar{\theta}_f \geq \theta_g$ *such that* $f(\theta_f) = g\left(\bar{\theta}_f\right)$ *. There exist an unique optimal connection* (A_o, B_o) *given by*

$$(A_o, B_o) = \begin{cases} \left(\theta_g, \bar{\theta}_g\right), & \text{if } f(\theta_f) \leq g(\theta_g), \\ \left(\bar{\theta}_f, \theta_f\right), & \text{if } f(\theta_f) \geq g(\theta_g). \end{cases} \tag{2.2.42}$$

If the flux functions f and g satisfies the hypotheses (H_1, H_2) or (H_1, H_3) we can choose (A, B) according to (2.2.41) or (2.2.42), respectively, just by considering the function values $g(\theta_g)$ and $f(\theta_f)$. This optimal connection entropy condition were also found by Adimurthi and Veerappa Gowda in [4], but there they use Hamilton-Jacobi theory and the fluxes were strictly convex. They also list explicit solutions for the Riemann problem (2.2.1) using the optimal connection (A_o, B_o).

Using a different approach, Kaasschieter ([12]) essentially derived the same entropy condition as [3], using the two-phase flow equation. Since the results in [12] is why we associate the entropy condition (2.2.42) with the condition to be used in two-phase flow model (c.f. section 2.2.3.1), it is worth taking a closer look at.

Consider the parabolic problem

$$\frac{\partial S_\varepsilon}{\partial t} + \frac{\partial F\left(S_\varepsilon\right)}{\partial x} + \varepsilon \frac{\partial}{\partial x}\left(\lambda\left(S_\varepsilon\right)\frac{\partial}{\partial x}P_c\left(S_\varepsilon\right)\right) = 0 \tag{2.2.43}$$

here $F\left(S_\varepsilon\right)$ can be $F_L\left(S_\varepsilon\right)$ (for $x < 0$) or $F_R\left(S_\varepsilon\right)$ (for $x > 0$) which correspond to g or f, respectively. S_ε is saturation, ε is the regularization variable, P_c is the capillary pressure function and λ is the total mobility (see section 2.2.3.1). As pointed out earlier, an entropy inequality is usually derived from a regularized problem like (2.2.43), by letting $\varepsilon \to 0$. In porous medium fluid flow, the capillary pressure must be continuous, even across heterogeneities. However, the mobility function, λ, contains both relative and absolute permeability, and therefore can be discontinuous across heterogeneities. This gives us some requirements that (2.2.43) must meet when $\varepsilon \to 0$. By introducing the notation $F_L'\left(S_L\right) \succeq 0$ used when $F_L'\left(S_L\right) \geq 0$ and $\lim_{S\to S_L^-} sign\left(F_L'\left(S\right)\right) = 1$ **or** $\lim_{S\to S_L^+} sign\left(F_L'\left(S\right)\right) = 1$, and $F_R'\left(S_R\right) \preceq 0$ used when $F_R'\left(S_R\right) \leq 0$ and $\lim_{S\to S_R^-} sign\left(F_R'\left(S\right)\right) = -1$ **or** $\lim_{S\to S_R^+} sign\left(F_R'\left(S\right)\right) = -1$, Kaasschieter derived the following jump condition

Entropy inequality. Let s be discontinuous (or even continuous) at $\xi = 0$, then $F_L'\left(S_L\right) \succeq 0$ <u>or</u> $F_R'\left(S_R\right) \preceq 0$,

where s is the similarity solution $S\left(x/t\right)$ with $\xi = x/t$, $S_L = \lim_{x\to 0^-} S\left(x,t\right)$ and $S_R = \lim_{x\to 0^+} S\left(x,t\right)$. This entropy jump condition gives us restrictions on which characteristics we allow at $x = 0$. The only characteristics we do not allow with this entropy inequality is where both $F_L'\left(S_L\right) < 0$ and $F_R'\left(S_R\right) > 0$, that is, when the characteristics go out of the discontinuity at $x = 0$.

As noted above, this entropy inequality gives the same solutions as the optimal entropy connection (A_o, B_o). According to definition 3, choosing another (A, B)-connection other the optimal entropy connection (A_o, B_o), leads to jumps between g and f where $g'\left(A\right) < 0$ and $f'\left(B\right) > 0$, thus not allowed by the inequality above. Since (2.2.42) says that $(A, B) = \left(\theta_g, \bar{\theta}_g\right)$, $(A, B) = \left(\bar{\theta}_f, \theta_f\right)$ or $(A, B) = \left(\theta_g, \theta_f\right)$, the entropy inequality above ([12]) is always satisfied, hence they are equal.

Minimal Jump Condition

In [10, 11], Gimse and Risebro investigate the Riemann problem (2.2.1), and proposes a different entropy jump condition than in [3]. The flux functions must satisfy a more general assumption demanding only smoothness and to have finitely critical point, but hypotheses (H_1) must still be satisfied. The entropy condition presented in [10] is the following:

Theorem 5. The minimal jump condition. *Let $u \in L_1^{loc}$, and denote, as before, $u^-(t) = \lim_{x\to 0^-} u(x,t)$ and $u^+(t) = \lim_{x\to 0^+} u(x,t)$. There exist a unique solution $u(x,t)$ to (2.2.1), satisfying (2.2.5), that minimizes*

$$\left|u^-(t) - u^+(t)\right|. \tag{2.2.44}$$

To justify the principle of minimal jump across the discontinuity, the authors present two arguments. The first argument states that (2.2.1) must be invariant during the transformation

$$\begin{aligned} x &\to -x, \\ g &\to -g, \\ f &\to -f, \end{aligned} \tag{2.2.45a}$$

which implies

$$\begin{aligned} u_L &\to u_R, \\ u_R &\to u_L, \end{aligned} \tag{2.2.45b}$$

and therefore the solution $u(x,t)$ must also be invariant under the same transformation, in order to be unique. Thus, u must not depend on the particular choice of $u^-(t)$ or $u^+(t)$. Hence, the only principle for selecting $u^-(t)$ and $u^+(t)$ is the one which maximizes or minimizes the difference between them.

The second argument, is where the "correct" solution is chosen to be when the difference is minimized. This is done be showing that the minimal jump condition is equal to a *viscous profile entropy solution*, which is a solution to the following parabolic equation

$$y_t^\epsilon + F\left(y^\epsilon\right)_x = \epsilon y_{xx}^\epsilon, \qquad \epsilon > 0, \tag{2.2.46}$$

when $\epsilon \to 0$. The equivalence is proved by extending (2.2.1) to a triangular system (2×2 system of equations), where we introduce a parameter to "conserve" the discontinuity in the flux at $x = 0$. This is done through the conservation law

$$\begin{aligned} v_t + g\left(v\right)_x &= 0, \\ v_0(x) &= H(x). \end{aligned} \tag{2.2.47}$$

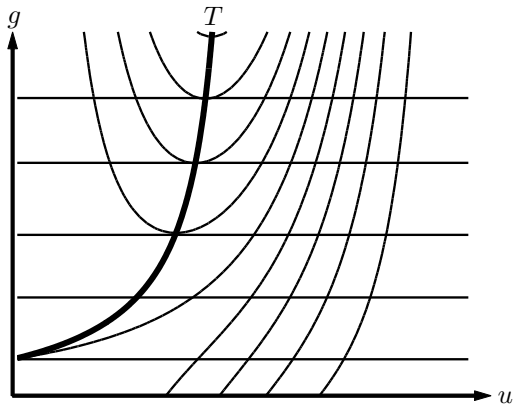

Figure 2.2.9: $(u, g)-$ phase plane for typical porous medium flux functions. The straight lines are u-waves and the contour plots are g-waves.

If $g(v)$ is a function with $g(0) = g(1) = 0$, $g(v) \geq 0$ for $v \in [0, 1]$, then the solution of (2.2.47) is the stationary solution $v(x, t) = H(x)$. Now if we let $F(u, v) = (1 - v)\, g(u) + v f(u)$,we can write (2.2.1) as a triangular system

$$\begin{aligned} v_t + g(v)_x &= 0, \\ u_t + F(u, v)_x &= 0. \end{aligned} \tag{2.2.48}$$

Note that the solution $v(x, t)$ only affects $u(x, t)$ through the flux function $F(u, v)$, and (2.2.47) does not depend on $u(x, t)$, it is only a physical consideration. Thus we can write both of the equations in (2.2.48) as a limit of some sort of parabolic equation (2.2.46). A thorough proof of the equivalence is given in [10], and it relies heavily on theory of hyperbolic systems of equations.

In [11] the authors gives a solution procedure for (2.2.1) using the minimal jump condition. By considering the equation of the type (2.2.2), we can use the theory on solving hyperbolic systems of equation, see e.g. [24] or [1]. For example, considering flow in petroleum reservoir as described in section 2.2.3.1, we have two equations for each porous medium with different permeability properties, thus two equation of the type (2.2.4). Following [11], we have two wave solutions, let us call them *u-waves* and *g-waves*. A u-wave is a wave of constant g, and is thus a Buckley-Leverett wave for one of the equations in 2.2.4 depending on the constant g. A g-wave is a wave of constant flow, i.e. $F(x, u) = constant$. Drawing the level curve of $F(x, u)$ in the (u, g)-phase plane, is crucial in solving hyperbolic systems and in figure 2.2.9 we see a typical set of such level curves for the porous medium flow model. The bold curve T represents the transition curve where $\partial_u F(x, u) = 0$. The solution of the Riemann problem (2.2.1) consist of connecting u-waves and g-waves from u_L to u_R. An example of a solution is found in [11].

If the flux functions satisfy the hypothesis (H_1)-(H_3), we have a much simpler

procedure for solving (2.2.1) with respect to the minimal jump condition. Since A and B must be chosen according to the constraints in section 2.2.2, choosing them such that the jump between them are minimal is easy. In the case where the flux functions intersects in u_χ, the choice $A = B = u_\chi$ if $g'(A) < 0$ and $f'(B) > 0$, is allowed by the minimal jump condition.

Comparing the Two Jump Conditions

Now that we have presented the two entropy conditions, let us do a comparison to show where they differ. We need some definitions before continuing

Definition 7. Solution types. Let $u^-(t)$ and $u^+(t)$ be defined as before (see e.g. section 2.2.1) . The solution u is said to be

1. *Regular* if either $g'(u^-(t))$, $f'(u^+(t)) \geq 0$ or $g'(u^-(t))$, $f'(u^+(t)) \leq 0$.
2. *Overcompressive* if $g'(u^-(t)) > 0$ and $f'(u^+(t)) < 0$.
3. *Undercompressive* if $g'(u^-(t)) < 0$ and $f'(u^+(t)) > 0$.
4. *Marginally under(over)compressive* if either $g'(u^-(t)) = 0$ and $f'(u^+(t)) \geq 0$ or $g'(u^-(t)) \leq 0$ and $f'(u^+(t)) = 0$.

These definitions of solution types, or wave types, can best be looked at from the perspective of characteristics. Figure 2.2.10 shows all five of the solution types defined in definition 7.[2]

The hypotheses on the flux functions, (H_1)-(H_3), does not dictate how the flux functions intersects in the interior of the domain $[s, S]$. In fact, they do not need to intersect at all. If they do not intersect, it is easy to see that the optimal connection and the minimal jump condition coincides. To illustrate this, we look at figure 2.2.11 where an example of non-intersecting flux functions together with the possible domain of (A, B) according to definition 3 is drawn. The minimal jump between A and B is when $A = \theta_g$ and $B = \bar{\theta}_g$, i.e. the optimal entropy connection. This is true also for other cases where the flux functions do not intersect, thus the optimal entropy and minimal jump solution coincides.

[2]The names *over- and undercompressive* comes from theory on nonstrictly hyperbolic systems. The Lax condition states that the characteristic speed behind the shock must be greater than the speed of the shock, which is greater than the speed in front of the shock. A undercompressive wave does not fulfill this condition, while a overcompressive wave does with more characteristics impinging the shock than the Lax condition require. See [17].

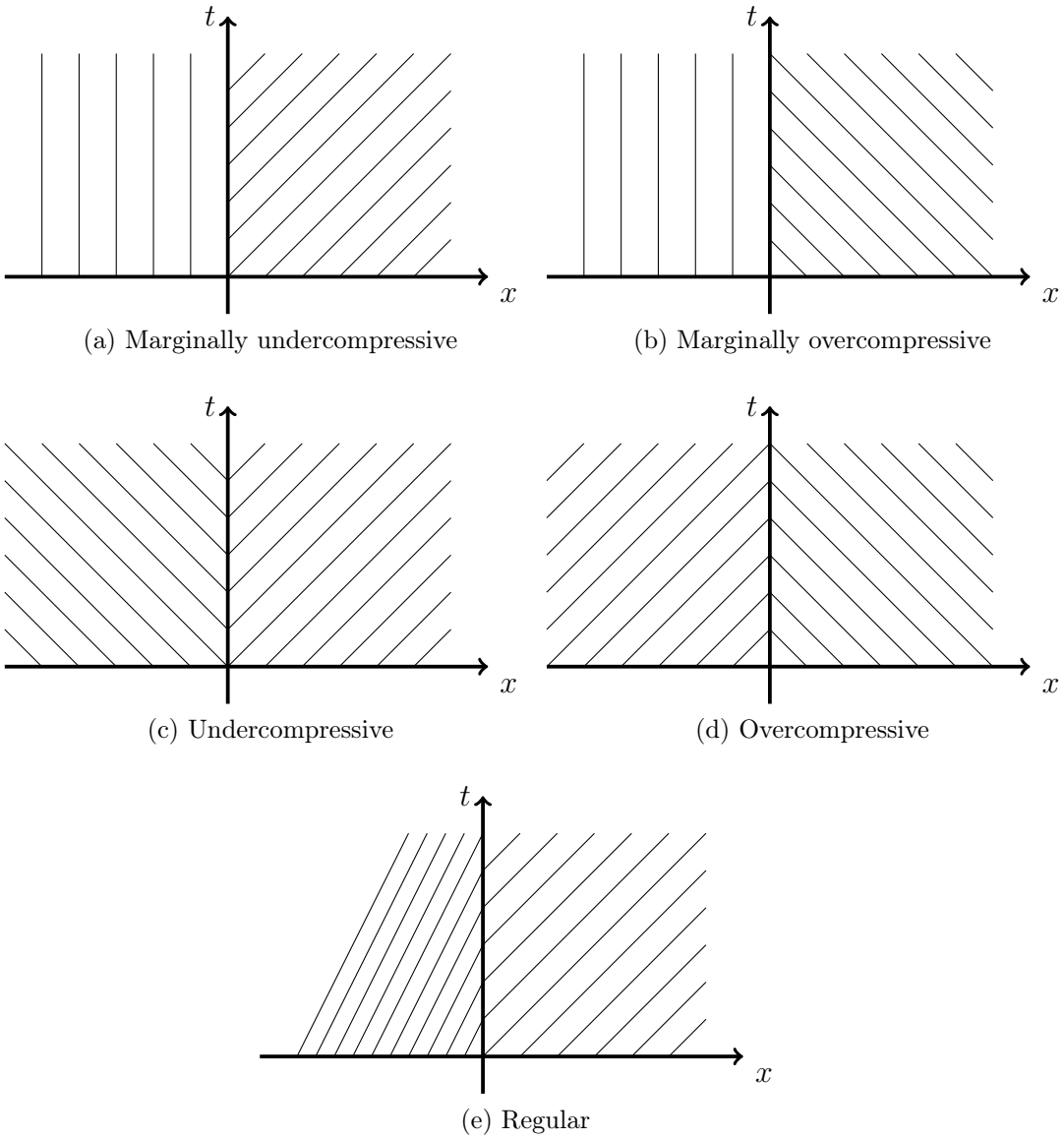

(a) Marginally undercompressive

(b) Marginally overcompressive

(c) Undercompressive

(d) Overcompressive

(e) Regular

Figure 2.2.10: Characteristics for the five solution type

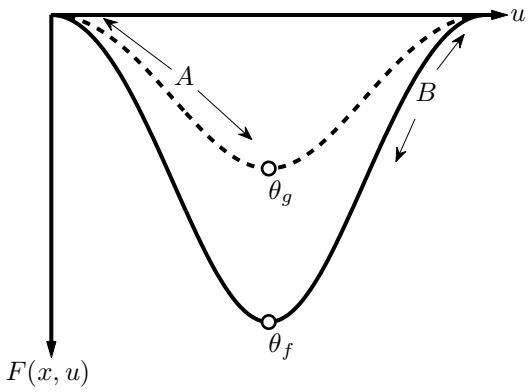

Figure 2.2.11: Non-intersecting flux functions with domain for A and B indicated

The flux functions can intersect in two ways, either in a *compressive manner* where A and B can not be chosen as the intersection value, u_χ, or in a *undercompressive manner* where $A = B = u_\chi$ is a possible choice. Both cases are illustrated in figure 2.2.12. In the first case, figure 2.2.12a shows that the minimal jump from A to B is when $A = \theta_g$ and $B = \theta_f$, and this is exactly the optimal entropy connection. In the second case, where the intersection is undercompressive, we see from figure 2.2.12b that $A = B = u_\chi$ is the minimal jump from A to B, where as the optimal entropy connection is still when $A = \theta_g$ and $B = \theta_f$. Hence, this is the only case where both entropy jump conditions differ.
Note that these results is valid for all alterations of non-intersecting and intersecting fluxes satisfying (H_1) - (H_3).

As noted above, the optimal entropy condition excludes undercompressive solution waves, but the minimal jump condition does not. As already established, the optimal entropy condition is the natural assumption when considering the two-phase flow model. As for the clarifier thickener model, the natural jump condition is the minimal jump condition. Here we have a source term present at $x = 0$, feeding suspension into the system in direction of both $x > 0$ and $x < 0$. The flux functions associated with the clarifier thickener model always intersects in a undercompressive manner, and u_χ is value of u at $x = 0$, namely u_F (c.f. (2.2.40) and (2.2.35)). Thus, characteristics as shown in figure 2.2.10c (where characteristics goes out at both sides of the discontinuity) is correct.

The entropy inequality given by Kaasschieter in [12] excludes the undercompressive waves, and only accepts solutions given in figure 2.2.10a, 2.2.10b, 2.2.10d and 2.2.10e. In the two phase flow model, a discontinuity represents a transition from one porous medium property to another, hence, no source term is present at the discontinuity. Therefore the undercompressive solution is readily omitted.

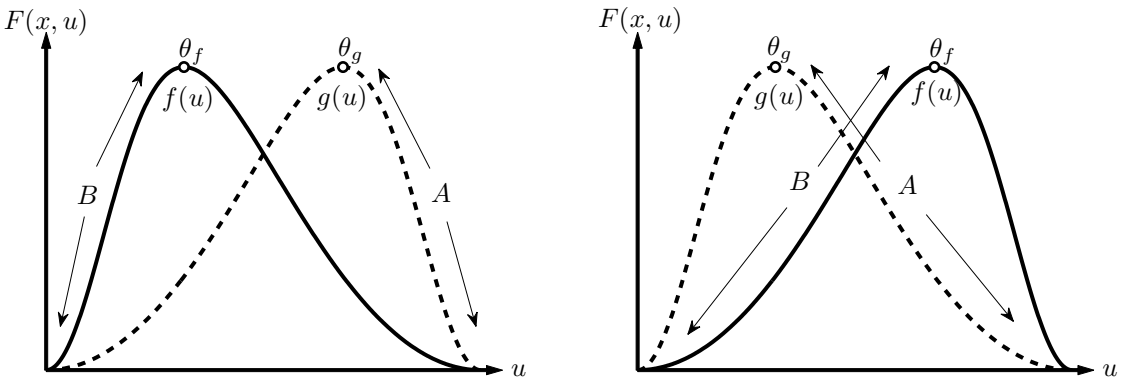

(a) Flux functions intersecting in a *compressive manner*, i.e. $f'(u_\chi) < 0$ and $g'(u_\chi) > 0$

(b) Flux functions intersecting in a *undercompressive manner*, i.e. $f'(u_\chi) > 0$ and $g'(u_\chi) < 0$

Figure 2.2.12: Intersecting flux functions with the domain of A and B indicated

2.3 Example of Heterogeneous Two-phase Flow

Since two-phase flow in porous medium is solved differently than the examples presented in section 2.2.2, it is useful to give an extensive example of the solution procedure for these type of problems. Example 1 at the end of section 2.1.3 is an example of the homogeneous two phase flow problem, thus it is useful to compare the solution produce with the one presented there. The heterogeneity in the porous medium model is, as noted before, a transition from one permeability property to another, somewhere in the reservoir. Thus, if we have the initial value at $x = 0$, the heterogeneity is located at $x_h > 0$. The theory presented in the previous sections still applies, only now, with a more elaborate solution procedure as the following will show.

The initial value problem is slightly differently formulated:

$$\begin{aligned} u_t + g(u)_x &= 0, \quad x < x_h, \\ u_t + f(u)_x &= 0, \quad x > x_h, \end{aligned} \tag{2.3.1}$$

$$u_0(x) = \begin{cases} u_L, & x < 0, \\ u_R, & x > 0. \end{cases} \tag{2.3.2}$$

The initial condition is only concerning the conservation law $u_t + g(u)_x$, thus for $x < x_h$ we can solve the problem in a "homogeneous" manner, i.e. with the procedure presented in section 2.1.3. At $x = x_h$ we use the interface entropy condition to single out the correct jump between $g(u)$ and $f(u)$. After the heterogeneity, the solution must fulfill the entropy condition given in theorem

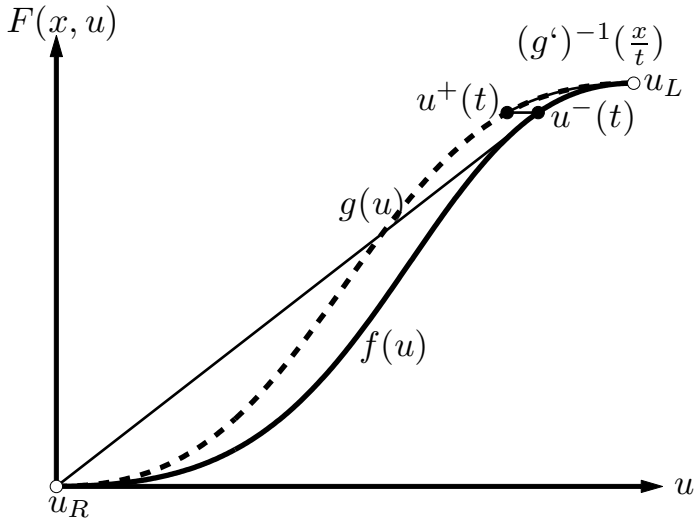

Figure 2.3.1: Flux functions $g(u)$ and $f(u)$with the solution path drawn. Note that jump between $g(u)$ and $f(u)$ is time dependent due to the rarefaction wave $(g')^{-1}(x/t)$ and the solution presented is after the wave solution has passed $x = x_h$. Note also that the (A, B)-connection is $A = B = u_L$.

3, i.e. a shock in the region (x_h, ∞) must have a positive velocity and meet condition 2.2.7.

We illustrate the solution procedure by looking at an example where the flux functions is given in figure 2.3.1 . The initial value is indicated in the figure, together with the solution, which is given for $t > t_h$(where t_h is the time when the wave reaches $x = x_h$) as

$$u(x,t) = \begin{cases} u_L, & x < 0, \\ (g')^{-1}\left(\frac{x}{t}\right), & 0 \le x \le x_h, \\ u^+(t), & x_h < x < \frac{f(u_R)-f\left(u^+(t)\right)}{u_R-u^+(t)}, \\ u_R, & x \ge \frac{f(u_R)-f\left(u^+(t)\right)}{u_R-u^+(t)}. \end{cases} \tag{2.3.3}$$

The solution is given in figure 2.3.2 together with the characteristics. As for the examples in section 2.2.2, we can check if the interface entropy condition, (2.2.8), is fulfilled. Recall from figure 2.3.1, that $A = B = u_L$

$$\begin{aligned} I_{AB}(t) &= \underbrace{sign\left(u^-(t) - A\right)}_{negative}\left(g\left(u^-(t)\right) - g(A)\right) \\ &- \underbrace{sign\left(u^+(t) - B\right)}_{negative}\left(f\left(u^+(t)\right) - f(B)\right) \\ &= \left[g(A) - f(B)\right] + \left(f\left(u^+(t)\right) - g\left(u^-(t)\right)\right) = 0. \end{aligned} \tag{2.3.4}$$

The interface entropy condition is fulfilled with strict equality. It is easily checked that this is true for all $t > t_h$ due to the fact $A = B = u_L = 1$ which is the end point of the flux functions, making the sign functions in (2.3.4) negative for $t > t_h$.

Remark. The solution is dynamic in the sense that the rarefaction wave, $(g')^{-1}(x/t)$, can change the solution from time to time dependent on the shape of $f(u)$ and $g(u)$. Thus the solution given in (2.3.3) might change after some time.

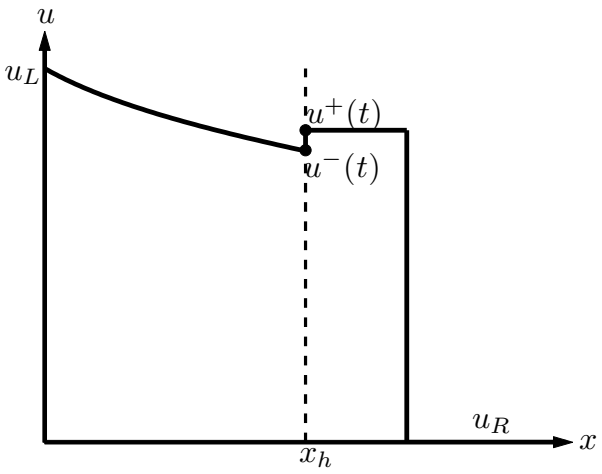

(a) Solution at time $t > t_h$

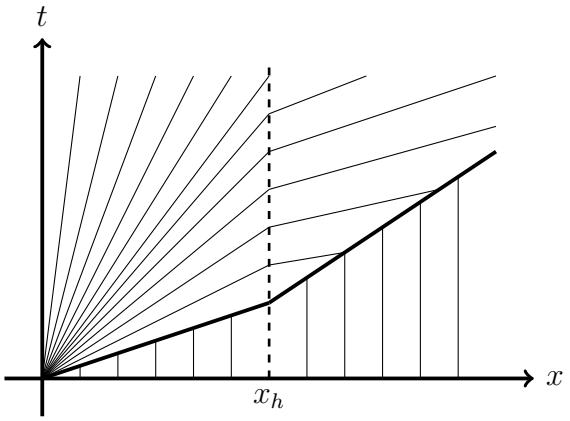

(b) Characteristics for the example. Note the characteristics where $x > x_h$ emerging from the rarefaction wave have different speed, illustrating the statement in the remark.

Figure 2.3.2: Solution after some fixed time $t > t_h$, and characteristics

Chapter 3

Numerical Methods

In the previous chapter we reviewed the theory of conservation laws with and without a spatial discontinuous flux function. We saw that basic physical principles must be conserved, and in this chapter we present numerical methods which also must mimic the same properties as the differential equation. From classic theory on difference equation, see e.g. [17], we know that the important properties a numerical method must possess to ensure convergence is *consistency* and *stability.* In the numerical methods for hyperbolic conservation laws, consistency is apprehended through *local conservation* and *flux consistency,* and stability is achieved by ensuring *monotonicity.* Considering weak solutions of conservation laws, we allow shock waves to occur, demanding strict requirements on the numerical method. To ensure convergence to the right solution, Lax-Wendroff's theorem [16] states that if a conservative numerical method converges, then it converges towards a weak solution. The scheme must also converge to the correct physical solution, and therefore we must require monotonicity. All these requirements are readily acquired for numerical methods for conservation laws **without** the spatial discontinuity, but not so intuitively apprehended **with** the spatial discontinuity. Thus, different properties may be required for the method to be convergent . The methods studied here are *finite volume methods.* Before we present the methods, we first give some general definitions which form the basics for all the methods.

3.1 Basic Definitions

3.1.1 Grid and Conservative Methods

We give numerical methods for the conservation law

$$u_t + F(x,u)_x = 0, \tag{3.1.1}$$

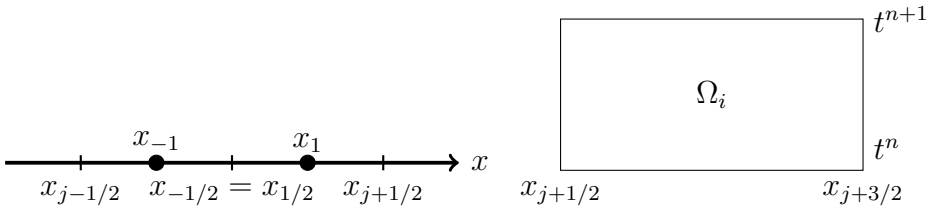

(a) The grid at $x = 0$ (b) The cell Ω_i over the time step Δt

Figure 3.1.1: Grid and Ω_i

where, as before, $F(x,u)$ is the flux function discontinuous at $x = 0$ in the sense that $F(x,u) = H(x) f(u) + (1 - H(x)) g(u)$. f and g are nonlinear, Lipschitz continuous functions as defined in the theory chapter. To include weak solutions of (3.1.1), we must consider the integral formulation of the equation:

$$\int_{x_1}^{x_2} u(x,t_2)\,dx - \int_{x_1}^{x_2} u(x,t_1)\,dx + \int_{t_1}^{t_2} F(x_2, u(x_2,t))\,dt - \int_{t_1}^{t_2} F(x_1, u(x_1,t))\,dt = 0 \tag{3.1.2}$$

for each control volume $[x_1, x_2] \times [t_1, t_2]$. Before we define a conservative scheme, we define the grid used throughout the chapter.

We discretize the spatial domain $\mathbb{R}$ into grid cells $I_j := \left(x_{j-1/2}, x_{j+1/2}\right)$ with equidistant width of $\Delta x > 0$. Here $j \in \mathbb{Z}$, and we define:

$$x_{j-1/2} = j\Delta x \text{ for } j \le 0, \quad x_{j+1/2} = j\Delta x \text{ for } j \ge 0, \quad x_{-1/2} = x_{1/2} = 0.$$

The cell centers are defined as

$$x_j = (j - 1/2)\,\Delta x, \text{ for } j \ge 1, \quad x_j = (j + 1/2)\,\Delta x, \text{ for } j \le -1.$$

The time domain $(0, T)$ is discretized by $t^n = n\Delta t$, where $\Delta t > 0$ is the time step and $n = 0, \ldots, N$. We let the time interval be defined as $I^n := [t^n, t^{n+1}]$. A cell $\Omega_i = I_j \times I^n$ is shown in figure 3.1.1, together with a figure of the grid at $x = 0$. When we discretize the (3.1.2) for a cell Ω_i , we use the definitions:

$$\begin{aligned} u_{j+1}^n &= \frac{1}{\Delta x} \int_{x_{j+1/2}}^{x_{j+3/2}} u(x,t^n)\,dx \text{ for } j \ge 0, \\ u_{j-1}^n &= \frac{1}{\Delta x} \int_{x_{j-3/2}}^{x_{j-1/2}} u(x,t^n)\,dx \text{ for } j \le 0, \end{aligned} \tag{3.1.3}$$

$$\mathcal{F}_{j+1/2}^n = \begin{cases} \frac{1}{\Delta t} \int_{I^n} g\left(u\left(x_{j-1/2}, t\right)\right) dt, & \text{for j<0,} \\ \overline{F}^n, & \text{for } j = 0, \\ \frac{1}{\Delta t} \int_{I^n} f\left(u\left(x_{j+1/2}, t\right)\right) dt, & \text{for } j > 0. \end{cases} \tag{3.1.4}$$

where $\mathcal{F}_{j+1/2}$ is the numerical flux function, approximating the real flux function $F(x,u)$. To ensure that the flux $\mathcal{F}^n_{j+1/2}$ has the same value on the cell edge between Ω_i and Ω_{i+1} we determine the flux using the values u^n_j and u^n_{j+1}, i.e.

$$\mathcal{F}^n_{j+1/2} = \mathcal{F}\left(u^n_j, u^n_{j+1}\right) = \begin{cases} G\left(u^n_{j-1}, u^n_j\right), & \text{for j}\leq\text{-1,} \\ \overline{F}\left(u^n_{-1}, u^n_1\right), & \\ F\left(u^n_j, u^n_{j+1}\right), & \text{for j}\geq\text{1.} \end{cases} \tag{3.1.5}$$

Note that u^n_0 does not exist due to the way we defined the cell centers.

Now we can define a conservative method for our problem (3.1.1).

Definition 8. Conservative method. *A conservative scheme for the differential equation* (3.1.1) *is a numerical method of the form*

$$\begin{aligned} u^{n+1}_j &= u^n_j - \lambda\left(G\left(u^n_j, u^n_{j+1}\right) - G\left(u^n_{j-1}, u^n_j\right)\right), \quad \text{if } j < -1, \\ u^{n+1}_{-1} &= u^n_{-1} - \lambda\left(\overline{F}\left(u^n_{-1}, u^n_1\right) - G\left(u^n_{-2}, u^n_{-1}\right)\right), \\ u^{n+1}_1 &= u^n_1 - \lambda\left(F\left(u^n_1, u^n_2\right) - \overline{F}\left(u^n_{-1}, u^n_1\right)\right), \\ u^{n+1}_j &= u^n_j - \lambda\left(F\left(u^n_j, u^n_{j+1}\right) - F\left(u^n_{j-1}, u^n_j\right)\right), \quad \text{if } j > 1, \end{aligned} \tag{3.1.6}$$

where $\lambda := \frac{\Delta t}{\Delta x}$.

3.1.2 The CFL-condition

When dealing with explicit numerical schemes, especially for hyperbolic PDEs, a necessary (but not always sufficient) condition for convergence is the *Courant-Friedrichs-Lewy (CFL) -condition*

$$\frac{\Delta t}{\Delta x}\left\|h'(u)\right\|_{L^\infty} \leq 1, \tag{3.1.7}$$

for a flux function $h(u)$. If a finite difference method fulfill the CFL-condition, its domain of dependence include the domain of dependence of the differential equation. The domain of dependence for the point (x,t), when looking at a general hyperbolic PDE, $u_t + h(u)_x = 0$, is defined as the point $\xi = x - h'(u)\,t$ on the x-axis. If the CFL-condition is violated, a change in the initial data will change the true solution at (x,t), but not the numerical solution at this point.

3.1.3 Consistency and Monotonicity

As mentioned in the introduction, consistency and monotonicity are important properties for ensuring convergence for numerical methods.

The numerical flux should approximate the flux as defined in (3.1.4), especially if the true solution is $u(x,t) = constant = \bar{u}$, then the integral in (3.1.4) reduces to $f(\bar{u})$ and $g(\bar{u})$ away from the interface $x = 0$. As a result, when $u_j^n = u_{j+1}^n = \bar{u}$, we naturally require the approximate flux function $\mathcal{F}$ to reduce to either $f(\bar{u})$ or $g(\bar{u})$, that is, we require

$$F(\bar{u}, \bar{u}) = f(\bar{u}), \tag{3.1.8}$$

and

$$G(\bar{u}, \bar{u}) = g(\bar{u}), \tag{3.1.9}$$

Consistency for the interface flux function $\overline{F}$, can be defined as consistent with either $g(\bar{u})$ or $f(\bar{u})$.

Monotonicity is a stability condition which ensures that a method fulfill the entropy condition, at least for conservation laws *without* spatially discontinuous flux functions. It is still an important property for conservation laws *with* discontinuous flux functions, and the methods described later will be investigated for this property. Thus, we need the basic definition for monotonicity.
An explicit method can be written on the form $\mathbf{u}^{n+1} = \mathbf{H}(\mathbf{u}^n)$,where

$$\mathbf{u}^n = \left[\ldots, u_{j-1}^n, u_j^n, u_{j+1}^n, \ldots\right]. \tag{3.1.10}$$

Definition 9. Monotone method. A explicit method is called monotone if

$$\mathbf{u} - \mathbf{v} \geq \mathbf{0} \quad \Longrightarrow \quad \mathbf{H}(\mathbf{u}) - \mathbf{H}(\mathbf{v}) \geq \mathbf{0}. \tag{3.1.11}$$

As noted in [1], it holds to check if the Jacobian $\mathbf{H}'(\mathbf{u}) \geq \mathbf{0}$. From the definition of a conservative scheme above we notice that the approximate solution u_j^{n+1} depends only on u_{j-1}^n, u_j^n and u_{j+1}^n, thus the monotonicity condition reduces to check if

$$\frac{\partial H_j}{\partial u_{j-1}} \geq 0, \quad \frac{\partial H_j}{\partial u_j} \geq 0, \quad \frac{\partial H_j}{\partial u_{j+1}} \geq 0. \tag{3.1.12}$$

3.2 Godunov's Method

The challenge of finding the best approximation of the flux function is obviously best solved by using (3.1.1) with the known values at t^n. Thus, by finding the exact solution until some finite time t^{n+1} and using this in calculating $\mathcal{F}_{j+1/2}$, we have a method which solves the numerical problem semi-analytically. This is the basic idea of *Godunov's method.*
To find the exact solution, we solve the equation

$$u_t + F(x,u)_x = 0, \quad t > t^n, \tag{3.2.1}$$

with the initial condition

$$u\left(x,t^{n}\right)=u^{n}\left(x\right), \tag{3.2.2}$$

where $u^{n}\left(x\right)=u_{i}^{n}$ for $x\in I_{j}$. By the definition of the numerical fluxes (3.1.4), all we need is the value $u\left(x,t\right)$ at the cell edges. This is equivalent of solving a local Riemann problem at each cell edge $x_{j+1/2}$ with $u_{L}=u_{j}$ and $u_{R}=u_{j+1}$ at a fixed time. For the cell edges $x_{j-1/2}$ we use $u_{L}=u_{j-1}$ and $u_{R}=u_{j}$. Thus, we have all the information to calculate $f\left(u\left(x_{j+1/2},t\right)\right)$ and $g\left(u\left(x_{j-1/2},t\right)\right)$. The solution at each cell edge will be a wave solution described in section 2.1.3. Since the waves from each local Riemann problem can intersect in finite time, we have to restrain the time step

$$t^{n+1}\leq t^{n}+\frac{\Delta x}{\left\|f'\right\|_{L^{\infty}}}, \tag{3.2.3}$$

This is just the CFL-condition, and a similar condition must be satisfied for g. Note that this procedure is only valid when $j<-1$ and $j>1$ in (3.1.6), i.e. when (3.1.1) is equal to either $u_{t}+g\left(u\right)_{x}=0$ or $u_{t}+f\left(u\right)_{x}=0$ respectively. We will describe the interface flux $\overline{F}$ shortly. The solution given at the cell edge is either the constant state on the side from which the elementary wave travel from, or if the wave velocity is zero, the solution is given by the initial value (3.2.2). In the last case, u is discontinuous, but the Rankine-Hugoniot condition with $\sigma=0$ ensures that f or g is continuous. In section 2.1.3, we saw that the easiest way of solving a Riemann problem was looking at the convex and concave hulls of the flux functions. With the definition of these hulls in mind we can set up expression for the fluxes away from the discontinuity at $x=0$:

$$G^{G}\left(u_{L},u_{R}\right)=\begin{cases}\min\limits_{u\in[u_{L},u_{R}]}g\left(u\right), & \text{for } u_{L}\leq u_{R},\\ \max\limits_{u\in[u_{R},u_{L}]}g\left(u\right), & \text{for } u_{L}\geq u_{R}.\end{cases} \tag{3.2.4}$$

and similarly for the numerical flux F^{G} with respect to f. The superscript G refer to Godunov's method. We can use the hypothesis (H_{2}) and (H_{3}) on the fluxes f and g to get a much simpler expression than (3.2.4). Let θ_{g} and θ_{f} be either the maxima or the minima of g and f respectively. First consider fluxes of the type (H_{2}), that is, functions of the concave type [2]:

$$\begin{aligned}G^{G}\left(u_{L},u_{R}\right)&=\min\left\{G^{G}\left(u_{L},\theta_{g}\right),G^{G}\left(\theta_{g},u_{R}\right)\right\}\\&=\min\left\{g\left(\min\left\{u_{L},\theta_{g}\right\}\right),g\left(\max\left\{\theta_{g},u_{R}\right\}\right)\right\},\end{aligned} \tag{3.2.5}$$

$$\begin{aligned}F^{G}\left(u_{L},u_{R}\right)&=\min\left\{F^{G}\left(u_{L},\theta_{f}\right),F^{G}\left(\theta_{f},u_{R}\right)\right\}\\&=\min\left\{f\left(\min\left\{u_{L},\theta_{f}\right\}\right),f\left(\max\left\{\theta_{f},u_{R}\right\}\right)\right\}.\end{aligned} \tag{3.2.6}$$

Now consider the hypothesis (H_{3}), that is, fluxes of the convex type[2]:

$$\begin{aligned}G^{G}\left(u_{L},u_{R}\right)&=\max\left\{G^{G}\left(u_{L},\theta_{g}\right),G^{G}\left(\theta_{g},u_{R}\right)\right\}\\&=\max\left\{g\left(\max\left\{u_{L},\theta_{g}\right\}\right),g\left(\min\left\{\theta_{g},u_{R}\right\}\right)\right\},\end{aligned} \tag{3.2.7}$$

$$\begin{aligned} F^G(u_L,u_R) &= \max\left\{F^G(u_L,\theta_f),F^G(\theta_f,u_R)\right\} \\ &= \max\left\{f(\max\{u_L,\theta_f\}),f(\min\{\theta_f,u_R\})\right\}. \end{aligned} \tag{3.2.8}$$

We now consider the interface flux $\overline{F}$. The basic idea of the Godunov scheme is to use the solution of (3.1.1) to calculate the numerical fluxes. In the case of the interface flux, we must create a numerical flux that captures the (A,B)-entropy solutions. Following [3], and using (H_2), we define the interface numerical flux as:

$$\overline{F}^G_{AB}(u_L,u_R) = \min\left\{G^G(u_L,A),F^G(B,u_R)\right\}. \tag{3.2.9}$$

By using (H_3) instead, the interface numerical flux is given by

$$\overline{F}^G_{AB}(u_L,u_R) = \max\left\{G^G(u_L,A),F^G(B,u_R)\right\}. \tag{3.2.10}$$

We can simplify the two expression above in the same matter as done in [2]. Let a be defined by $g(a)=g(A)$ and b be defined by $f(b)=f(B)$. The interface fluxes (3.2.9) and (3.2.10) is rewritten to

$$\overline{F}^G_{AB}(u_L,u_R) = \min\left\{g(\min\{u_L,a\},f(\max\{b,u_R\}))\right\}, \tag{3.2.11}$$

and

$$\overline{F}^G_{AB}(u_L,u_R) = \max\left\{g(\max\{u_L,a\},f(\min\{b,u_R\}))\right\}, \tag{3.2.12}$$

respectively. This completes the Godunov scheme for approximating general (A,B)-entropy solutions. If we want to approximate the solutions given in [2, 12, 3, 4], we can do this by following the optimal connection theorem (see (2.2.42)):

- For (H_2)-fluxes

$$\begin{aligned} &a=A=\theta_g, \quad b=\theta_g^* \text{ where } f\left(\theta_g^*\right)=f\left(\bar{\theta}_g\right), && \text{if } g(\theta_g)\geq f(\theta_f), \\ &a=\theta_f^* \text{ where } g\left(\theta_f^*\right)=g\left(\bar{\theta}_f\right), \quad b=B=\theta_f, && \text{if } g(\theta_g)\leq f(\theta_f). \end{aligned}$$

- For (H_3)-fluxes

$$\begin{aligned} &a=A=\theta_g, \quad b=\theta_g^* \text{ where } f\left(\theta_g^*\right)=f\left(\bar{\theta}_g\right), && \text{if } g(\theta_g)\leq f(\theta_f), \\ &a=\theta_f^* \text{ where } g\left(\theta_f^*\right)=g\left(\bar{\theta}_f\right), \quad b=B=\theta_f, && \text{if } g(\theta_g)\geq f(\theta_f). \end{aligned}$$

As seen when comparing the minimal jump condition and the optimal connection condition, they give the same solution except when the fluxes intersect in a undercompressive matter, i.e. $f'(u_\chi)>0$ and $g'(u_\chi)<0$, where $u_\chi$denotes the point of intersection (see section 2.2.3.3). Thus, if we want to approximate the solutions given in [10, 11, 7, 8], we let

$$A=B=u_\chi,$$

when the the fluxes intersects undercompressively, and a and b is determined by $g(a) = g(A)$ and $f(b) = f(B)$.

The scheme is monotone and conservative, but not always consistent. We will show this in the following, starting with the consistency. Since the expression for F^G and G^G are equal we only investigate for G^G and suggest, without proof, the same properties for F^G.
We use the definition in section 3.1.3 on fluxes of concave type, i.e. satisfying (H_2), to prove consistency

$$G^G(\bar{u}, \bar{u}) = \min\{g(\min\{\bar{u}, \theta_g\}), g(\max\{\theta_g, \bar{u}\})\} = g(\bar{u}), \tag{3.2.13}$$

since $g(\bar{u}) \leq g(\theta_g)$ for all choices of $\bar{u} \in [s, S]$. If the fluxes are of convex type, i.e. satisfying (H_3), we get

$$G^G(\bar{u}, \bar{u}) = \max\{g(\max\{\bar{u}, \theta_g\}), g(\min\{\theta_g, \bar{u}\})\} = g(\bar{u}), \tag{3.2.14}$$

since $g(\bar{u}) \geq g(\theta_g)$ for all choices of $\bar{u} \in [s, S]$. Thus the numerical fluxes away from $x = 0$ is consistent. Now, we investigate the interface flux $\overline{F}^G$ and see if it is consistent, starting with(H_2)-fluxes:

$$\overline{F}^G_{AB}(\bar{u}, \bar{u}) = \min\{g(\min\{\bar{u}, a\}), f(\max\{b, \bar{u}\})\}. \tag{3.2.15}$$

$\overline{F}^G(\bar{u}, \bar{u})$ is not equal to $g(\bar{u})$ or $f(\bar{u})$ when $a < \bar{u} < b$, thus it is not consistent for all $\bar{u} \in [s, S]$. If the fluxes satisfy (H_3) we instead get

$$\overline{F}^G_{AB}(u_L, u_R) = \max\{g(\max\{\bar{u}, a\}), f(\min\{b, \bar{u}\})\}. \tag{3.2.16}$$

Again $\overline{F}^G(\bar{u}, \bar{u})$ need not be equal to $g(\bar{u})$ or $f(\bar{u})$. When $b \leq \bar{u} \leq a$, $\overline{F}^G(\bar{u}, \bar{u})$ is not consistent with neither $g(\bar{u})$ or $f(\bar{u})$.

We now check the monotonicity for the scheme. When the scheme is written as $\mathbf{u}^{n+1} = \mathbf{H}(\mathbf{u}^n)$, one element of the matrix $\mathbf{H}$ for a fixed time is

$$H_j(\mathbf{u}) = u_j - \lambda\left[\mathcal{F}^G(u_j, u_{j+1}) - \mathcal{F}^G(u_{j-1}, u_j)\right]. \tag{3.2.17}$$

Away from the interface ($j \neq \pm 1$) the scheme is the normal Godunov scheme, and thus monotonicity has been proved e.g. in [1]. Therefore, we will only prove monotonicity for the scheme at the interface ($x = 0$) i.e. when $j = \pm 1$. In the following we focus on $j = -1$ involving only G^G and $\overline{F}^G$.
We start of with (H_2)-fluxes, and write the matrix $\mathbf{H}$ when $j = -1$

$$H_{-1}(\mathbf{u}) = u_{-1} - \lambda\left[\overline{F}^G_{AB}(u_{-1}, u_1) - G^G(u_{-2}, u_{-1})\right]. \tag{3.2.18}$$

To calculate the Jacobian $\mathbf{H}'(\mathbf{u})$, we need the derivative of the Godunov fluxes given above. To calculate the derivatives of $\overline{F}^G$ we introduce some simplified notations

$$z_1 = \min\{u_L, a\},$$

$$z_2 = \max\{b, u_R\},$$

denoting $u_{-1} = u_L$ and $u_1 = u_R$ (in general $u_{j-1} = u_L$ and $u_j = u_R$ for G^G, and $u_j = u_L$ and $u_{j+1} = u_R$ for F^G). With these notations the interface flux defined in (3.2.11) can be written as

$$\overline{F}^G(u_L, u_R) = \begin{cases} g(z_1), & \text{if } g(z_1) \le f(z_2), \\ f(z_2), & \text{if } f(z_2) \le g(z_1). \end{cases} \tag{3.2.19}$$

The derivative with respect to u_L is then

$$\overline{F}^G_{u_L}(u_L, u_R) = \begin{cases} g'(u_L) \ge 0, & \text{if } g(z_1) \le f(z_2) \text{ and } u_L \le a, \\ 0, & \text{otherwise.} \end{cases} \tag{3.2.20}$$

and the derivative with respect to u_R is

$$\overline{F}^G_{u_R}(u_L, u_R) = \begin{cases} f'(u_R) \le 0, & \text{if } f(z_2) \le g(z_1) \text{ and } u_R \ge b, \\ 0, & \text{otherwise.} \end{cases} \tag{3.2.21}$$

We introduce similar notations for G^G

$$w_1 = \min\{u_L, \theta_g\},$$

$$w_2 = \max\{\theta_g, u_R\},$$

simplifying our expressions. Using this notation, the derivatives for G^G is

$$G^G_{u_L}(u_L, u_R) = \begin{cases} g'(u_L) \ge 0, & \text{if } g(w_1) \le g(w_2) \text{ and } u_L \le \theta_g, \\ 0, & \text{otherwise.} \end{cases} \tag{3.2.22}$$

$$G^G_{u_R}(u_L, u_R) = \begin{cases} g'(u_R) \le 0, & \text{if } g(w_2) \le g(w_1) \text{ and } u_R \ge \theta_g, \\ 0, & \text{otherwise.} \end{cases} \tag{3.2.23}$$

Now we have all the information we need to calculate the Jacobian $\mathbf{H}'(\mathbf{u})$. As noted in section 3.1.3, we only need the derivative of $H_j(\mathbf{u})$ with respect to u_{j-1} , u_j and u_{j+1}. For $j = -1$, these derivatives are

$$\frac{\partial H_{-1}}{\partial u_{-2}} = \lambda G^G_{u_L}(u_{-2}, u_{-1}) \ge 0, \tag{3.2.24}$$

$$\frac{\partial H_{-1}}{\partial u_1} = -\lambda \overline{F}^G_{u_R}(u_{-1}, u_1) \ge 0, \tag{3.2.25}$$

from (3.2.22) and (3.2.21) respectively. Further

$$\frac{\partial H_{-1}}{\partial u_{-1}} = 1 - \lambda \left[\overline{F}^G_{u_L}(u_{-1}, u_1) - G^G_{u_R}(u_{-2}, u_{-1}) \right]. \tag{3.2.26}$$

If $g'(u_{-1}) \neq 0$, then according to (3.2.20) and (3.2.23), only one of the numerical fluxes will be equal to $g(u_{-1})$. Thus we have

$$\frac{\partial H_{-1}}{\partial u_{-1}} \geq 1 - |g'(u_{-1})| \geq 0, \tag{3.2.27}$$

when the CFL-condition is satisfied. As noted above, similar results follow for $j = 1$, when F and $\overline{F}$ are involved, hence the scheme is monotone for fluxes of concave type. The procedure for proving monotonicity for (H_3)-fluxes is similar to the proof above and therefore is omitted.

In [3, 2] they use *the singular mapping technique* introduced by Temple in [24] to prove convergence. The essence of the convergence proof is using the singular mapping function to obtain a limit function u, then using the Lax-Wendroff theorem proving that u is a weak solution. From here, consistency with the entropy conditions, both away from and at $x = 0$, is proved, thus we have uniqueness of the limit solutions. The complete proof is found in [2] for the Godunov scheme with respect to the entropy condition in [4], and in [3] for the (A, B)-entropy solutions, though the proof there relies heavily on the procedure in [2]. Thus the scheme converges, in spite of non-consistency for the interface flux.

3.3 Engquist-Osher's Method

Upwind differencing for the linear differential equation $u_t + au_x = 0$ can be generalized for the nonlinear differential equation $u_t + f(u)_x = 0$. If we also assume that the solution is a rarefaction wave, the entropy condition is always satisfied. This is the basic idea of *the Engquist-Osher method* (EO). See e.g. [17] for a description of the method for conservation laws without the spatial discontinuity. As before, we start with the numerical fluxes away from the discontinuity at $x = 0$, and we let $u_L = u_{j-1}$ and $u_R = u_j$ for a fixed t

$$G^{EO}(u_L, u_R) = \frac{1}{2}[g(u_L) + g(u_R)] - \frac{1}{2}\int_{u_L}^{u_R} |g'(w)|dw, \tag{3.3.1}$$

and if we let $u_L = u_j$ and $u_R = u_{j+1}$

$$F^{EO}(u_L, u_R) = \frac{1}{2}[f(u_L) + f(u_R)] - \frac{1}{2}\int_{u_L}^{u_R} |f'(w)|dw. \tag{3.3.2}$$

This is just one of many ways of describing the numerical fluxes, but for comparison with the interface flux $\overline{F}$ this is the best way. It is easy to check that for most cases, the Engquist-Osher flux is equal to the Godunov flux, i.e. to the upwind flux. The only case where the Engquist-Osher method and the

Godunov method differ is when $h'(u_L) > 0 > h'(u_R)$ (for a flux function h in a general conservation law $u_t + h(u)_x = 0$). Here EO produces

$$h(u_L) + h(u_R) - h(u_s),$$

where u_s is the value of u when $h'(u) = 0$, instead of simply $h(u_L)$ or $h(u_R)$ given by the Godunov scheme. The obvious advantage of EO is that no Riemann solver is involved.
To get an expression for the interface flux, we could have separated the integral in the EO flux with a properly selected value u_M. If $u_L = u_{-1}$ and $u_R = u_1$, this results in

$$\begin{aligned}\overline{F}^{EO}(u_L, u_R) =& \frac{1}{2}\left[g(u_L) + f(u_R)\right] \\ & - \frac{1}{2}\left[\int_{u_L}^{u_M} |g'(w)|dw + \int_{u_M}^{u_R} |f'(w)|dw\right].\end{aligned} \tag{3.3.3}$$

But since we need a condition for selecting u_M, we rather modify the EO flux such that we capture the (A, B)-entropy connection at the interface, as we did for the Godunov scheme in section 3.2. This is done in [9]. The interface flux is given by

$$\begin{aligned}\overline{F}^{EO}_{AB}(u_L, u_R) =& \frac{1}{2}\left[\tilde{g}(u_L) + \tilde{f}(u_R)\right] \\ & - \frac{1}{2}\left[\int_{B}^{u_R} |\tilde{f}'(w)|dw - \int_{A}^{u_L} |\tilde{g}'(w)|dw\right],\end{aligned} \tag{3.3.4}$$

where the modified flux expressions for (H_2)-fluxes is given as

$$\tilde{f}(u) := \min\{f(u), f(B)\},$$
$$\tilde{f}'(u) := \begin{cases} 0, & \text{if } f(u) \geq f(B), \\ f'(u), & \text{if } f(u) \leq f(B), \end{cases}$$

and

$$\tilde{g}(u) := \min\{g(u), g(A)\},$$
$$\tilde{g}'(u) := \begin{cases} 0 & \text{if } g(u) \geq g(A), \\ g'(u) & \text{if } g(u) \leq g(A). \end{cases}$$

For (H_3)-fluxes the modified flux functions are instead

$$\tilde{f}(u) := \max\{f(u), f(B)\},$$
$$\tilde{f}'(u) := \begin{cases} f'(u), & \text{if } f(u) \geq f(B), \\ 0, & \text{if } f(u) \leq f(B), \end{cases}$$

and

$$\tilde{g}(u) := \max\{g(u), g(A)\},$$
$$\tilde{g}'(u) := \begin{cases} g'(u), & \text{if } g(u) \geq g(A), \\ 0 & \text{if } g(u) \leq g(A). \end{cases}$$

Although the fluxes defined in (3.3.1),(3.3.2) and (3.3.4) are nice for analytical purposes, when implementing the EO scheme it is more favorable writing the expression for the flux function for each case of the flux derivatives. We will see that this gives us a simplified version of the EO fluxes. Also, for the interface flux it is not easy to know what the numerical flux expression will look like for each case of the flux derivatives just by looking at formula (3.3.4). Therefore, we have derived the full expressions in Appendix A, and in short, the answers to all the cases are either $g(u_L)$, $g(A)$, $f(u_R)$, $f(B)$ or $g(u_L) + f(u_R) - g(A)$. Thus, if we again let a be such that $g(a) = g(A)$, and b be such that $f(b) = f(B)$, the above formulations can be simplified like the formulations made for the Godunov scheme (c.f. section 3.2) . For flux functions satisfying (H_2), the EO flux can be simplified to

$$\overline{F}^{EO}_{AB}(u_L, u_R) = g(\min\{u_L, a\}) + f(\max\{b, u_R\}) - g(A), \tag{3.3.5}$$

and for fluxes satisfying (H_3)

$$\overline{F}^{EO}_{AB}(u_L, u_R) = g(\max\{u_L, a\}) + f(\min\{b, u_R\}) - g(A). \tag{3.3.6}$$

This simplification can also be done for the flux functions away from $x = 0$. As before, let θ_f and θ_g be the maxima or minima for f and g satisfying (H_2) or (H_3), respectively. For (H_2) fluxes

$$\begin{aligned} G^{EO}(u_L, u_R) &= g(\min\{u_L, \theta_g\}) + g(\max\{\theta_g, u_R\}) - g(\theta_g), \\ F^{EO}(u_L, u_R) &= f(\min\{u_L, \theta_f\}) + f(\max\{\theta_f, u_R\}) - f(\theta_f), \end{aligned} \tag{3.3.7}$$

and (H_3) fluxes

$$\begin{aligned} G^{EO}(u_L, u_R) &= g(\max\{u_L, \theta_g\}) + g(\min\{\theta_g, u_R\}) - g(\theta_g), \\ F^{EO}(u, u_R) &= f(\max\{u_L, \theta_f\}) + f(\min\{\theta_f, u_R\}) - f(\theta_f), \end{aligned} \tag{3.3.8}$$

With these formulation, implementation of the method is easy. The only drawback is finding the two values a and b. The advantage of the EO scheme is that no Riemann solver is involved, but as we must choose which (A, B)-entropy solution we want to approximate, a knowledge of the Riemann solution is necessary.

We check consistency and monotonicity for the scheme, starting with consistency. Again, we only investigate the fluxes G^{EO} and $\overline{F}^{EO}$, omitting F^{EO} due to similarity with G^{EO}. Inserting $u_L = u_R = \overline{u}$ in G^{EO} gives

$$\begin{aligned} G^{EO}(\bar{u}, \bar{u}) &= g(\min\{\bar{u}, \theta_g\}) + g(\max\{\theta_g, \bar{u}\}) - g(\theta_g) \\ &= g(\bar{u}) + g(\theta_g) - g(\theta_g) = g(\bar{u}). \end{aligned} \tag{3.3.9}$$

This is valid for both (H_2)-fluxes and (H_3)-fluxes. For the interface flux $\overline{F}^{EO}$ we get, in the case of (H_2)-fluxes

$$\overline{F}^{EO}_{AB}(\bar{u},\bar{u}) = g(\min\{\bar{u},a\}) + f(\max\{b,\bar{u}\}) - g(A), \tag{3.3.10}$$

which is not consistent when $a < \bar{u} < b$ and $b < \bar{u} < a$. For (H_3)-fluxes, we get

$$\overline{F}^{EO}_{AB}(\bar{u},\bar{u}) = g(\max\{\bar{u},a\}) + f(\min\{b,\bar{u}\}) - g(A), \tag{3.3.11}$$

again, from direct calculations, not consistent when $a < \bar{u} < b$ and $b < \bar{u} < a$. Thus, as for the Godunov fluxes, EO-fluxes are not always consistent with either f or g at the interface.
We check monotonicity, the same way as for the Godunov scheme, only for $j = -1$. Away from the interface, the scheme is equal to the normal EO scheme, hence monotonicity can be found in e.g. [1]. As before we prove monotonicity for (H_2)-fluxes, as the proof is similar for (H_3)-fluxes. The matrix $\mathbf{H}(\mathbf{u})$ for a fixed time when $j = -1$ is

$$H_{-1}(\mathbf{u}) = u_{-1} - \lambda\left[\overline{F}^{EO}_{AB}(u_{-1},u_1) - G^{EO}(u_{-2},u_{-1})\right]. \tag{3.3.12}$$

We again denote $u_L = u_j$ and $u_R = u_{j+1}$ in general for G^{EO} and F^{EO}, and $u_L = u_{-1}$ and $u_R = u_1$ for $\overline{F}^{EO}$, and calculate their derivatives, starting with $\overline{F}^{EO}$

$$\overline{F}^{EO}_{u_L}(u_L,u_R) = \begin{cases} g'(u_L) \geq 0, & \text{if } u_L \leq a, \\ 0, & \text{otherwise.} \end{cases} \tag{3.3.13}$$

$$\overline{F}^{EO}_{u_R}(u_L,u_R) = \begin{cases} f'(u_R) \leq 0, & \text{if } u_R \geq b, \\ 0, & \text{otherwise.} \end{cases} \tag{3.3.14}$$

The derivatives for G^{EO} are

$$G^{EO}_{u_L}(u_L,u_R) = \begin{cases} g'(u_L) \geq 0, & \text{if } u_L \leq \theta_g, \\ 0, & \text{otherwise.} \end{cases} \tag{3.3.15}$$

$$G^{EO}_{u_R}(u_L,u_R) = \begin{cases} g'(u_R) \leq 0, & \text{if } u_R \geq \theta_g, \\ 0, & \text{otherwise} \end{cases} \tag{3.3.16}$$

Note that the derivatives are almost the same as the derivatives calculated for the Godunov scheme, thus we can expect similar results. We check the derivatives of $H_{-1}(\mathbf{u})$ with respect to u_{-2} , u_{-1} and u_1

$$\frac{\partial H_{-1}}{\partial u_{-2}} = \lambda G^{EO}_{u_L}(u_{-2},u_{-1}) \geq 0, \tag{3.3.17}$$

$$\frac{\partial H_{-1}}{\partial u_1} = -\lambda \overline{F}^{EO}_{u_R}(u_{-1},u_1) \geq 0, \tag{3.3.18}$$

These results follow from (3.3.15) and (3.3.14). Further

$$\frac{\partial H_{-1}}{\partial u_{-1}} = 1 - \lambda \left[\overline{F}^{EO}_{u_L} (u_{-1}, u_1) - G^{EO}_{u_R} (u_{-2}, u_{-1}) \right]. \tag{3.3.19}$$

From (3.3.13) and (3.3.16) we see that only one of $\overline{F}^{EO}_{u_L} (u_{-1}, u_1)$ and $G^{EO}_{u_R} (u_{-2}, u_{-1})$ can be equal to $g'(u_{-1})$, and since $\overline{F}^{EO}_{u_L} (u_{-1}, u_1) \geq 0$ and $G^{EO}_{u_R} (u_{-2}, u_{-1}) \leq 0$, we write

$$\frac{\partial H_{-1}}{\partial u_{-1}} \geq 1 - |g'(u_{-1})| \geq 0, \tag{3.3.20}$$

if the CFL-condition is satisfied. Hence the scheme is monotone under the CFL-condition.

Convergence of this scheme is proved in [9]. Unlike the convergence proof in [2] and [18], this proof does not contain the singular mapping approach due to their formulation of the entropy jump condition (c.f. section 2.2.2). Instead they can use a spatial variation bound away from $x = 0$ to obtain a limit function u. From here, Lax-Wendroff-type calculations are done to prove that the limit function u converges to the weak solutions both away from $x = 0$ and at $x = 0$.

3.4 The Local Lax-Friedrichs Method

The simplest conservative scheme is the Lax-Friedrichs (LxF) scheme. This is just a central scheme where the value u^n_j is replaced by the average $\frac{1}{2}\left(u^n_{j-1} + u^n_{j+1}\right)$. Hence the scheme for a general hyperbolic conservation law, $u_t + h(u)_x = 0$, is

$$u^{n+1}_j = \frac{1}{2}\left(u^n_{j-1} + u^n_{j+1}\right) - \frac{\Delta t}{2\Delta x}\left[h\left(u^n_{j+1}\right) - h\left(u^n_{j-1}\right)\right]. \tag{3.4.1}$$

It can be written in conservative form (3.1.6) if we define the numerical flux

$$\mathcal{H}^n_{j+1/2} = \mathcal{H}(u_L, u_R) = \frac{1}{2}\left[h(u_L) + h(u_R) - \frac{\Delta x}{\Delta t}(u_R - u_L)\right]. \tag{3.4.2}$$

From known theory, see e.g. [17], we know that Lax-Friedrichs method gives extensive numerical dissipation. However, the numerical dissipation can be reduced significantly by replacing $\Delta x/\Delta t$ in (3.4.2) by a locally determined value $a_{j\pm1/2}$. We look at the numerical fluxes away from $x = 0$, and denote $u_L = u_{j-1}$ and $u_R = u_j$ when considering G, and $u_L = u_j$ and $u_R = u_{j+1}$ when considering F, for a fixed time. Starting with $j \leq -1$:

$$G^{LLxF}(u_L, u_R) = \frac{1}{2}\left[g(u_L) + g(u_R) - a_{j-1/2}(u_R - u_L)\right], \tag{3.4.3}$$

where

$$a_{j-1/2} = \max\left\{\left|g'\left(u\right)\right|\right\}, \quad \forall u \text{ between } u_L \text{and } u_R.$$

For $j \geq 1$

$$F^{LLxF}\left(u_L, u_R\right) = \frac{1}{2}\left[f\left(u_L\right) + f\left(u_R\right) - a_{j+1/2}\left(u_R - u_L\right)\right], \tag{3.4.4}$$

where

$$a_{j+1/2} = \max\left\{\left|f'\left(u\right)\right|\right\}, \quad \forall u \text{between } u_L \text{and } u_R.$$

This is called the *Local Lax-Friedrichs* (LLxF) *method* or *Rusanov's method* after V.V. Rusanov [21]. The value $a_{j+1/2}$ represents the local maximum speeds at each cells.
Following [23], a conservative scheme can be written in the form (for an arbitrary flux function $h\left(u\right)$)

$$u_j^{n+1} = u_j^n - \frac{\lambda}{2}\left[h\left(u_{j+1}^n\right) - h\left(u_{j-1}^n\right)\right] + \frac{1}{2}\left[\Delta\left(Q_{j-1/2}\Delta u_{j-1/2}\right)\right], \tag{3.4.5}$$

where $\Delta q_{j+1/2} = q_{j+1} - q_j$ (q is an arbitrary variable), $\lambda = \Delta t/\Delta x$ and $Q_{j-1/2}$ is called the *numerical viscosity coefficient*. It is easy to check that for the Lax-Friedrichs scheme $Q_{j-1/2} \equiv 1$, and for the Local Lax-Friedrichs scheme $Q_{j-1/2} = \lambda a_{j-1/2}$. Under the CFL condition $\lambda \cdot \max\left|h'\left(u\right)\right| \leq 1$ the numerical dissipation of LLxF will, at the worst, be equal to LxF.
We would also like to apply the LLxF flux to the interface flux. This is done in a straightforward manner:

$$\overline{F}^{LLxF}\left(u_L, u_R\right) = \frac{1}{2}\left[g\left(u_L\right) + f\left(u_R\right) - \overline{a}\left(u_R - u_L\right)\right], \tag{3.4.6}$$

where

$$\overline{a} = \max\left\{\left|g'\left(u\right)\right|, \left|f'\left(u\right)\right|\right\}, \quad \forall u \text{between } u_L \text{and } u_R,$$

and $u_L = u_{-1}$ and $u_R = u_1$, as usual.

We again investigate the scheme for consistency and monotonicity, and as before we concentrate on the fluxes G^{LLxF} and $\overline{F}^{LLxF}$. We begin by checking consistency for G^{LLxF}

$$G^{LLxF}\left(\overline{u}, \overline{u}\right) = \frac{1}{2}\left[g\left(\overline{u}\right) + g\left(\overline{u}\right) - \left|g'\left(\overline{u}\right)\right|\left(\overline{u} - \overline{u}\right)\right] = g\left(\overline{u}\right), \tag{3.4.7}$$

and for $\overline{F}^{LLxF}$ the calculations are

$$\begin{aligned}\overline{F}^{LLxF}\left(\overline{u}, \overline{u}\right) &= \frac{1}{2}\left[g\left(\overline{u}\right) + f\left(\overline{u}\right) - \max\left\{g'\left(\overline{u}\right), f\left(\overline{u}\right)\right\}\left(\overline{u} - \overline{u}\right)\right] \\ &= \frac{1}{2}\left(g\left(\overline{u}\right) + f\left(\overline{u}\right)\right).\end{aligned} \tag{3.4.8}$$

Thus, $\overline{F}^{LLxF}(\bar{u}, \bar{u})$ is not consistent with $f(\bar{u})$ or $g(\bar{u})$ unless $g(\bar{u}) = f(\bar{u})$.
To prove monotonicity for the scheme, we need to calculate the derivatives of $H_j(\mathbf{u})$ with respect to u_{j-1}, u_j and u_{j+1}. But since the numerical fluxes contains $|f'(u)|$ and/or $|g'(u)|$, the derivative of $H_j(\mathbf{u})$ can be difficult to analyze. For j away from the interface, monotonicity can easily be proved using the properties of *E schemes* (see [19]). We are then avoiding calculation of the derivatives of H_j, but unfortunately E schemes are only applied for hyperbolic conservation laws without the discontinuous flux function. Therefore, monotonicity is not proved for this scheme, but since it is a first order scheme and is monotone without the spatial discontinuity, we anticipate that this scheme also is monotone for our problem.

Convergence of this scheme for the problem (3.1.1) has not been proved, but for a conservation law *without* the spatial discontinuity the scheme converges to the entropy solution presented in section 2.1.2.2. It can be shown that the entropy solution in section 2.1.2.2, can also be derived from what is called vanishing viscosity entropy solution (or viscous profile entropy solution in section 2.2.3.3). Since the LLxF scheme converges for conservation laws without the spatial discontinuity, and the entropy solution there is the same as the vanishing viscosity entropy solution, we anticipate the LLxF scheme to converge to the minimal jump condition for conservation laws with the discontinuous flux.

The main advantage of the LLxF scheme, and also LxF, is that no approximate Riemann solver is necessary. It is much simpler to implement and is general in its application. Many higher order schemes is based on the Lax-Friedrichs scheme e.g. the Kurganov and Tadmor central scheme [14].

3.5 Upstream Mobility Finite Difference Scheme

For calculating the flow in porous medium, the petroleum engineers invented a scheme based on simple physical considerations. The main idea of the scheme is calculating the flux values by considering the direction of the flow . See e.g. [22, 5].
In reservoir simulation the flow of incompressible, immiscible fluids is determined by the saturation equation and Darcy's law in one dimension, given by the following equations (c.f. section 2.2.3.1 for description of variables and subscripts)

$$\phi \frac{\partial S_l}{\partial t} + \frac{\partial v_l}{\partial x} = 0, \tag{3.5.1}$$

$$v_l = -K \frac{k_l}{\mu_l} \left(\frac{dp}{dx} - \rho_l g \right). \tag{3.5.2}$$

Capillary pressure is neglected, the reservoir has constant porosity, ϕ, and absolute permeability, K. Finally, μ_l is assumed constant and g indicates the impact of gravity. If we discretize the equations above and combine them, we get the following equation(c.f [22])

$$\begin{aligned}\Delta x\phi\frac{S_{l,i}^{n+1}-S_{l,i}^{n}}{dt} =&\frac{Kk_l^L}{\mu_l}\frac{\left(p_{i-1}^{n+1}-p_i^{n+1}+\rho_l g\Delta x\right)}{\Delta x}\\ &+\frac{Kk_l^R}{\mu_l}\frac{\left(p_{i+1}^{n+1}-p_i^{n+1}-\rho_l g\Delta x\right)}{\Delta x}.\end{aligned} \tag{3.5.3}$$

Note that the pressure is evaluated implicitly, thus it is an IMPES (Implicit Pressure, Explicit Saturation) method, but generally it could have been calculated differently. This is, however, not important in our analysis, as it is the physical principle we are interested in. The superscripts R and L indicates that the relative permeabilities $k_l\left(S_l\right)$ must be evaluated in the upstream direction. This must not be confused with the notation earlier, where it indicated the side of $x=0$. In (3.5.3) the upstream direction is based on the flow direction. Thus, $k_l^{R,L}$ is evaluated at the upstream saturation S_l^n in cell $i\pm1$ if

$$p_{i\pm1}^{n+1}-p_i^{n+1}>\pm\rho_l g\Delta x, \tag{3.5.4}$$

and in cell i otherwise. Here, R corresponds to the plus sign in (3.5.4), and L to the minus sign. A reservoir simulator usually solve (3.5.3) and (3.5.4) together with the constraint $S_{nw}^{n+1}+S_w^{n+1}=1$, but for analysis purposes, we need the equations in conservation form and not have the upstream condition depending on pressure gradients. As shown in section 2.2.3.1, (3.5.1) and (3.5.2) can combine and give the saturation equation

$$\phi\frac{\partial S_w}{\partial t}+\frac{\partial F}{\partial x}=0, \tag{3.5.5}$$

where

$$F\left(S_w\right)=\frac{\lambda_w\left(S_w\right)}{\lambda_w\left(S_w\right)+\lambda_{nw}\left(S_w\right)}\left[v+g\left(\rho_w-\rho_{nw}\right)\lambda_{nw}\left(S_w\right)\right], \tag{3.5.6}$$

and as usual, the effective mobilities are defined as

$$\lambda_l\left(S_w\right)=\frac{Kk_l\left(S_w\right)}{\mu_l}.$$

We discretize (3.5.5) in the wanted conservation form

$$S_w^{n+1}=S_w^n-\frac{\Delta t}{\phi\Delta x}\left[F^R-F^L\right], \tag{3.5.7}$$

The pressure dependence is removed by using the definition of the total Darcy velocity as follows

$$\begin{aligned} v = v_{nw} + v_w &= \lambda_t^L \left[\frac{p_{i-1}^{n+1} - p_i^{n+1} - \rho_t^L g \Delta x}{\Delta x} \right] \\ &= -\lambda_t^R \left[\frac{p_{i+1}^{n+1} - p_i^{n+1} - \rho_t^R g \Delta x}{\Delta x} \right] \end{aligned} \tag{3.5.8}$$

where v is a known constant value, i.e. inflow velocity. The last equality is due to mass conservation, that is, the total Darcy velocity is constant through the reservoir, thus it can be calculated using the left or right upstream direction. The total mobility, λ_t, and the mobility-weighted density term, ρ_t, is defined as

$$\lambda_t = \frac{K k_w}{\mu_w} + \frac{K k_{nw}}{\mu_{nw}} = \lambda_w + \lambda_{nw}, \tag{3.5.9}$$

and

$$\rho_t \cdot \lambda_t = \frac{K k_w}{\mu_w} \rho_w + \frac{K k_{nw}}{\mu_{nw}} \rho_{nw}, \tag{3.5.10}$$

Consider for now cell $i-1$ (corresponding to superscript L). We can express the upstream condition, without the pressure gradients for the wetting phase, by manipulating (3.5.8), which results in the following

$$p_{i-1}^{n+1} - p_i^{n+1} + \rho_w g \Delta x = \frac{\Delta x}{\lambda_t^L} \left[v + \lambda_{nw}^L g \left(\rho_w - \rho_{nw} \right) \right], \tag{3.5.11}$$

and for the non-wetting phase

$$p_{i-1}^{n+1} - p_i^{n+1} + \rho_{nw} g \Delta x = \frac{\Delta x}{\lambda_t^L} \left[v + \lambda_w^L g \left(\rho_{nw} - \rho_w \right) \right]. \tag{3.5.12}$$

Thus, for cell $i-1$ we use saturation $\left(S_w^n\right)_{i-1}$ if

$$v + \lambda_{nw}^L g \left(\rho_w - \rho_{nw} \right) > 0,$$

or $\left(S_w^n\right)_i$ if

$$v + \lambda_{nw}^L g \left(\rho_w - \rho_{nw} \right) < 0,$$

for calculating k_w^L, and similarly for k_{nw}^L. Because of conservation for each cell $\left(k_l^R\right)_i = \left(k_l^L\right)_{i+1}$, hence the condition applies for cell $i+1$ as well.

We can now use the observations made above in the approximation of the numerical fluxes. Away from $x = 0$ they are calculated from the following

$$\begin{aligned} G^{UM}\left(u_L, u_R\right) &= \frac{\lambda_w^{L*}}{\lambda_w^{L*} + \lambda_{nw}^{L*}} \left[v + \left(g_w - g_{nw} \right) \lambda_{nw}^{L*} \right], \\ \lambda_l^{L*} &= \begin{cases} \lambda_l^L\left(u_L\right), & \text{if } v + \left(g_l - g_i \right) \lambda_i^{L*} > 0,\ i, l = w, nw, \\ \lambda_l^L\left(u_R\right), & \text{if } v + \left(g_l - g_i \right) \lambda_i^{L*} \leq 0,\ i, l = w, nw, \end{cases} \quad i \neq l, \end{aligned} \tag{3.5.13}$$

and

$$
\begin{aligned}
F^{UM}(u_L, u_R) &= \frac{\lambda_w^{R*}}{\lambda_w^{R*} + \lambda_{nw}^{R*}} \left[v + (g_w - g_{nw}) \lambda_w^{R*} \right], \\
\lambda_l^{R*} &= \begin{cases} \lambda_l^R(u_L), & \text{if } v + (g_l - g_i)\lambda_i^{R*} > 0,\ i,l = w, nw, \\ \lambda_l^R(u_R), & \text{if } v + (g_l - g_i)\lambda_i^{R*} \le 0,\ i,l = w, nw, \end{cases} \quad i \neq l.
\end{aligned} \tag{3.5.14}
$$

Again, $u_L = u_{j-1}$ and $u_R = u_j$ for G^{UM}, and $u_L = u_j$ and $u_R = u_{j+1}$ for F^{UM} at a fixed time. The superscripts R (right) and L (left) now denotes on which side of $x = 0$ the mobility functions are defined. We see from formulas (3.5.13) and (3.5.14) that we must use the saturation values which is upstream with respect to the direction of the flow in the calculation of the mobility functions λ. The flow direction of phase l is determined by the sign of $v + (g_l - g_i)\lambda_i^{R,L*}$, but this is a implicit formula since $\lambda_i^{R,L*}$ depend on $\lambda_l^{R,L*}$. In [5] the authors give explicit formulas for calculating the mobility functions, thus simplifying the calculations of the numerical fluxes. By ordering the phases by increasing weights we get the following formulae for calculating the mobility functions:

Case 1: $g_w \le g_{nw}$

We define the quantities

$$
\theta_1 = v + (g_w - g_{nw})\lambda_{nw}^{R,L}(u_L), \quad \theta_2 = v + (g_{nw} - g_w)\lambda_w^{R,L}(u_R).
$$

Clearly $\theta_1 \le \theta_2$ since $g_w \le g_{nw}$. We can now define the explicit formulae

$$
\begin{aligned}
&1.\ 0 \le \theta_1 \le \theta_2 \quad \Leftrightarrow \quad \lambda_w^{R,L*} = \lambda_w^{R,L}(u_L), \quad \lambda_{nw}^{R,L*} = \lambda_{nw}^{R,L}(u_L), \\
&2.\ \theta_1 \le 0 \le \theta_2 \quad \Leftrightarrow \quad \lambda_w^{R,L*} = \lambda_w^{R,L}(u_R), \quad \lambda_{nw}^{R,L*} = \lambda_{nw}^{R,L}(u_L), \\
&3.\ \theta_1 \le \theta_2 \le 0 \quad \Leftrightarrow \quad \lambda_w^{R,L*} = \lambda_w^{R,L}(u_R), \quad \lambda_{nw}^{R,L*} = \lambda_{nw}^{R,L}(u_R),
\end{aligned}
$$

Case 2: $g_w \ge g_{nw}$

Again we define the quantities

$$
\theta_1 = v + (g_w - g_{nw})\lambda_{nw}^{R,L}(u_R), \quad \theta_2 = v + (g_{nw} - g_w)\lambda_w^{R,L}(u_L).
$$

Now, $\theta_1 \ge \theta_2$ since $g_1 \ge g_2$. The explicit formulae are

$$
\begin{aligned}
&1.\ 0 \le \theta_2 \le \theta_1 \quad \Leftrightarrow \quad \lambda_w^{R,L*} = \lambda_w^{R,L}(u_L), \quad \lambda_{nw}^{R,L*} = \lambda_{nw}^{R,L}(u_L), \\
&2.\ \theta_2 \le 0 \le \theta_1 \quad \Leftrightarrow \quad \lambda_w^{R,L*} = \lambda_w^{R,L}(u_L), \quad \lambda_{nw}^{R,L*} = \lambda_{nw}^{R,L}(u_R), \\
&3.\ \theta_2 \le \theta_1 \le 0 \quad \Leftrightarrow \quad \lambda_w^{R,L*} = \lambda_w^{R,L}(u_R), \quad \lambda_{nw}^{R,L*} = \lambda_{nw}^{R,L}(u_R),
\end{aligned}
$$

The direction of the flow is calculated in each cell by the quantities θ_1 and θ_2, and by evaluating their signs we know which saturation value to use for the mobility functions. Note that the above definition apply to both F^{UM} and G^{UM}, hence the superscript R, L. At $x = 0$ the interface numerical flux is calculated as follows (see [18]):

$$\begin{aligned} \overline{F}^{UM}(u_L, u_R) &= \frac{\lambda_w^*}{\lambda_w^* + \lambda_{nw}^*}\left[v + (g_w - g_{nw})\,\lambda_{nw}^*\right], \\ \lambda_l^* &= \begin{cases} \lambda_l^L(u_L), & \text{if } v + (g_l - g_i)\,\lambda_i^* > 0,\ i, l = w, nw, \\ \lambda_l^R(u_R), & \text{if } v + (g_l - g_i)\,\lambda_i^* \le 0,\ i, l = w, nw, \end{cases} i \neq l. \end{aligned} \tag{3.5.15}$$

Like F^{UM} and G^{UM} the interface flux must be calculated using the mobility values which is upstream with respect to the flow of the corresponding phases. And as before, (3.5.15) is a implicit formula, but in [18] explicit formulae is given:

Case 1: $g_w \le g_{nw}$

We define the quantities

$$\theta_1 = v + (g_w - g_{nw})\,\lambda_{nw}^L(u_L), \quad \theta_2 = v + (g_{nw} - g_w)\,\lambda_w^R(u_R).$$

$\theta_1 \le \theta_2$ since $g_w \le g_{nw}$. The explicit formulae are now

1. $0 \le \theta_1 \le \theta_2 \quad \Leftrightarrow \quad \lambda_w^* = \lambda_w^L(u_L), \quad \lambda_{nw}^* = \lambda_{nw}^L(u_L),$
2. $\theta_1 \le 0 \le \theta_2 \quad \Leftrightarrow \quad \lambda_w^* = \lambda_w^R(u_R), \quad \lambda_{nw}^* = \lambda_{nw}^L(u_L),$
3. $\theta_1 \le \theta_2 \le 0 \quad \Leftrightarrow \quad \lambda_w^* = \lambda_w^R(u_R), \quad \lambda_{nw}^* = \lambda_{nw}^R(u_R),$

Case 2: $g_w \ge g_{nw}$

We define the quantities

$$\theta_1 = v + (g_w - g_{nw})\,\lambda_{nw}^R(u_R), \quad \theta_2 = v + (g_{nw} - g_w)\,\lambda_w^L(u_L).$$

Now, $\theta_1 \ge \theta_2$ since $g_w \ge g_{nw}$. The explicit formulae are

1. $0 \le \theta_2 \le \theta_1 \quad \Leftrightarrow \quad \lambda_w^* = \lambda_w^L(u_L), \quad \lambda_{nw}^* = \lambda_{nw}^L(u_L),$
2. $\theta_2 \le 0 \le \theta_1 \quad \Leftrightarrow \quad \lambda_w^* = \lambda_w^L(u_L), \quad \lambda_{nw}^* = \lambda_{nw}^R(u_R),$
3. $\theta_2 \le \theta_1 \le 0 \quad \Leftrightarrow \quad \lambda_w^* = \lambda_w^R(u_R), \quad \lambda_{nw}^* = \lambda_{nw}^R(u_R),$

The definition above is exactly the same as for the fluxes away from $x = 0$, although with more consideration on the mobility functions.

We now turn our attention to consistency and monotonicity. As for the other schemes, consistency and monotonicity will only be investigated involving the

numerical fluxes G^{UM} and $\overline{F}^{UM}$. First we check consistency for G^{UM}, and keep in mind that the physical fluxes g and f are the flux functions defined in section 2.2.3.1, where we derived the two-phase flow model.

$$G^{UM}(\bar{u},\bar{u}) = \frac{\lambda_w^{L*}}{\lambda_w^{L*}+\lambda_{nw}^{L*}}\left[v + (g_w - g_{nw})\,\lambda_{nw}^{L*}\right], \tag{3.5.16}$$

where

$$\lambda_l^{L*} = \lambda_l^L(\bar{u}), \quad l = w, nw, \tag{3.5.17}$$

thus

$$G^{UM}(\bar{u},\bar{u}) = g(\bar{u}). \tag{3.5.18}$$

For the interface flux we get

$$\overline{F}^{UM}(\bar{u},\bar{u}) = \frac{\lambda_w^{*}}{\lambda_w^{*}+\lambda_{nw}^{*}}\left[v + (g_w - g_{nw})\,\lambda_{nw}^{*}\right]. \tag{3.5.19}$$

Here the mobility functions λ_l^* are determined from the analysis given above. From the explicit formulae we see that there exist cases where the mobility functions are given by λ^L for one phase and λ^R for the other (c.f. entry 2 for Case 1 and Case 2 in the analysis above). Thus, for some $\bar{u}$, $\overline{F}^{UM}$ fails to be consistent with g or f.
Proof of monotonicity for the scheme away from the interface $x = 0$, is the same as the proof given in e.g. [22, 5]. Thus, we again focus on proving monotonicity for the scheme at $x = 0$, where $j = \pm 1$ in (3.1.6), and limiting even further, we let $j = -1$ and $g_w \leq g_{nw}$, suggesting that the proof is similar for the other cases. $\mathbf{H}(\mathbf{u})$ for a fixed time at $j = -1$ is given by

$$H_{-1}(\mathbf{u}) = u_{-1} - \lambda\left[\overline{F}^{UM}(u_{-1},u_1) - G^{UM}(u_{-2},u_{-1})\right]. \tag{3.5.20}$$

To calculate the derivatives of the numerical fluxes with respect to u_L and u_R, we go through all the possible situations listed under Case 1 above. To simplify the notation we introduce some quantities:

$$\begin{aligned} \delta_1 &= v + (g_w - g_{nw})\,\lambda_{nw}^{*}, \\ \delta_2 &= v + (g_{nw} - g_w)\,\lambda_w^{*}. \end{aligned} \tag{3.5.21}$$

Since $g_w \leq g_{nw}$ and $v, \lambda_l^* \geq 0$, we have $\delta_1 \leq \delta_2$. Recall the quantities

$$\theta_1 = v + (g_w - g_{nw})\,\lambda_w^L(u_L), \quad \theta_2 = v + (g_{nw} - g_w)\,\lambda_w^R(u_R)$$

We now calculate the derivatives of $\overline{F}^{UM}$:

1. $0 \leq \theta_1 \leq \theta_2$

   For this case, the mobility functions are given as

$$\lambda_w^* = \lambda_w^L(u_L), \quad \lambda_{nw}^* = \lambda_{nw}^L(u_L).$$

The interface flux functions with the simplified notations is then

$$\begin{aligned}\delta_1 &= v + (g_w - g_{nw})\lambda_{nw}^L(u_L) = \theta_1,\\ \delta_2 &= v + (g_{nw} - g_w)\lambda_w^L(u_L),\end{aligned}$$

$$\overline{F}^{UM}(u_L, u_R) = \frac{\lambda_w^L(u_L)}{\lambda_w^L(u_L) + \lambda_{nw}^L(u_L)}\delta_1.$$

The derivative with respect to u_L

$$\overline{F}_{u_L}^{UM}(u_L, u_R) = \frac{\left(\left(\lambda_w^L\right)'(u_L)\,\delta_1\lambda_{nw}^L(u_L) - \lambda_w^L(u_L)\,\delta_2\left(\lambda_{nw}^L\right)'(u_L)\right)}{\left(\lambda_w^L(u_L) + \lambda_{nw}^L(u_L)\right)^2} \geq 0, \tag{3.5.22}$$

since λ_l are positive functions with respect to u, λ_w is non-decreasing and λ_{nw} is non-increasing.
Further we have

$$\overline{F}_{u_R}^{UM}(u_L, u_R) = 0, \tag{3.5.23}$$

since $\overline{F}^{UM}$ only depends on u_L.

2. $\theta_1 \leq 0 \leq \theta_2$

   Here, the mobility functions are

$$\lambda_w^* = \lambda_w^R(u_R), \quad \lambda_{nw}^* = \lambda_{nw}^L(u_L).$$

The interface flux function with simplified notation is

$$\begin{aligned}\delta_1 &= v + (g_w - g_{nw})\lambda_{nw}^L(u_L) = \theta_1,\\ \delta_2 &= v + (g_{nw} - g_w)\lambda_w^R(u_R) = \theta_2,\end{aligned}$$

$$\overline{F}^{UM}(u_L, u_R) = \frac{\lambda_w^R(u_R)}{\lambda_w^R(u_R) + \lambda_{nw}^L(u_L)}\delta_1.$$

Derivation with respect to u_L and u_R is given as

$$\overline{F}_{u_L}^{UM}(u_L, u_R) = -\frac{\lambda_w^R(u_R)\left(\lambda_{nw}^L\right)'(u_L)\,\delta_2}{\left(\lambda_w^R(u_R) + \lambda_{nw}^L(u_L)\right)^2} \geq 0, \tag{3.5.24}$$

$$\overline{F}_{u_R}^{UM}(u_L, u_R) = \frac{\left(\lambda_w^R\right)'(u_R)\,\lambda_{nw}^L(u_L)\,\delta_1}{\left(\lambda_w^R(u_R) + \lambda_{nw}^L(u_L)\right)^2} \leq 0. \tag{3.5.25}$$

Again calculated using the properties of the mobility functions λ_l.

3. $\theta_1 \leq \theta_2 \leq 0$

   The mobility functions for this case is given as

$$\lambda_w^* = \lambda_w^R(u_R), \quad \lambda_{nw}^* = \lambda_{nw}^R(u_R).$$

   With these mobility functions, the interface flux function is given as

$$\begin{aligned} \delta_1 &= v + (g_w - g_{nw})\lambda_{nw}^R(u_R), \\ \delta_2 &= v + (g_{nw} - g_w)\lambda_w^R(u_R) = \theta_2, \end{aligned}$$

$$\overline{F}^{UM}(u_L, u_R) = \frac{\lambda_w^R(u_R)}{\lambda_w^R(u_R) + \lambda_{nw}^R(u_R)}\delta_1.$$

   We derived with respect to u_L and u_R:

$$\overline{F}_{u_L}^{UM}(u_L, u_R) = 0, \tag{3.5.26}$$

$$\overline{F}_{u_R}^{UM}(u_L, u_R) = \frac{\left(\left(\lambda_w^R\right)'(u_R)\,\delta_1\lambda_{nw}^R(u_R) - \lambda_w^R(u_R)\,\delta_2\left(\lambda_{nw}^R\right)'(u_R)\right)}{\left(\lambda_w^R(u_R) + \lambda_{nw}^R(u_R)\right)^2} \leq 0. \tag{3.5.27}$$

   The calculations are equal to the ones done for the first situation, but now with $\overline{F}^{UM}$ only depending on u_R.

As noted before, the formula for $\overline{F}^{UM}$ are similar to the ones for G^{UM} and F^{UM}, thus we get similar results for the derivatives of G^{UM}, that is

$$G_{u_L}^{UM}(u_L, u_R) \geq 0, \qquad G_{u_R}^{UM}(u_L, u_R) \leq 0. \tag{3.5.28}$$

The derivatives of $H_{-1}(\mathbf{u})$ with respect to u_{-2}, u_{-1} and u_1 are for all the situations in Case 1

$$\frac{\partial H_{-1}}{\partial u_{-2}} = \lambda G_{u_L}^{UM}(u_{-2}, u_{-1}) \geq 0, \tag{3.5.29}$$

$$\frac{\partial H_{-1}}{\partial u_1} = -\lambda \overline{F}_{u_R}^{UM}(u_{-1}, u_1) \geq 0, \tag{3.5.30}$$

$$\frac{\partial H_{-1}}{\partial u_{-1}} = 1 - \lambda\left[\overline{F}_{u_L}^{UM}(u_{-1}, u_1) - G_{u_R}^{UM}(u_{-2}, u_{-1})\right] \geq 0. \tag{3.5.31}$$

A special CFL condition is needed for the last inequality to be true, as pointed out in [22] and [5, 18]. The CFL condition with $\lambda = \Delta t/\Delta x$ is:

$$\lambda M \leq 1, \tag{3.5.32}$$

where

$$M = \max\left\{ \max_{j \text{ for } x \neq 0} \left\{ \frac{\partial \mathcal{F}^n_{j+1/2}}{\partial u_L}(u_j, u_{j+1}) - \frac{\partial \mathcal{F}^n_{j-1/2}}{\partial u_R}(u_{j-1}, u_j) \right\} \right.$$
$$\left. \frac{\partial F^n_{3/2}}{\partial u_L}(u_1, u_2) - \frac{\partial \overline{F}}{\partial u_R}(u_{-1}, u_1), \frac{\partial \overline{F}}{\partial u_L}(u_{-1}, u_1) - \frac{\partial G^n_{-3/2}}{\partial u_R}(u_{-2}, u_{-1}) \right\}. \tag{3.5.33}$$

Hence the scheme is monotone under the CFL-condition above.

Since the interface flux is inconsistent, convergence analysis must be done in the same manner as for the Godunov scheme. This is done in [18].

Chapter 4

Numerical Experiments

In this chapter we present numerical results of different test scenarios, to investigate the performance of the Upstream Mobility scheme. The test scenarios involves two phase flow in a heterogeneous porous medium, since it is here the Upstream Mobility scheme is widely used. We try to explain errors and deviations from a mathematical as well as physical point of view. By doing this the results becomes more applicable and comparable to real-life problems. A secondary objective is testing the Local Lax-Friedrichs scheme to see which of the entropy conditions it converges to, and how it performs compared with the other numerical methods.

4.1 Model Specifications

Our main focus in this chapter is fluid flow in porous medium (see theory in section 2.2.3.1). We denote the wetting phase as water (w) and the non-wetting phase as oil (o), as it is the most common situation. In this situation $\rho_w > \rho_o$, that is, water is the heavier phase. The conserved material is water saturation, given by S_w. Due to wetting preference of the porous media, the saturation of water or oil can only be reduced to a minimal (or irreducible) saturation, denoted S_{wi} and S_{or} for water and oil respectively. Thus we can normalize the water saturation according to the following equation

$$u = \frac{S_w - S_{wi}}{1 - S_{wi} - S_{or}}. \tag{4.1.1}$$

The domain of u is therefore $[0, 1]$ where 0 indicates $S_w = S_{wi}$ and 1 when $S_w = 1 - S_{or}$. The flux functions are given by the equation

$$h(u) = \frac{\lambda_w}{\lambda_w + \lambda_o} \left[v + (g_w - g_o) \lambda_o \right], \tag{4.1.2}$$

where $h(u)$ can be either $g(u)$ or $f(u)$. We let $\mu_w = \mu_o = 1$ since we are only interested in the impact of the discontinuity represented by change in permeability. Thus the effective mobility functions becomes $\lambda_l = Kk_l(u)$ for each phase l. We also let $v = 1$ in the following, unless nothing else is specified. The relative permeability functions, $k_l(u)$, are approximated according to the Corey relation [6], that is, they are assumed to follow a power law correlation with respect to u:

$$k_w(u) = k_w^0 u^p, \qquad k_o(u) = k_o^0 (1-u)^n, \tag{4.1.3}$$

where k_l^0 are endpoint values of the relative permeabilities for each phase l in the sense that k_w^0 is the value when $u = 1$ and k_o^0 is the value when $u = 0$. p and n can be obtained from measured data, or approximated from flow simulations, but is usually set to $p = n = 2$. The relative permeabilities and effective mobilities must satisfy the following property:

$$\begin{aligned} k_w &\text{ and } \lambda_w \text{ are increasing functions of } u, \\ k_o &\text{ and } \lambda_o \text{ are decreasing functions of } u, \end{aligned}$$

The gravity components g_l can be chosen such that the impact of the gravity force, given by $(g_w - g_o)$, is negative, positive or zero, corresponding to downdip, updip or horizontal flow. The impact on a flux function $h(u)$ is given in figure 4.1.1. In the following test scenarios, the gravity components are chosen such that gravity term in (4.1.2) is $+\lambda_o$, $-\lambda_o$ or 0. Thus, the gravity term is the most weighted term in (4.1.2), which is done in anticipation of more distinctive numerical results. Figure 4.1.2 shows the gravitational impact on the flux function.

We solve the conservation laws

$$\begin{aligned} u_t + g(u)_x &= 0, \quad x < x_h, \\ u_t + f(u)_x &= 0, \quad x > x_h, \end{aligned} \tag{4.1.4}$$

with initial condition

$$u_0(x) = \begin{cases} u_L = 1, & x < 0, \\ u_R = 0, & x > 0. \end{cases} \tag{4.1.5}$$

As in the example of heterogeneous two phase flow, we let the spatial discontinuity in the flux function be at $x_h > 0$ and denote $t = t_h$ as the time when the solution wave reaches the interface. The initial condition is still discontinuous at $x = 0$. The Riemann problem above has many application for two-phase flow in a porous medium. Depending on the boundary conditions, the Riemann problem can simulate water injection at $x = 0$ and production at some $x = x_{end}$, or two phase flow in a core plug where the set up, parameters and inflow can be controlled. It is therefore natural to simulate the general Riemann

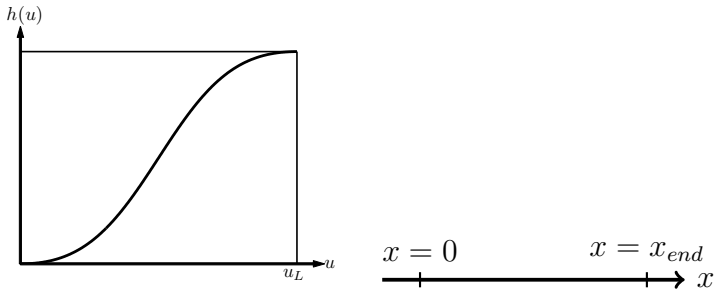

(a) Horizontal flow

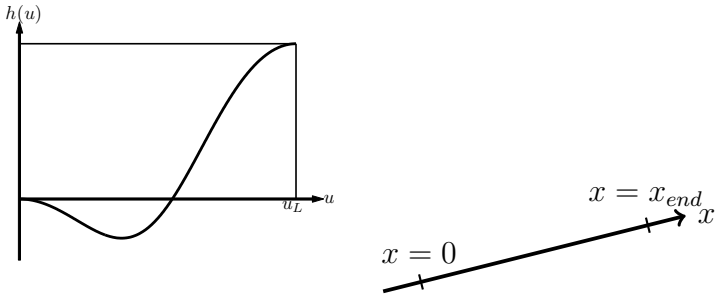

(b) Updip flow

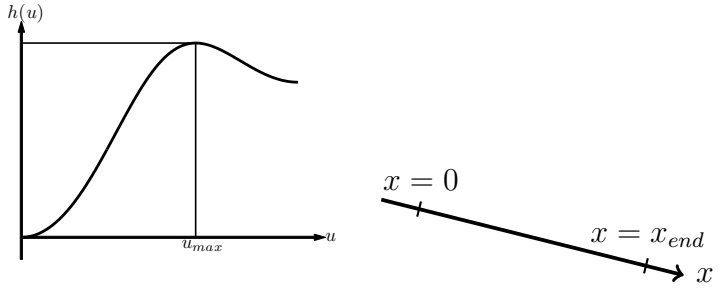

(c) Downdip flow

Figure 4.1.1: Illustration of the effect of gravity on a flux function $h(u)$

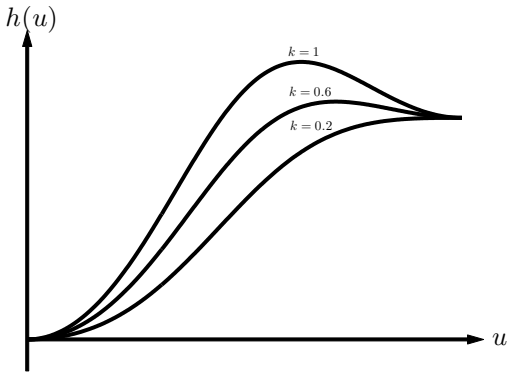

Figure 4.1.2: The impact of gravitation on the flux function (4.1.2), where $(g_w - g_o) = k$

problem in the numerical experiments below. The transition from one porous medium to another is at x_h which is located at $x_{end}/2$. We discretize the grid according to section 3.1.3, where negative j indicates cells to the left of x_h and positive j indicates the cells to the right of x_h, making $x_h = x_{-1/2} = x_{1/2}$. The area of interest for our numerical experiments is $x > 0$, since it is here x_h is located, and we therefore limit our view of the solution to $x \in (0, x_{end})$. Thus, we need a boundary condition at $x = 0$:

$$g\left(u\left(0,t\right)\right) = g\left(u_{max}\right), \quad \text{for } t > 0, \tag{4.1.6}$$

where u_{max} is maximum point of $g\left(u\right)$ (i.e. $g'\left(u_{max}\right) = 0$). From figure 4.1.1, we see that $u_{max} = u_L$ for horizontal and updip flow, but for downdip flow $u_{max} = \theta_g$. For a Riemann problem, this boundary condition is nothing more than a fact following from the solution. When solving the problem by a numerical method, it ensures us mass conservation for $x > 0$. In practice, the boundary condition is implemented as follows

$$u_j^{n+1} = u_j^n - \lambda\left(G\left(u_j, u_{j+1}\right) - g\left(u_{max}, t^n\right)\right) \tag{4.1.7}$$

where j is such that Ω_j is the *first* cell in the grid.
At $x = x_{end}$ we also need a boundary condition, since our porous medium is finite. The boundary condition at $x = x_{end}$ is implemented in the scheme as follows

$$u_j^{n+1} = u_j^n - \lambda\left(f\left(u_j^n\right) - F\left(u_{j-1}, u_j\right)\right) \tag{4.1.8}$$

where j now is such that Ω_j is the *last* cell in the grid. In practice, the boundary condition states that we "produce" the saturation given at x_j with the flux $f\left(u_j^n\right)$. Both of the boundary conditions is only valid if we have flow from left to right. The boundary conditions are illustrated in figure 4.1.3. With $u_R = 0$ (i.e. $S_w = S_{wi}$), we assume that the porous medium is initially saturated with oil.

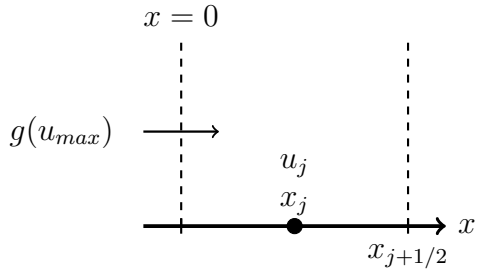

(a) Injection at $x = 0$ indicated by $g\left(u_{max}\right)$. u_j is the first node after $x = 0$

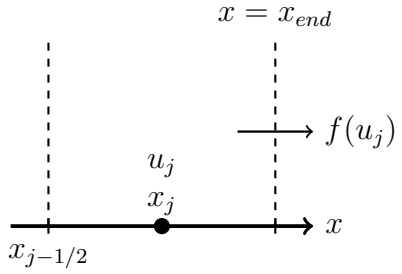

(b) Production at $x = x_{end}$ indicated by $f\left(u_j\right)$, where u_j is the last node before $x = x_{end}$.

Figure 4.1.3: Illustration of the boundary conditions (4.1.7) and (4.1.8)

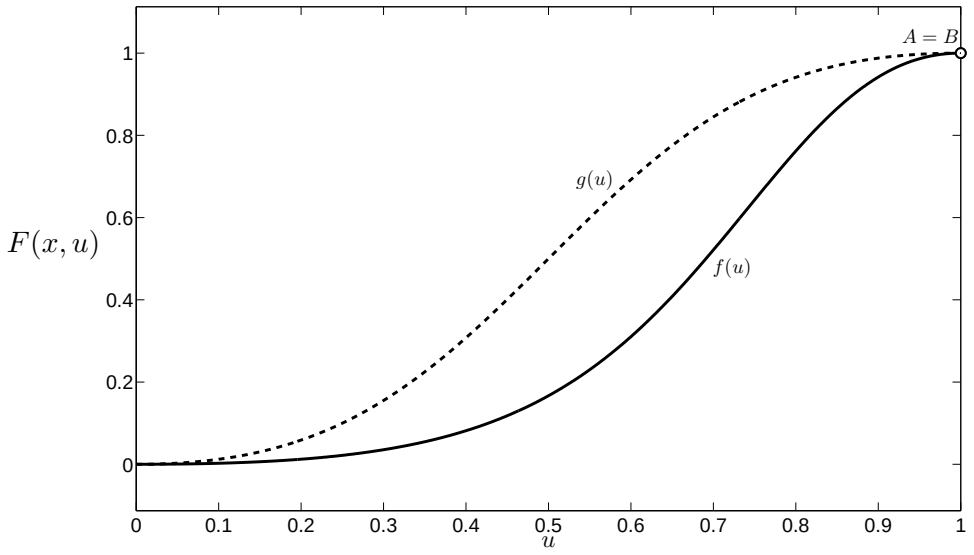

Figure 4.1.4: Flux functions for Experiment A1 with $A = B = 1$ indicated

When nothing else is specified the grid step is $\Delta x = 0.01$. The time step is chosen according to the CFL-condition of the schemes. Since we do not emphasize on computational effectiveness in the experiments, the time steps have been chosen below the least required value from the CFL-condition for every method. We also omit porosity, as it is only a scaling factor for the flow. The numerical methods are denoted as follows: Godunov (G) and Engquist-Osher (EO) if they follow the optimal entropy condition and (G-MJ) and (EO-MJ) if they follow the minimal jump condition. Further we denote Local Lax-Friedrichs (LLxF) and Upstream Mobility (UM).

4.2 Test scenario A: Horizontal Flow

In a pure horizontal porous medium, we do not have any gravity component which can work with or against the flow in the porous medium. Thus the only component driving the water through the reservoir is the total Darcy velocity, v. The flux functions for this flow situation is given by

$$h(u) = \frac{\lambda_w}{\lambda_w + \lambda_o} v, \tag{4.2.1}$$

where $h(u)$ is either $g(u)$ or $f(u)$. The (A, B)-connection can only be $A = B = 1$ if it is to satisfy the requirements in the theory section. Thus the two entropy conditions coincide for this reservoir type. We look at one experiment of this flow type:

Experiment A1
The mobility values to left of x_h is

$$\lambda_w^L = u^2, \qquad \lambda_o^L = (1-u)^2,$$

and to the right of x_h

$$\lambda_w^R = 2u^2, \qquad \lambda_o^R = 10\,(1-u)^2,$$

The flux functions are thus given as

$$g(u) = \frac{u^2}{u^2 + (1-u)^2}, \qquad f(u) = \frac{2u^2}{2u^2 + 10\,(1-u)^2}, \tag{4.2.2}$$

and is shown in figure 4.1.4. Physically speaking, we experience a change in the relative permeability across the interface, x_h. The analytical solution for this experiment is the same as the one given in the example in section 2.3. In figure 4.2.1 we show the numerical results both before and after the waves have passed the heterogeneity at x_h. We observe that the G, EO and UM schemes do not differ at all, indicating that the UM scheme performs well in horizontal flow. We could have anticipated this beforehand, as horizontal flow only involve advection, meaning the flow of water and oil is from $x = 0$ to $x = x_{end}$ only, thus the upstream weighting choose the left saturation value for λ_l at each cell edge. The upwind nature of G and EO explains why these schemes perform well when only advection is considered. However the LLxF scheme experience much numerical dispersion, and in figure 4.2.1b we see that the scheme misses the interface discontinuity.

4.3 Test scenario B: Updip Flow

Updip flow is shown in figure 4.1.1b. Here the gravity component is negative, and work against the flow of water leading to a more efficient sweep, that is, a more piston-like displacement of oil. Mathematically, we can justify the physical observation by looking at the flux function in figure 4.1.1b. The flux functions is of convex type ($CV\,(I)$), and with the initial condition $u_R < u_L$ we create a shock solution from u_R to some u_s which is closer to u_L than for horizontal and downdip flow. For this test scenario the flux functions $g(u)$ and $f(u)$ is generally given as

$$h(u) = \frac{\lambda_w}{\lambda_w + \lambda_o}\left[1 - \lambda_o\right], \tag{4.3.1}$$

Here flux crossing is possible, thus the (A, B)-connections depends on which interface entropy condition we choose. When the flux functions intersect in

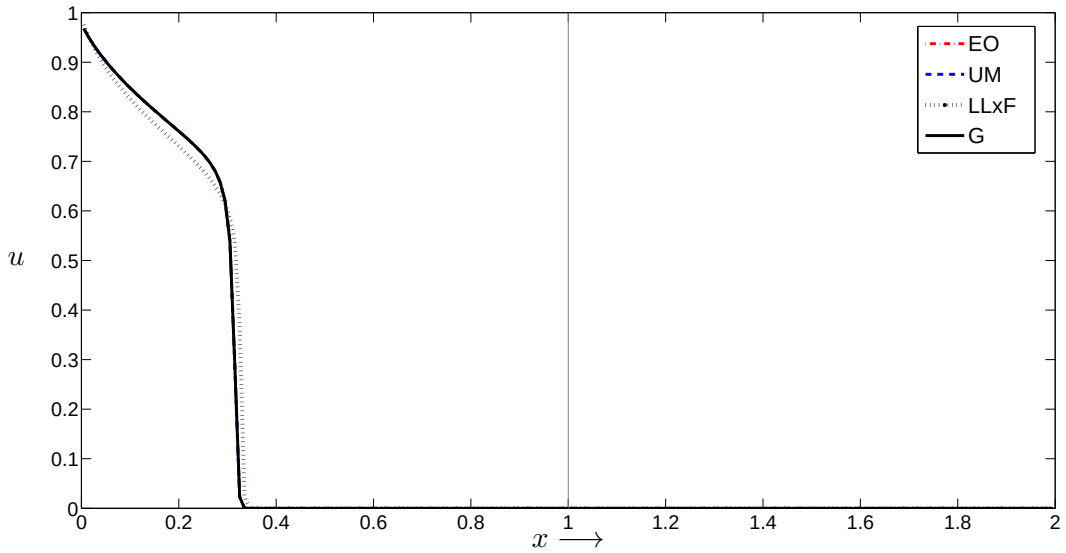

(a) $t = 0.25$

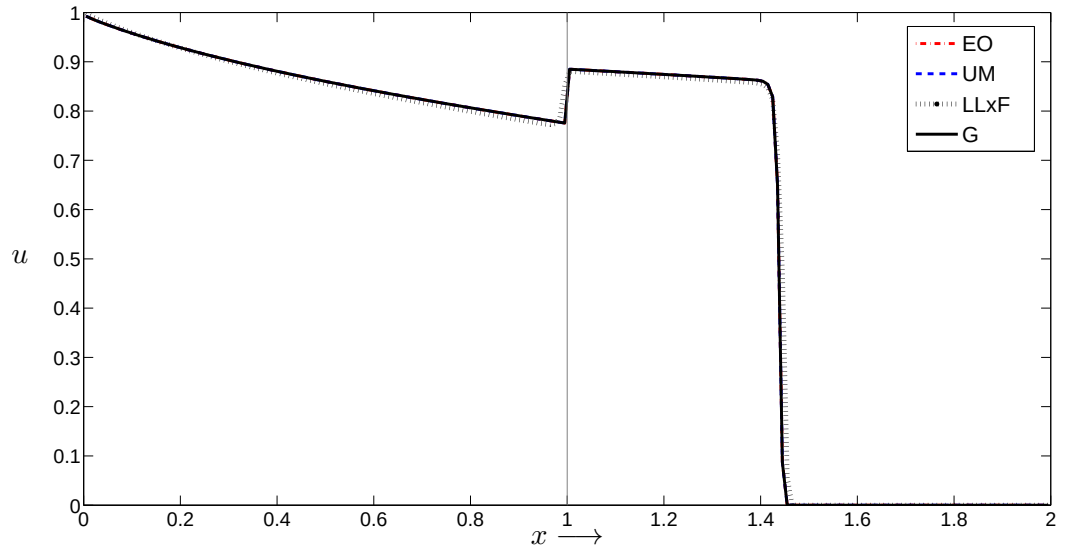

(b) $t = 1.25$

Figure 4.2.1: Plots of the solution to Experiment A1 at time $t = 0.25$ and $t = 1.25$

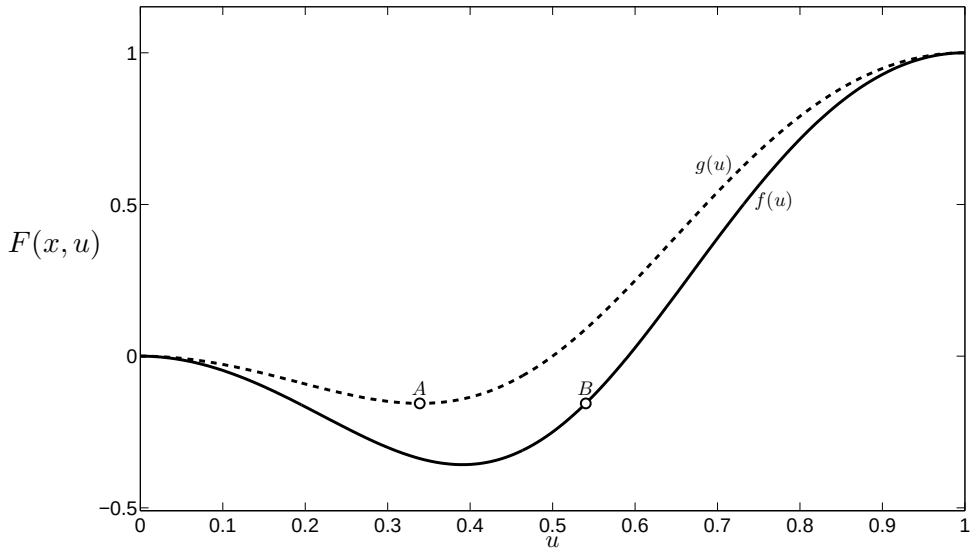

Figure 4.3.1: Flux functions for Experiment B1 with $(A, B) = \left(\theta_g, \overline{\theta}_g\right)$ indicated

a undercompressive manner, we indicate the optimal entropy connection with (A_o, B_o) and the minimal jump connection with (A_m, B_m). If the entropy conditions coincide, we denote the connection with (A, B). We look at two experiments for this flow type: one with changing absolute permeability and one with changing relative permeability.

Experiment B1

The mobility functions to the left of x_h is given as

$$\lambda_w^L = 4u^2, \qquad \lambda_o^L = 4\left(1-u\right)^2,$$

and to the right of x_h, the mobility functions are

$$\lambda_w^R = 6u^2, \qquad \lambda_o^R = 6\left(1-u\right)^2,$$

The flux functions are given as

$$\begin{aligned} g\left(u\right) &= \frac{u^2}{u^2+\left(1-u\right)^2}\left[1-4\left(1-u\right)^2\right], \\ f\left(u\right) &= \frac{u^2}{u^2+\left(1-u\right)^2}\left[1-6\left(1-u\right)^2\right], \end{aligned} \tag{4.3.2}$$

and is drawn in figure 4.3.1 . The mobility functions experience a change in absolute permeability across the interface. The analytical solution for this

problem is similar to the procedure for horizontal flow, described in experiment A1 (which was the same as the example in section 2.3). In figure 4.3.2 we show the numerical solutions for experiment B1. Again the UM scheme is doing well, and there is no notable difference between this scheme and G. In the previous chapter it was noted that EO differs from G when $h'(u_L) > 0 > h'(u_R)$ which is exactly the case we have for both $g(u)$ and $f(u)$ with our initial condition. If we zoom in on the front for $t = 1.25$, we can see the numerical dispersion of EO in this experiment; c.f. figure 4.3.3. LLxF is performing better than in experiment A1, but in figure 4.3.3 we see that it still experience numerical dispersion. It also has trouble at the interface, x_h, but it is hard to see as the jump there is quite small.

Experiment B2
To the left of x_h we have the mobility functions

$$\lambda_w^L = 2u^2, \qquad \lambda_o^L = 20\,(1-u)^2\,,$$

and to the right of x_h we have

$$\lambda_w^R = 20u^2, \qquad \lambda_o^R = 4\,(1-u)^2\,,$$

giving the flux functions

$$\begin{aligned} g(u) &= \frac{u^2}{u^2 + 10\,(1-u)^2}\left[1 - 20\,(1-u)^2\right], \\ f(u) &= \frac{u^2}{u^2 + \frac{1}{5}\,(1-u)^2}\left[1 - 4\,(1-u)^2\right], \end{aligned} \tag{4.3.3}$$

illustrated in figure 4.3.4. In this experiment, the flux functions crosses in an undercompressive manner, thus we have the two interface entropy conditions represented. In the porous medium this corresponds to change in relative permeability. Figure 4.3.5 shows the numerical solutions of this experiment. With the initial conditions $u_L = 1$ and $u_R = 0$, the solution is a jump between $u^-(t)$ and $u^+(t)$ located close to u_L. Hence we get the same solution for both of the interface entropy conditions. The numerical methods performs similarly as in Experiment B1, and the comments given there is also valid for this experiment.

With the two first test scenarios, we have dealt with displacement of oil which is most preferable, i.e. the situations where we have piston-like displacement. The flow has been purely from left to right for both phases, and the UM scheme has performed as good as G. From the definition of UM, this is not unexpected. We now turn our attention to the test scenarios where more challenging fluid flow is studied.

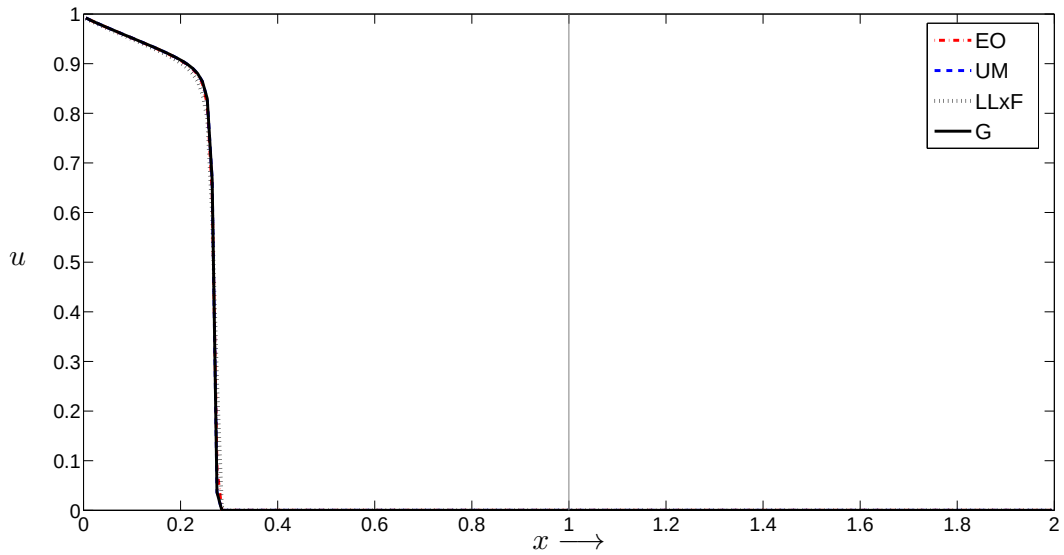

(a) $t = 0.25$

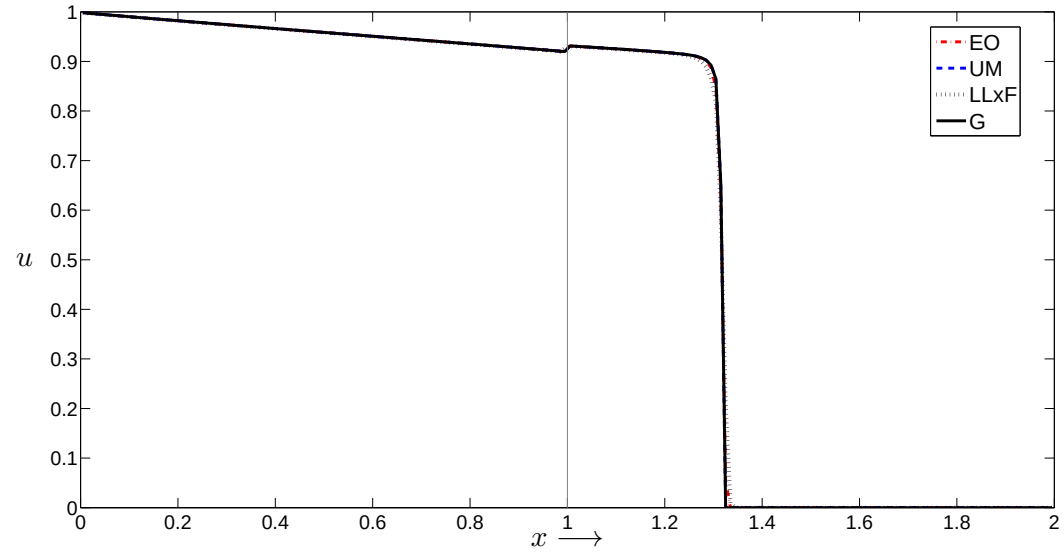

(b) $t = 1.25$

Figure 4.3.2: Numerical solutions of Experiment B1 at time $t = 0.25$ and $t = 1.25$

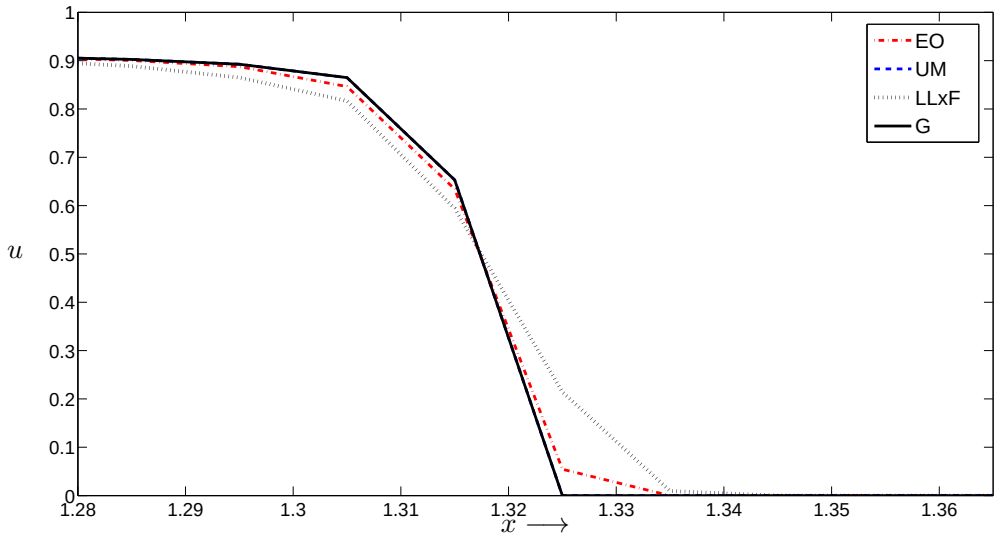

Figure 4.3.3: The solution front of Experiment B1 at $t = 1.25$. EO and LLxF experience numerical diffusion

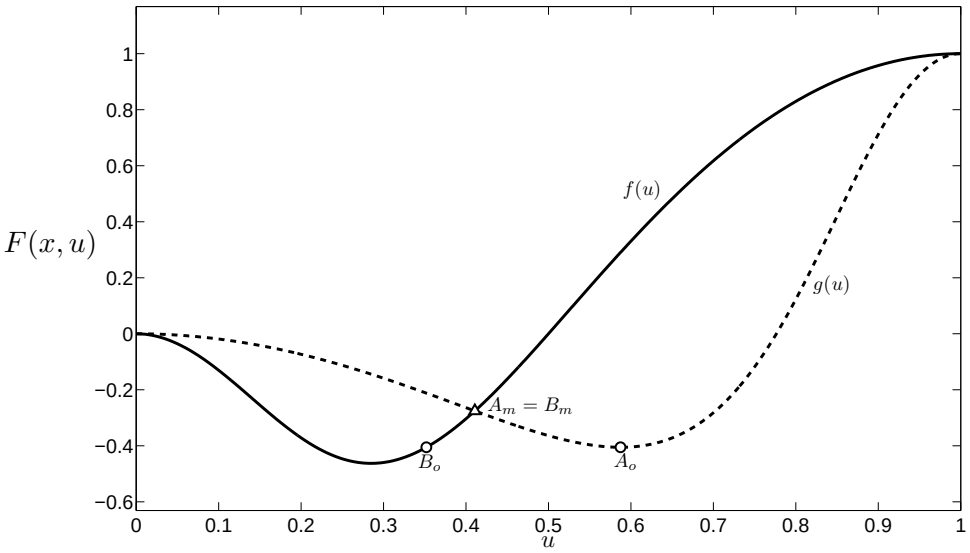

Figure 4.3.4: Flux functions for Experiment B2 with $(A_o, B_o) = \left(\theta_g, \overline{\theta}_g\right)(\circ)$ and $(A_m, B_m) = (u_\chi, u_\chi)$ $(\triangle)$ indicated

4.4 Test scenario C: Downdip Flow

Figure 4.1.1c illustrates what we mean by downdip flow. Here the gravity forces drives the injected water downwards, and the oil, which is lighter, moves upwards, giving countercurrent flow. In mathematical terms, we now deal with flux functions of concave type, i.e. $f, g \in CC\,(I)$. The solution near $x = 0$

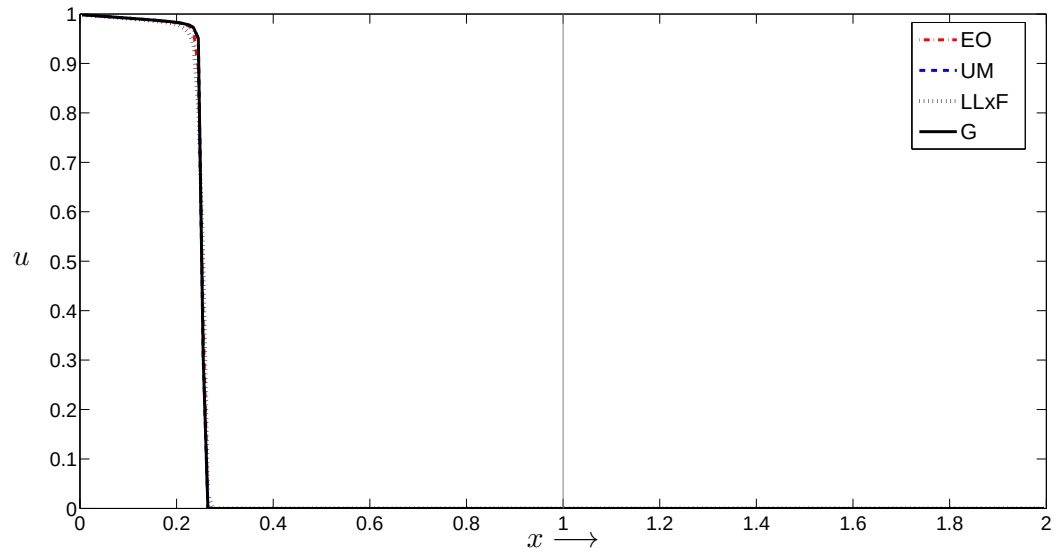

(a) $t = 0.25$

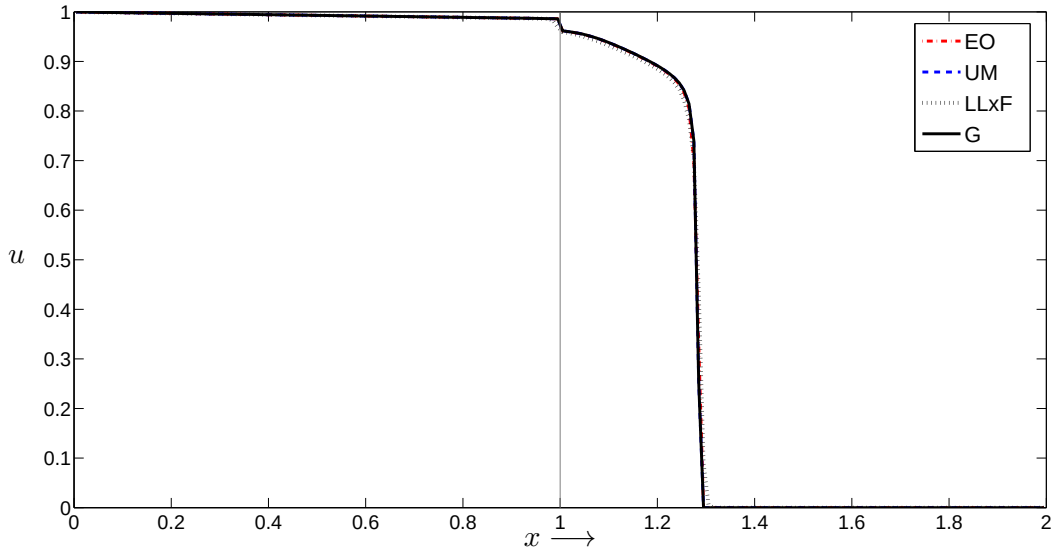

(b) $t = 1.25$

Figure 4.3.5: The numerical solutions of Experiment B2 at time $t = 0.25$ and $t = 1.25$

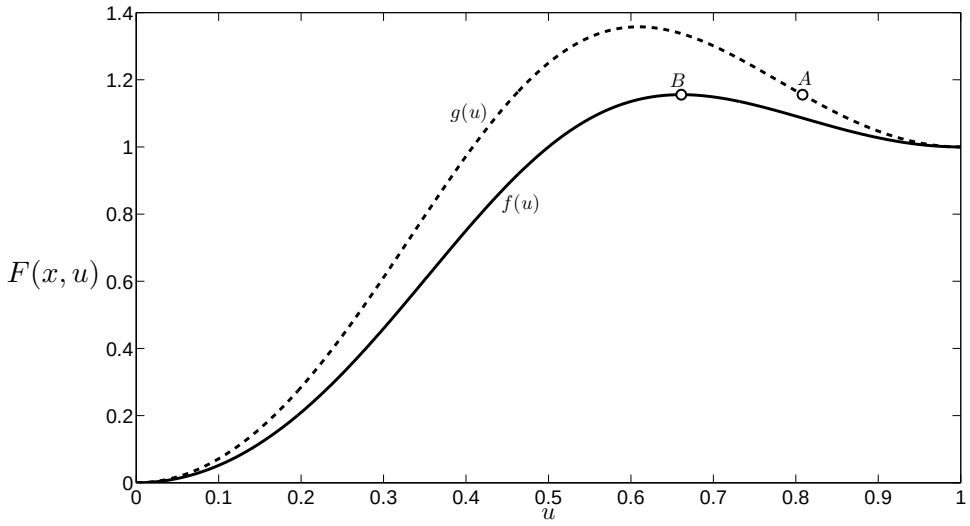

Figure 4.4.1: Flux functions for Experiment C1 with $(A, B) = \left(\overline{\theta}_f, \theta_f\right)$ indicated

with the above initial condition, consist of 3 waves if we include the region $x < 0$. We have two shock waves, one going left in the region $x < 0$ and one going right in $x > 0$, connected by a rarefaction wave. As noted in the model specifications, we are only interested in the solution for $x > 0$. The flux functions for this flow type is generally given as

$$h\left(u\right) = \frac{\lambda_w}{\lambda_w + \lambda_o}\left[1 + \lambda_o\right]. \tag{4.4.1}$$

As for updip flow flux function crossing can occur, leaving the possibility for the two interface entropy conditions to differ. If they do, we denote the optimal entropy condition as (A_o, B_o) and the minimal jump condition as (A_m, B_m). If not, we use the normal (A, B) notation. We anticipate some challenges for UM in this test scenario, therefore test a wide range of flux functions corresponding to both transitions in absolute and relative permeability across the heterogeneity.

Experiment C1
The mobility functions for $x < x_h$ is

$$\lambda_w^L = 6u^2, \qquad \lambda_o^L = 6\left(1-u\right)^2,$$

and for $x > x_h$ we have

$$\lambda_w^R = 4u^2, \qquad \lambda_o^R = 4\left(1-u\right)^2,$$

giving the flux functions

$$\begin{aligned} g(u) &= \frac{u^2}{u^2 + (1-u)^2}\left[1 + 6(1-u)^2\right], \\ f(u) &= \frac{u^2}{u^2 + (1-u)^2}\left[1 + 4(1-u)^2\right], \end{aligned} \tag{4.4.2}$$

which is illustrated in figure 4.4.1. The transition across x_h is a change in absolute permeability. The flux functions do not intersect for $u \in [0,1]$, hence the interface entropy conditions coincide. The solution for $t < t_h$ is a normal rarefaction-shock wave. When $t \geq t_h$, the jump is determined by the values $(u^-(t), u^+(t)) \neq (A, B)$. After some time, $g(u^-(t)) > g(A)$, and the jump between $g(u)$ and $f(u)$ must be at the values (A, B). Hence we get a shock wave moving leftwards, away from x_h, from $(g')^{-1}(x/t)$ to A. Figure 4.4.2 shows the solutions calculated with the different numerical schemes. All the schemes performs well in calculating the solution of the "homogeneous" case (i.e. the solution for $t < t_h$). Figure 4.4.2b shows the solution when $t > t_h$ and $g(u^-(t)) < g(A)$. Again all the schemes performs preferably. As we see in figure 4.4.2c, when the left-going shock wave starts propagating, we get some differences for each of the schemes. If we take a closer look at the interface, c.f. figure 4.4.3, we see that UM and LLxF misses the interface discontinuity, and also is not following the left-going shock as well as EO and G. At the interface the left trace of UM, u_{-1}, is almost equal to the one produce by G, which again is equal to $A \approx 0.81$, i.e. the correct value. The right trace, u_1, is, however, not equal to the desired value B, but is instead a higher u-value, approximately 0.76, and the solution decreases in value for $x > x_h$ until it coincides with the solution of EO and G.
To see if UM misses the interface due to numerical dispersion, we refine the grid size to $\Delta x = 0.005$ and $\Delta x = 0.001$ in figure 4.4.4. We see that refining the grid by a factor of 2 and 10 improves the approximation made by UM, and indicates to us that if we refine even more, UM will converge to the same jump solution as G and EO. We note that the left and right traces of UM is still $u_{-1} \approx A$ and $u_1 \approx 0.76$ even with mesh size of $\Delta x = 0.001$, and that the solution is a curved line after x_h with the fine mesh. It does not necessarily mean anything other than at some lower Δx the scheme will eventually approximate a sharp interface solution, but is worth noting. LLxF is also doing better at the interface when we refine the grid, even better than UM.
Qualitatively speaking, UM follows the desired entropy solution, and it seems that it converges to the physically correct solution.

In the next experiment we look at change in relative permeability. We keep $f(u)$ from the last experiment and change $g(u)$.

Experiment C2
The left mobility functions are

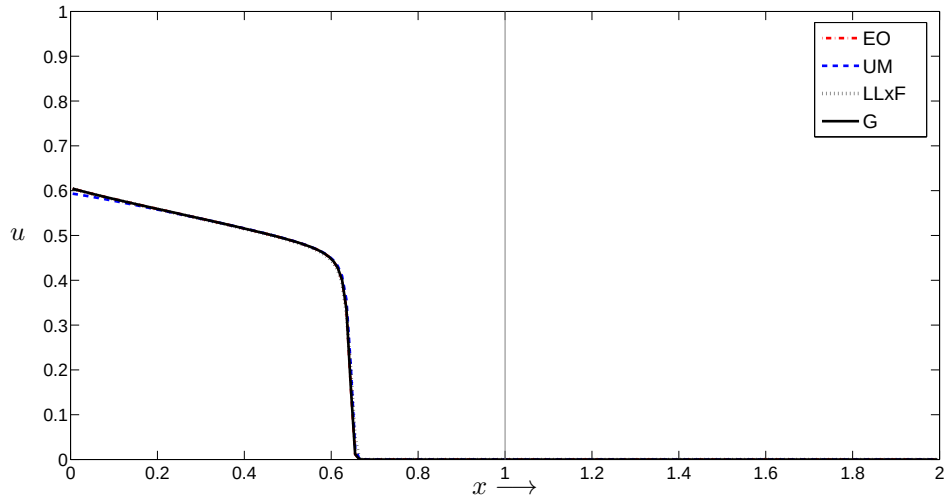

(a) $t = 0.25$

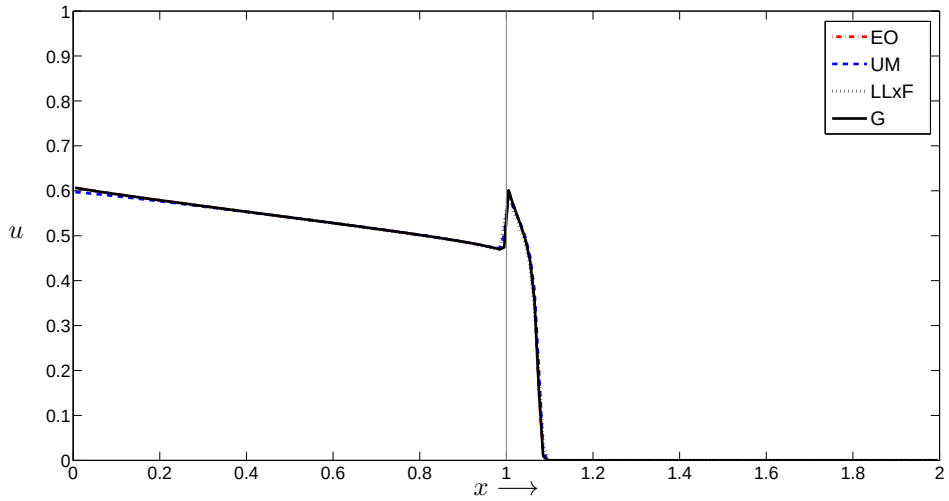

(b) $t = 0.425$

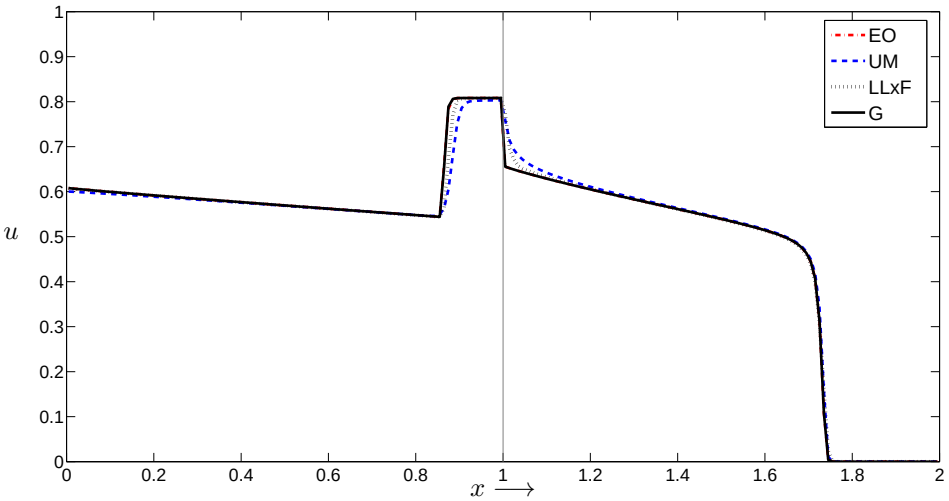

(c) $t = 0.75$

Figure 4.4.2: The numerical solutions of Experiment C1 at $t = 0.25$, $t = 0.425$ and $t = 0.75$

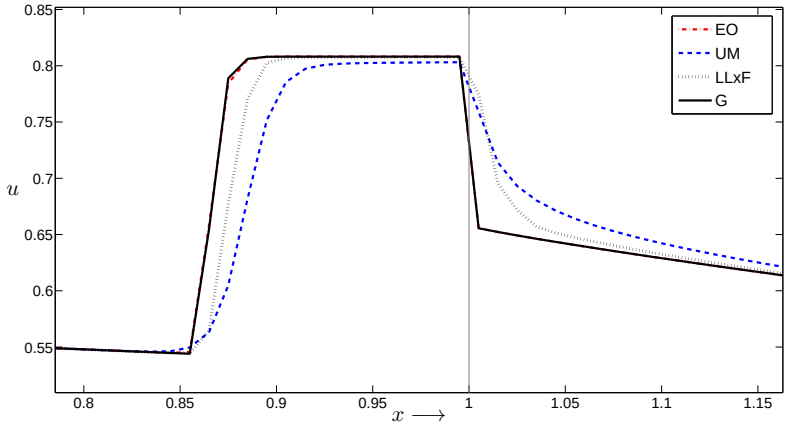

Figure 4.4.3: The solution of Experiment C1 at the interface $x = x_h$ at $t = 0.75$.

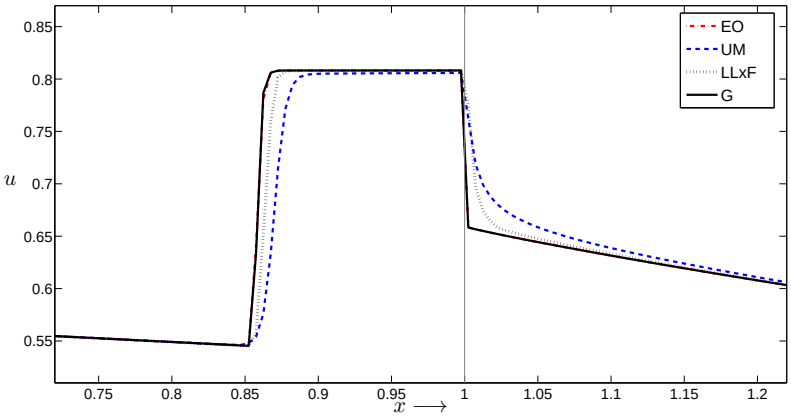

(a) $\Delta x = 0.005$

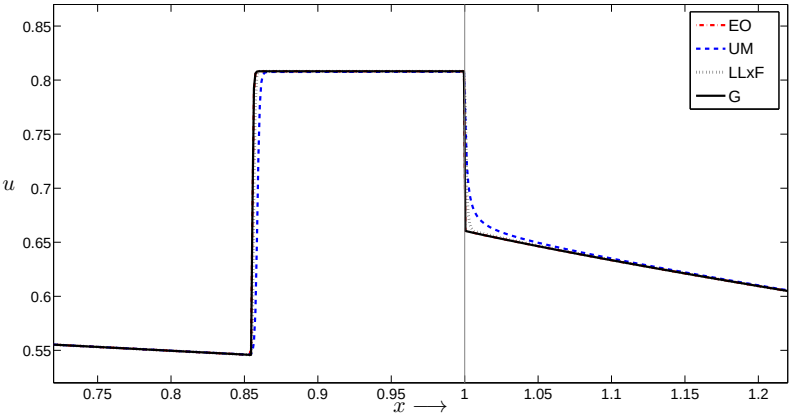

(b) $\Delta x = 0.001$

Figure 4.4.4: The numerical solutions of Experiment C1 at x_h for $t = 0.75$ with $\Delta x = 0.005$ and $\Delta x = 0.001$

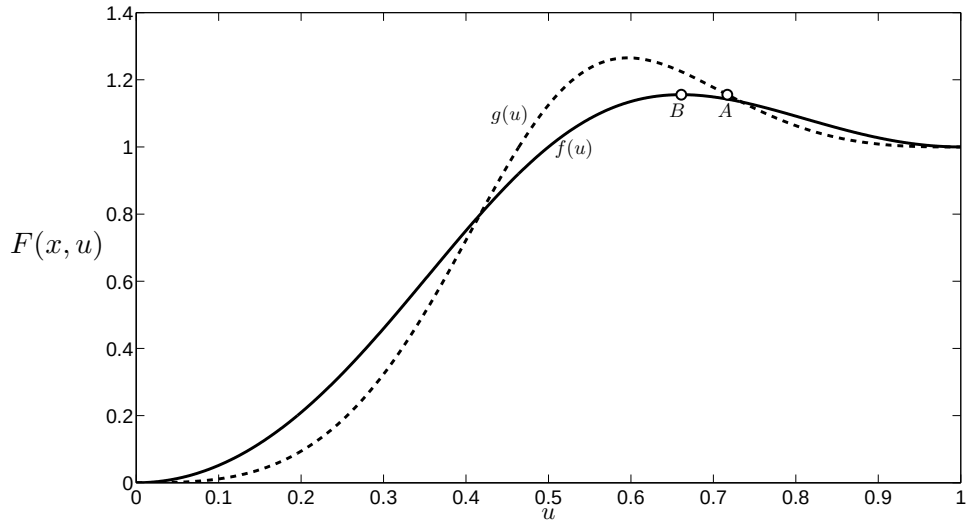

Figure 4.4.5: Flux functions for Experiment C2 with $(A, B) = \left(\overline{\theta}_f, \theta_f\right)$ indicated

$$\lambda_w^L = 10u^3, \qquad \lambda_o^L = 10\left(1-u\right)^3,$$

and the right mobility functions are

$$\lambda_w^R = 4u^2, \qquad \lambda_o^R = 4\left(1-u\right)^2,$$

giving the flux functions

$$\begin{aligned} g\left(u\right) &= \frac{u^3}{u^3 + \left(1-u\right)^3}\left[1 + 10\left(1-u\right)^3\right], \\ f\left(u\right) &= \frac{u^2}{u^2 + \left(1-u\right)^2}\left[1 + 4\left(1-u\right)^2\right], \end{aligned} \tag{4.4.3}$$

which is shown in figure 4.4.5 . The flux functions cross, but since $\theta_g \leq A \leq 1$ and $0 \leq B \leq \theta_f$ must be satisfied, both of the interface entropy conditions still coincide. The analytical solution is therefore similar to the one in Experiment C2. As seen in figure 4.4.6 the numerical solution for G, EO and LLxF is similar to the previous experiment. UM, however, misses the interface, giving a jump from a lower to a higher u-value,that is, from a left trace almost equal A to the right trace $u_1 \approx 0.75 > B$.
To see if the "spike" in the solution of UM still is present when refining the grid, we have illustrated the numerical solutions with grid size $\Delta x = 0.005$ and $\Delta x = 0.001$ at $t = 1$ in figure 4.4.7a and 4.4.7b, respectively. We clearly see that the right trace is of constant height of $u_1 \approx 0.75$ even with $\Delta x = 0.001$. This suggest that the "spike" will be present when $\Delta x \to 0$.

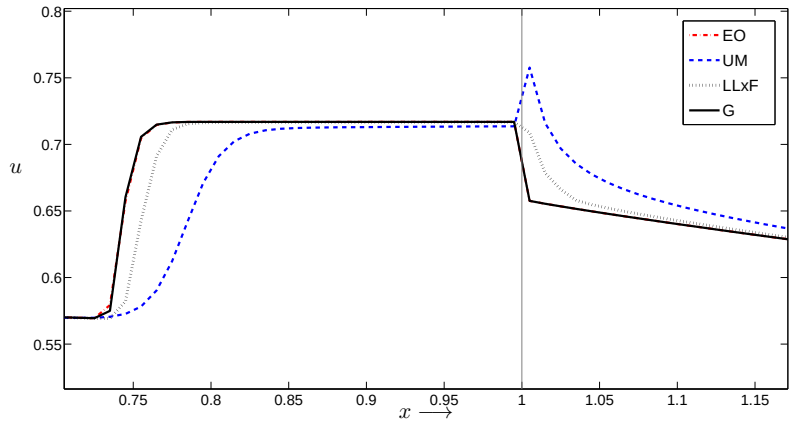

Figure 4.4.6: The numerical solutions of Experiment C2 at x_h for $t = 1$

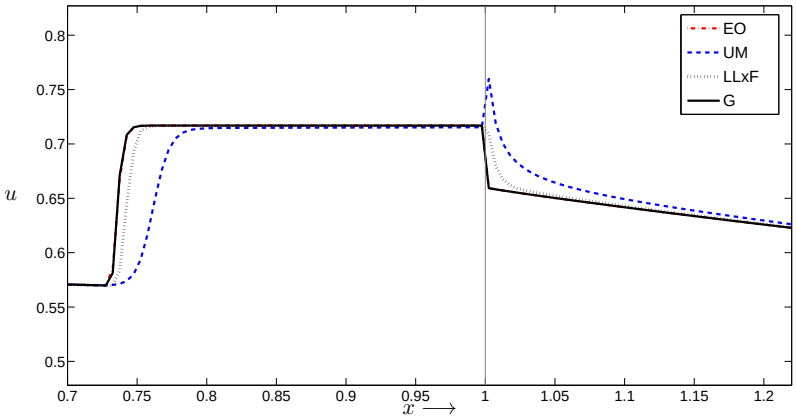

(a) $\Delta x = 0.005$

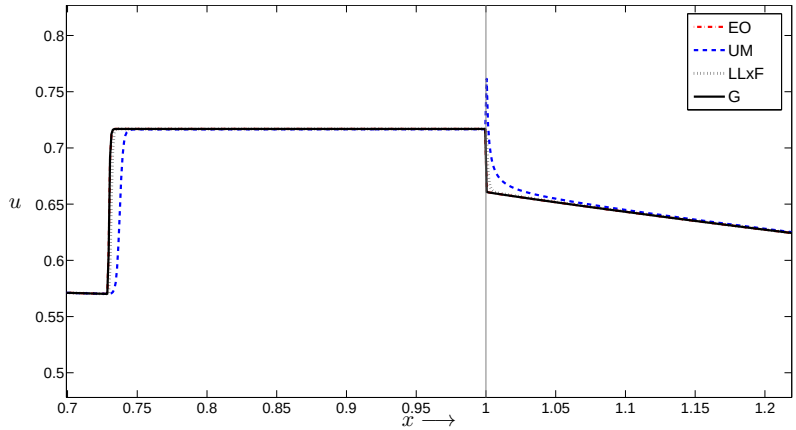

(b) $\Delta x = 0.001$

Figure 4.4.7: The numerical solutions of Experiment C2 at x_h for $t = 1$ with $\Delta x = 0.005$ and $\Delta x = 0.001$

Experiment C1 and C2 should have produced similar solutions, but as we have seen in figure 4.4.2 and 4.4.6 UM approximates a different jump in the solution across x_h than G. To show the difference between the UM- and G-jumps across x_h more clearly , we compare $g(u_{-1})$ and $f(u_1)$ to $g(A)$ and $f(B)$ for both schemes, where u_{-1} is the last node before and u_1 is the first node after x_h. This is done in figure 4.4.8a and 4.4.8b for Experiment C1 and C2, respectively. As seen in the numerical results for C2, G approximates the jump across x_h such that $u_{-1} \approx A$ and $u_1 \approx B$. UM, however, approximate the jump such that $u_{-1} \approx A$ and $u_1 > B$. Since $u_1 > B$ and $g(u_{-1}) \neq f(u_1)$, the entries in definition 3 is violated, we can conclude that UM produces unphysical solutions for Experiment C2. To confirm this conclusion, we can look at the numerical fluxes for both experiments in figures 4.4.9a and 4.4.9b. We see that UM (and the rest of the schemes) approximate the fluxes in a similar manner for both experiments, with no unnatural behavior. We saw in C1 that UM converges to the correct solution if we refined the grid, suggesting that the numerical fluxes where approximated correctly. Thus, when UM still approximate a "spike" solution (even at a refined grid) with a similar numerical flux as C1, the conclusion that UM produces unphysical solution for Experiment C2 is readily clear.

In the next experiments, the flux functions cross in an over- and undercompressive manner, i.e. $g'(u_\chi) > 0$ and $f'(u_\chi) < 0$, and $g'(u_\chi) < 0$ and $f'(u_\chi) > 0$ respectively, where u_χ is the point of intersection. First we consider the cases of flux functions crossing in an overcompressive manner, and as shown in the theory section, the optimal connection and minimal jump condition coincides for these flux functions.

Experiment C3

The left mobility functions are given as

$$\lambda_w^L = 5.595u^3, \qquad \lambda_o^L = 150\,(1-u)^3\,,$$

and the right mobility functions is given as

$$\lambda_o^R = 12u^3, \qquad \lambda_o^R = 30\,(1-u)^3\,,$$

The flux functions are then given as

$$\begin{aligned} g(u) &= \frac{5.595u^3}{5.595u^3 + 150\,(1-u)^3}\left[1 + 150\,(1-u)^3\right] \\ f(u) &= \frac{u^3}{u^3 + \frac{5}{2}\,(1-u)^3}\left[1 + 30\,(1-u)^3\right], \end{aligned} \tag{4.4.4}$$

As figure 4.4.10 shows, the flux functions have equal maximum value, and the (A, B)-connection is chosen as (θ_g, θ_f). The analytical solution for this experiment is again similar as for Experiment C1 and C2, but since $g(\theta_g) = f(\theta_f)$

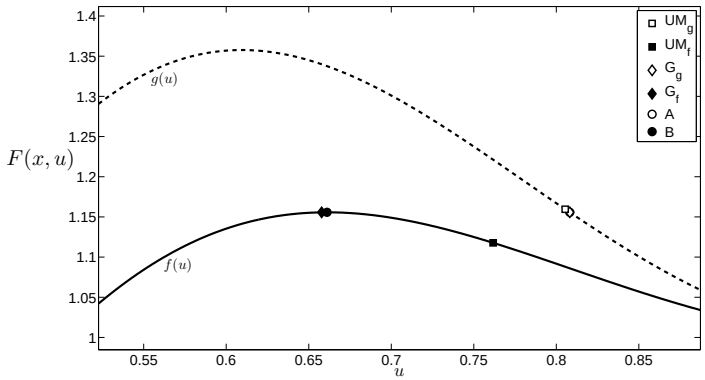

(a) The jump from u_{-1} and u_1 approximated by UM and G for Experiment C1.

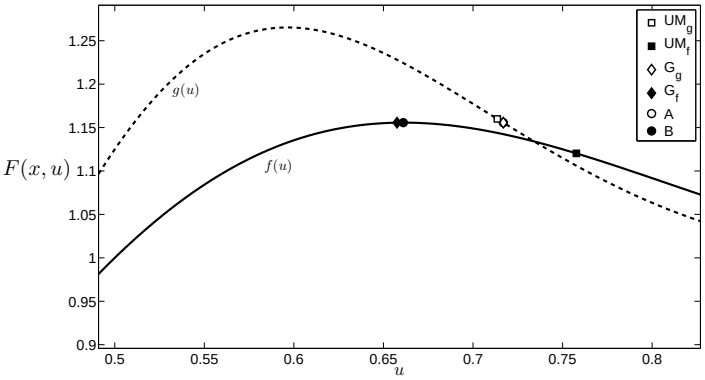

(b) The jump from u_{-1} and u_1 approximated by UM and G for Experiment C2.

Figure 4.4.8: The function values of u_{-1} and u_1 drawn for UM and G for Experiment C1 and C2 at $t = 1$. The subscripts g and f refers to $g(u_{-1})$ and $f(u_1)$, respectively.

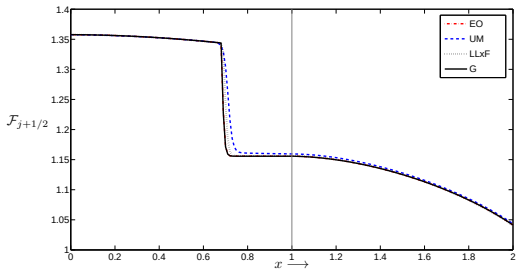

(a) The numerical fluxes, $\mathcal{F}_{j+1/2}$, for EO, UM, LLxF and G in Experiment C1.

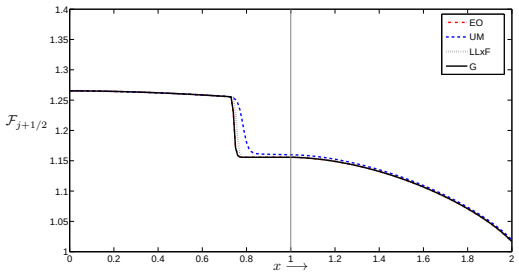

(b) The numerical fluxes, $\mathcal{F}_{j+1/2}$, for EO, UM, LLxF and G in Experiment C2.

Figure 4.4.9: The numerical fluxes, $\mathcal{F}_{j+1/2}$, for all the schemes for C1 and C2 at $t = 1$. Note that $\mathcal{F}_{j+1/2}$ is only valid for $x_{j+1/2}$.

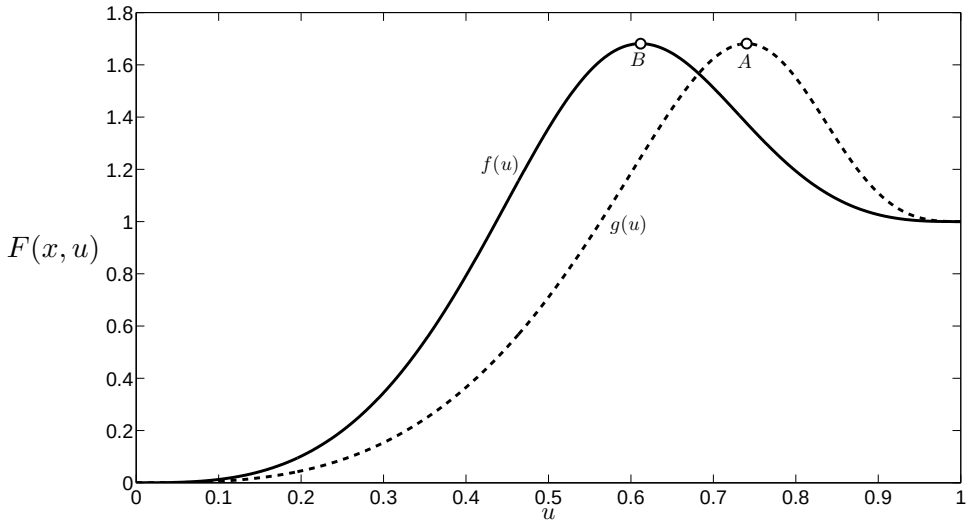

Figure 4.4.10: Flux functions for Experiment C3 with $(A, B) = (\theta_g, \theta_f)$ indicated

we do not get a left going wave after some time as we did for the mentioned experiments. Figure 4.4.11 shows that UM produces a left-going wave after the solution has passed the heterogeneity. After some time we observe that UM has a different jump at x_h than the other schemes. The left and right traces are approximately 0.76 and 0.59 instead of $0.74(\approx A)$ and $0.61(\approx B)$ of EO and G. LLxF follow EO and G away from x_h, but at the heterogeneity the scheme fails to approximate the jump between A and B.

As we did for Experiment C1 and C2 we look at $g(u_{-1})$ and $f(u_1)$ produced by UM and G, and the numerical fluxes for all schemes. In figure 4.4.12a we see that G approximates the (A, B)-connection fairly well, as anticipated. UM stabilizes at a jump where $u_{-1} > A$ and $u_1 < B$, and also $g(u_{-1}) \approx f(u_1)$, thus the conditions in definition 3 is not violated, but in the sense of two-phase flow the optimal entropy condition is not met. Hence the UM solution is unphysical for this experiment. From figure 4.4.12b we see that the numerical flux has no unnatural behavior at the interface, but is generally lower than the numerical fluxes for the other schemes. This tells us that the mass in the porous medium is higher for UM than the other schemes. Comparing $g(u_1)$, $f(u_1)$ and $\mathcal{F}_{j+1/2}$ for UM, we notice that they are approximately the same value, indicating that UM approximates the correct flux values, but with wrong u-values.

Experiments with $g(\theta_g) < f(\theta_f)$ and $g(\theta_g) > f(\theta_f)$ has been done for flux functions crossing in a overcompressive manner, without significant problems in the UM performance. The next cases considers flux functions crossing in a undercompressive manner, and from the theory presented previously we know that the optimal entropy and minimal jump conditions gives different solutions.

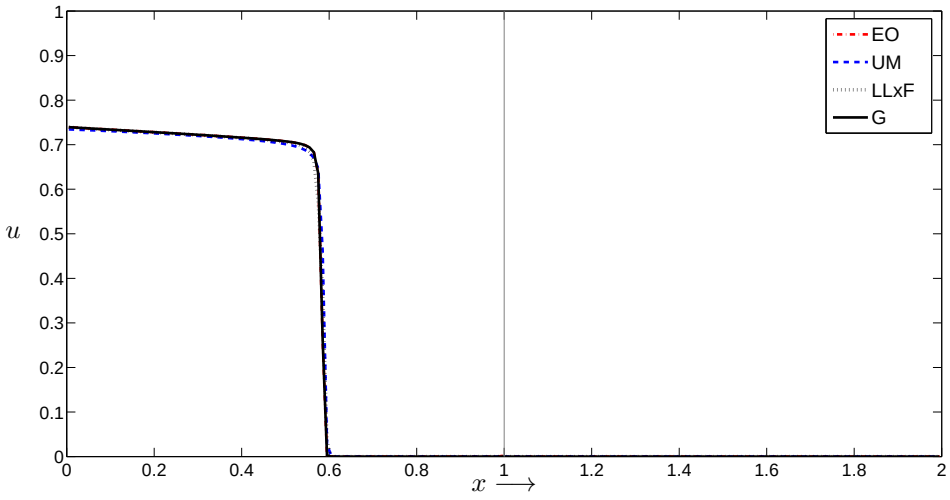

(a) $t = 0.25$

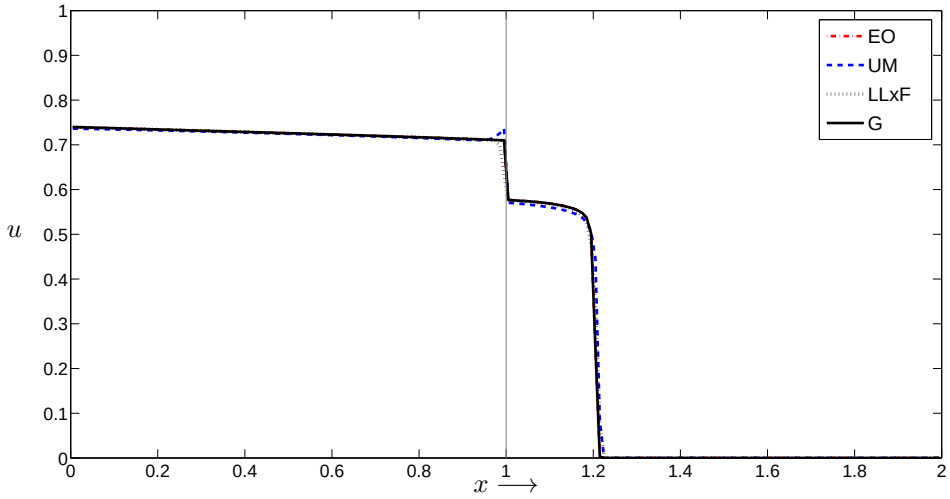

(b) $t = 0.5$

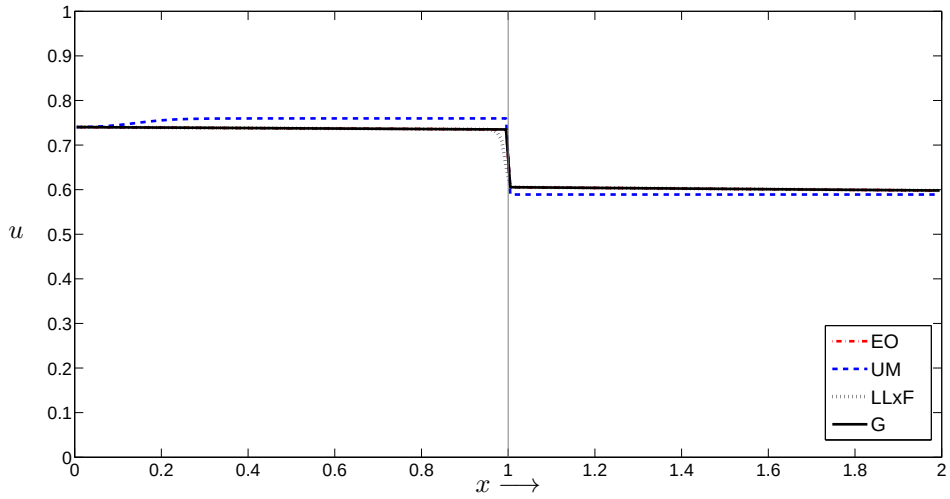

(c) $t = 2.5$

Figure 4.4.11: Numerical solutions for Experiment C3 at $t = 0.25$, $t = 0.5$ and $t = 2.5$

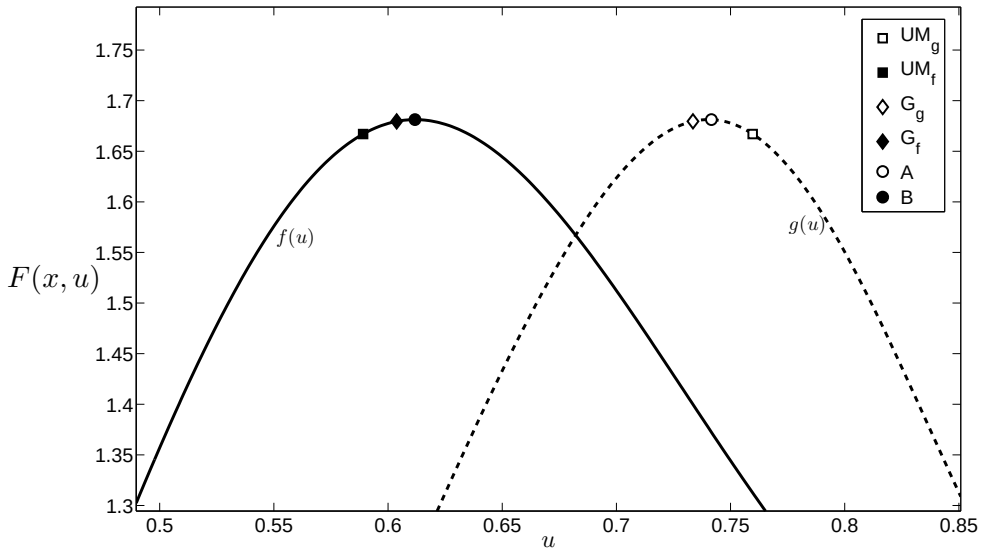

(a) The jump from u_{-1} and u_1 approximated by UM and G for Experiment C3. Recall that the subscripts g and f refers to $g(u_{-1})$ and $f(u_1)$, respectively.

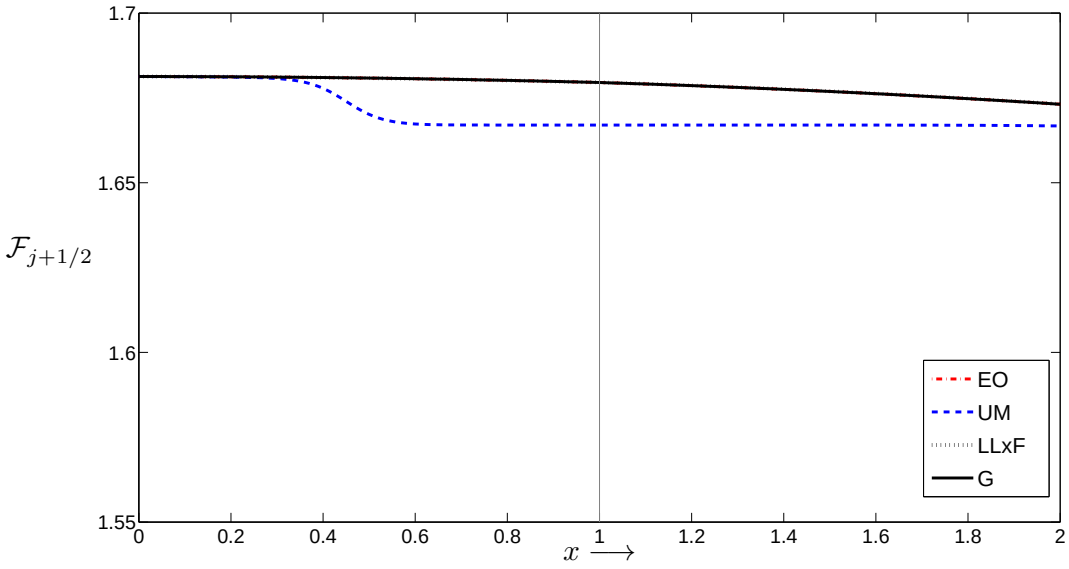

(b) The numerical fluxes, $\mathcal{F}_{j+1/2}$, for EO, UM, LLxF and G in Experiment C3. Note that $\mathcal{F}_{j+1/2}$ is only valid for $x_{j+1/2}$.

Figure 4.4.12: The function values of u_{-1} and u_1 drawn for UM and G for Experiment C3 at $t = 2$. Also, the numerical fluxes for all the schemes at $t = 2$ is illustrated

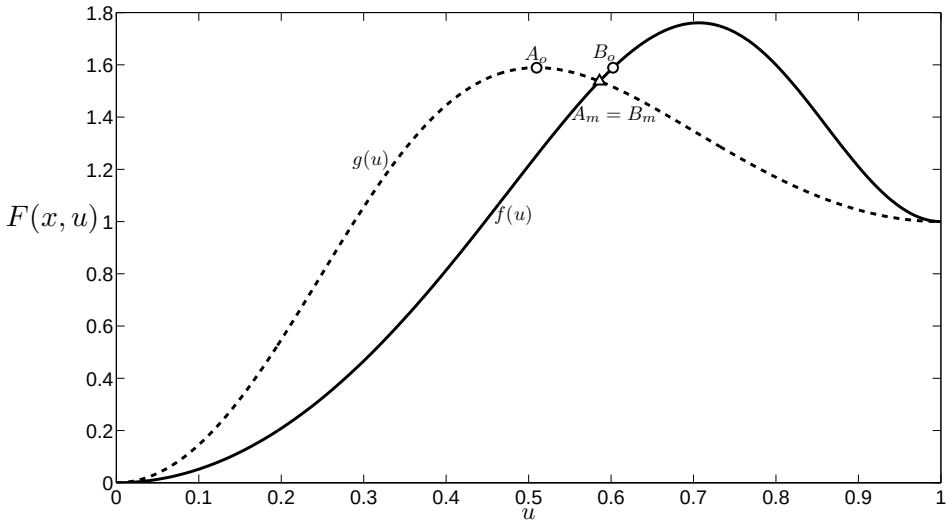

Figure 4.4.13: Flux functions for Experiment C4 with $(A_o, B_o) = \left(\theta_g, \bar{\theta}_g\right)$ ($\circ$) and $(A_m, B_m) = (u_\chi, u_\chi)$ ($\triangle$) indicated

Experiment C4
We let the mobility functions to the left of x_h be

$$\lambda_w^L = 12u^2, \qquad \lambda_o^L = 5\left(1-u\right)^2,$$

and to the right of x_h the mobility functions are

$$\lambda_w^R = 5u^2, \qquad \lambda_o^R = 30\left(1-u\right)^2,$$

The flux functions are given as follows

$$\begin{aligned} g\left(u\right) &= \frac{u^2}{u^2 + \frac{5}{12}\left(1-u\right)^2}\left[1 + 5\left(1-u\right)^2\right], \\ f\left(u\right) &= \frac{u^2}{u^2 + 6\left(1-u\right)^2}\left[1 + 30\left(1-u\right)^2\right], \end{aligned} \tag{4.4.5}$$

and are given in figure 4.4.13 . There are two analytical solutions for this problem, one for the (A_o, B_o)-connection and one for the (A_m, B_m)-connection. The "homogeneous" part is equal for both solutions, but when $t > t_h$ the solutions divide. The optimal connection solution is a jump from $u^-\left(t\right)$ to $u^+\left(t\right)$ as long as $g\left(u^-\left(t\right)\right) < g\left(\theta_g\right)$, and a jump from A_o to B_o when $g\left(u^-\left(t\right)\right) = g\left(\theta_g\right)$. The minimal jump solution also consist of a jump from $u^-\left(t\right)$ to $u^+\left(t\right)$, but here it is valid as long as $g\left(u^-\left(t\right)\right) < g\left(u_\chi\right)$. When $g\left(u^-\left(t\right)\right) \geq g\left(u_\chi\right)$, the solution at the interface is $u^-\left(t\right) = u^+\left(t\right) = u_\chi$, and we get a left-going shock from $\left(g'\right)^{-1}\left(x/t\right)$ to u_χ and a right-going shock from u_χ to u_R, such that the solution in the whole porous medium ultimately becomes $u\left(x,t\right) = u_\chi$. Figure

4.4.14 shows the approximate solutions given by our schemes. As before, the "homogeneous" part ($t \leq t_h$) of the solution is handled well by all the schemes, and the distinction between the schemes arise when $t > t_h$. UM then produces a "spike" at the left side of the interface, x_h. The left trace of UM is therefore lower than the ones given by EO and G, stabilizing at $u_{-1} \approx 0.39$ instead of $A \approx 0.51$. The jump at x_h for EO and G follows the analytical solution for the optimal connection, as expected. We observe that LLxF follows the minimal jump solution, and produces a left-going shock wave for $t > t_h$. Thus, it seems that LLxF, as it is written in the numerical method section, converges to the vanishing viscosity solution (minimal jump solution) as anticipated.

Without showing the experiment, the same solution as above is also produced when the flux functions have equal maximum function value (i.e. $g(\theta_g) = f(\theta_f)$). Hence, the next experiment is when $g(\theta_g) > f(\theta_f)$.

Experiment C5
Here, the mobility functions in the left medium is

$$\lambda_w^L = 12u^2, \qquad \lambda_o^L = 5(1-u)^2,$$

and for the right medium

$$\lambda_w^R = 2.75u^2, \qquad \lambda_o^R = 80(1-u)^2,$$

giving the flux functions

$$\begin{aligned} g(u) &= \frac{u^2}{u^2 + \frac{5}{12}(1-u)^2}\left[1 + 5(1-u)^2\right], \\ f(u) &= \frac{2.75u^2}{2.75u^2 + 80(1-u)^2}\left[1 + 80(1-u)^2\right], \end{aligned} \tag{4.4.6}$$

illustrated in figure 4.4.15. In this experiment the analytical solution for $t \leq t_h$ is a "normal" Buckley-Leverett solution, and for $t > t_h$ we have for the optimal entropy condition, a jump from $u^-(t)$ to $u^+(t)$ for $g(u^-(t)) < g(A)$. When $g(u^-(t)) \geq g(A)$, the solution experience a left-going shock, such that the jump at the interface is from A to B. The minimal jump condition, however is equal to the optimal connection when $g(u^-(t)) < g(u_\chi)$. When $g(u^-(t)) \geq g(u_\chi)$, the solution at the interface is $u^-(t) = u^+(t) = u_\chi$, and the solution is similar as for Experiment C4 where after some time the water saturation in the porous medium becomes $u(x,t) = u_\chi$. In figure 4.4.16 the numerical solutions for this experiment is presented. 4.4.16a shows similar results as the ones from Experiment C4. UM has a "spike" just to the left of x_h, EO and G are performing similarly well across the interface. LLxF follows the minimal jump condition giving a left- and right-going shock with saturation $u = u_\chi$. In

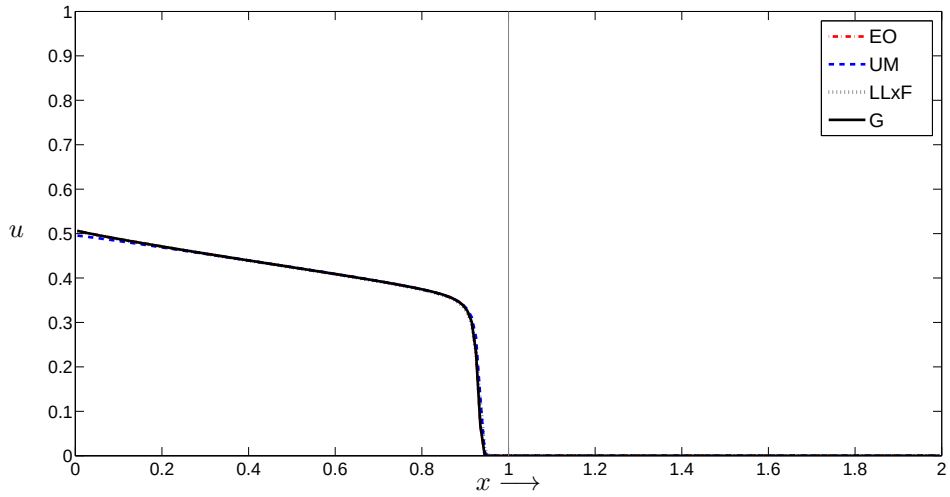

(a) $t = 0.25$

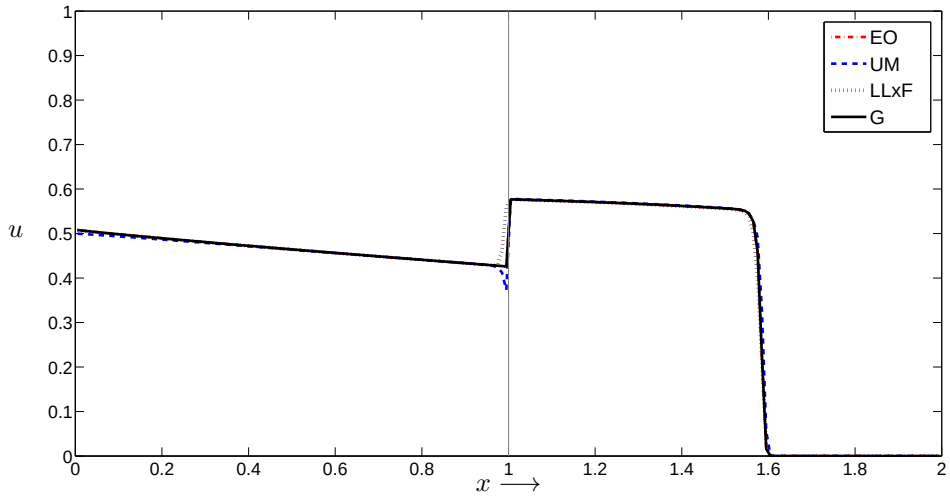

(b) $t = 0.5$

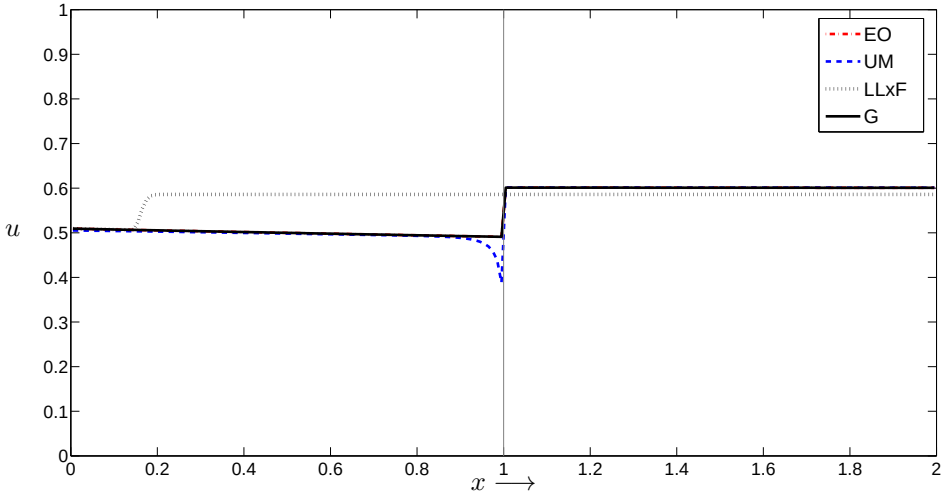

(c) $t = 2.5$

Figure 4.4.14: Numerical solution of Experiment C4 at $t = 0.25$, $t = 0.5$ and $t = 2.5$

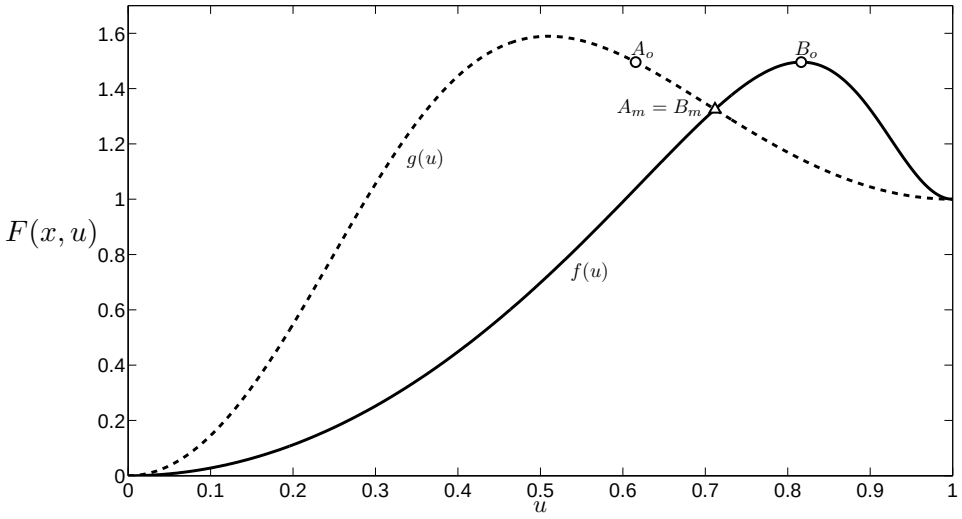

Figure 4.4.15: Flux functions for Experiment C5 with $(A_o, B_o) = \left(\bar{\theta}_f, \theta_f\right)$ ($\circ$) and $(A_m, B_m) = (u_\chi, u_\chi)$ ($\triangle$) indicated

figures 4.4.16b and 4.4.16c we have $g\left(u^-\left(t\right)\right) > g\left(A\right)$, thus the left-going shock wave for the optimal entropy condition starts propagating. Now, the "spike" in the UM solution shift from being on the left side of x_h to being on the right side. Also, UM does not follow the the left-going shock as well as EO and G.

Experiment C4 and C5 involved similar type of solutions, both analytically and numerical, hence some shared comments can be made. The most notable observations seen in the experiments were the approximate solution of LLxF. From figure 4.4.14c and 4.4.16c, we see that the area under the LLxF solution is higher than the area under the other schemes' solutions, meaning the mass in the medium is higher for the LLxF solution in than the other schemes. To fulfill the mass conservation principle, a higher mass in the system must imply a lower flux. In figures 4.4.17a and 4.4.17b we confirm that the numerical flux for LLxF is lower than the other schemes.

We did not show figures of refined grids of these experiments. The "spike" in the solutions has the same properties as the "spike"-solution of UM in Experiment C2. It is still present with the same height when the mesh size is reduced.

Before we move on to the next experiments, we want to see how LLxF perform against EO and G if we set their (A, B)-connections to approximate the minimal jump condition. This is only done for Experiment C5 at $t = 1$ with the usual mesh size of $\Delta x = 0.01$, and is shown in figure 4.4.18. We see that LLxF approximates the minimal jump solution almost as good as EO-MJ and G-MJ. Only small numerical dispersion is visible.

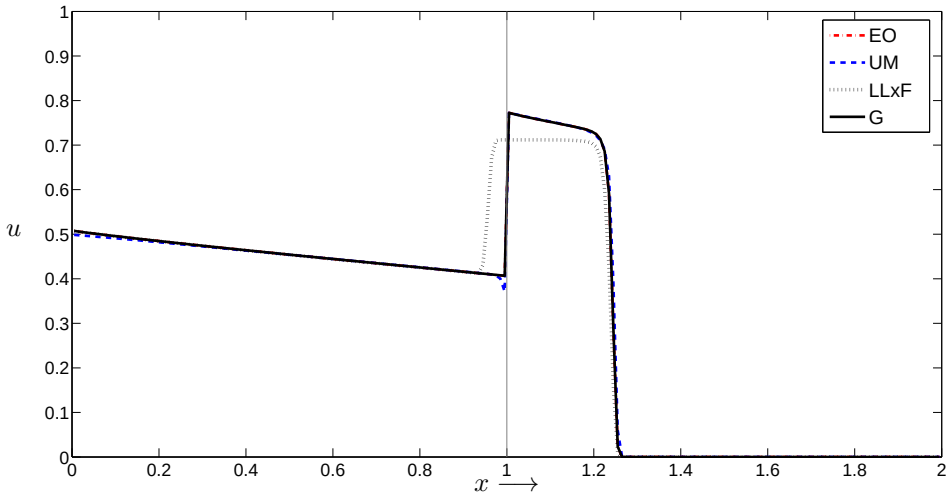

(a) $t = 0.4$

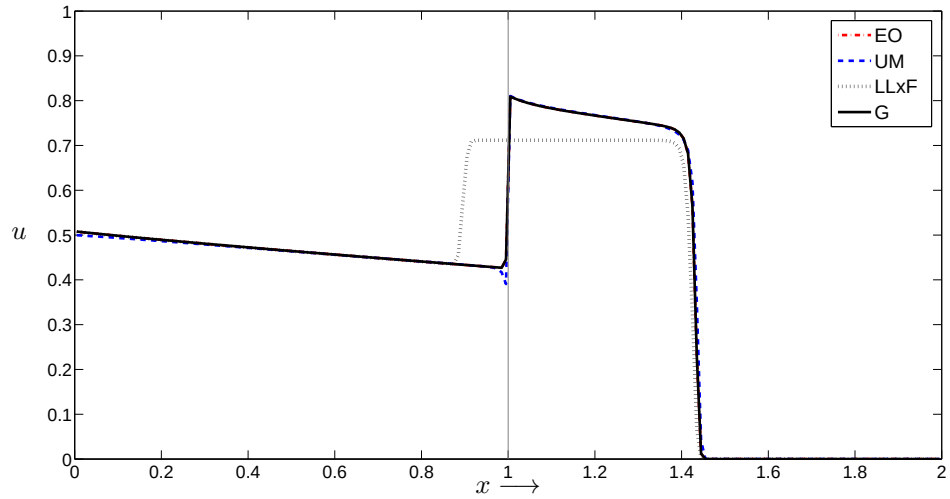

(b) $t = 0.5$

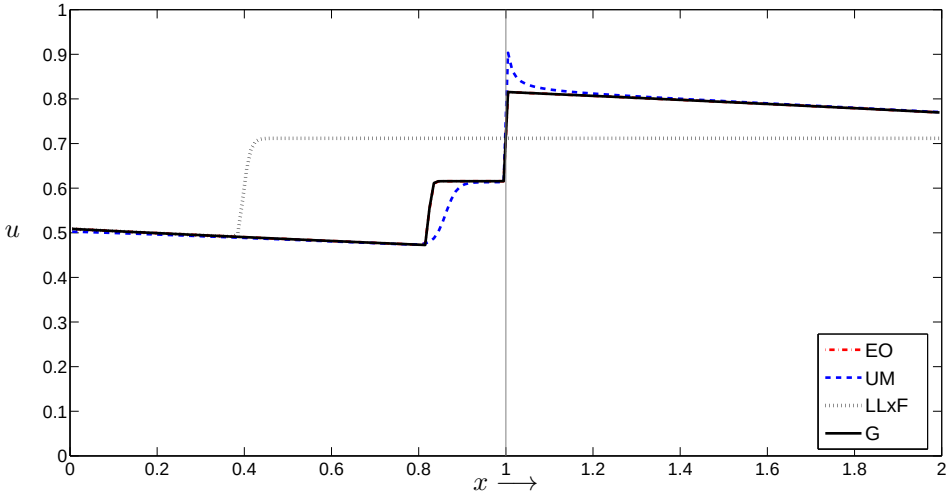

(c) $t = 1$

Figure 4.4.16: The numerical solutions for Experiment C5 at $t = 0.4$, $t = 0.5$ and $t = 1$

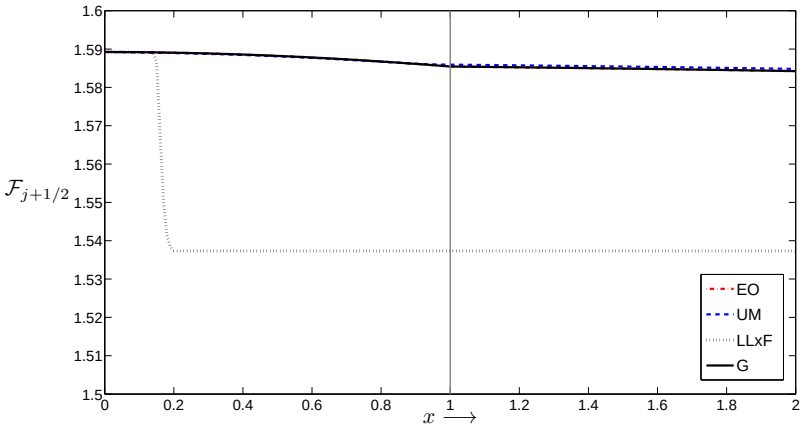

(a) Numerical fluxes for Experiment C4 at $t = 0.75$

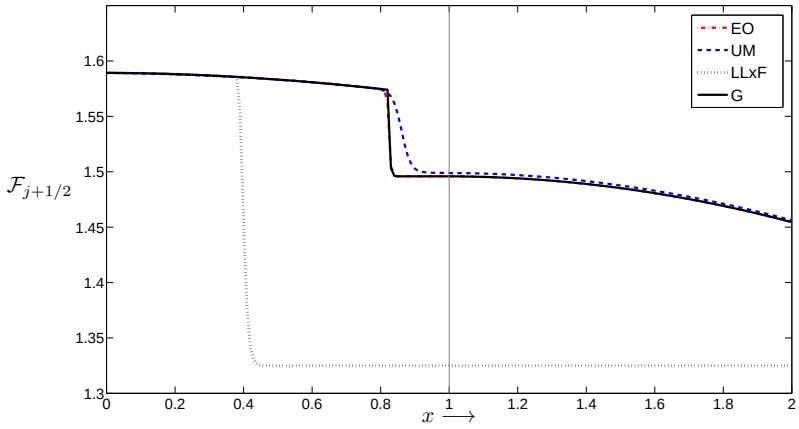

(b) Numerical fluxes for Experiment C5 at $t = 1$

Figure 4.4.17: The numerical flux approximations for all the schemes for Experiment C4 and C5.

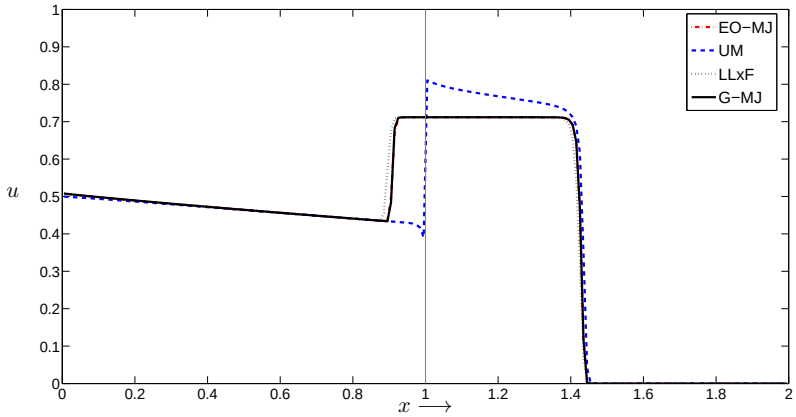

Figure 4.4.18: Numerical solution for Experiment C5 at $t = 1$ with EO and G approximating the minimal jump condition

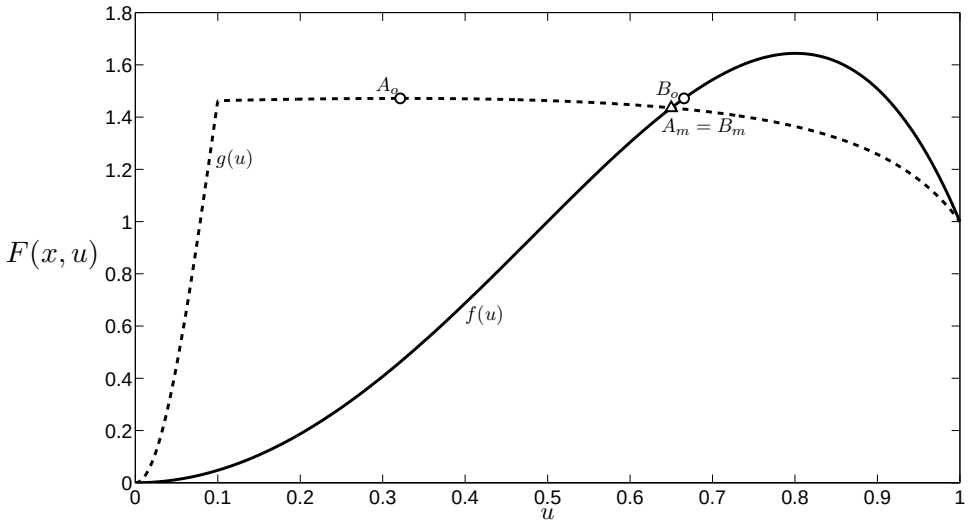

Figure 4.4.19: Flux functions for Experiment C6 with $(A_o, B_o) = \left(\theta_g, \bar{\theta}_g\right)$ ($\circ$) and $(A_m, B_m) = (u_\chi, u_\chi)$ ($\triangle$) indicated

From the experiments above, we see that UM follows the optimal entropy condition, qualitatively speaking. An interesting question if therefore: can we make UM follow the minimal jump condition? In [18] they showed that for gravity-segregation, i.e. flow only influenced by the gravity term ($v = 0$), UM followed the minimal jump condition for some modified flux functions. But will UM do the same for a dynamic system like our model? The question is answered in the next experiment.

Experiment C6

The left mobility function are slightly modified compared to previous experiments, and is given as

$$\lambda_w^L = \begin{cases} \approx 161.4u^2, & \text{if } u < 0.1, \\ \approx 0.14u + 1.6, & \text{if } u \geq 0.1, \end{cases}$$
$$\lambda_o^L = 5\left(1 - u^2\right),$$

and for the right mobility functions, we have the formulae

$$\lambda_w^R = 4u^2, \qquad \lambda_o^R = 5\left(1 - u^2\right),$$

This gives us the flux functions

$$\begin{aligned} g(u) &= \begin{cases} \frac{u^2}{u^2 + \frac{5}{161.4}(1-u^2)} \left[1 + 5\left(1 - u^2\right)\right], & \text{if } u < 0.1, \\ \frac{0.14u+1.6}{0.14u+1.6+5(1-u^2)} \left[1 + 5\left(1 - u^2\right)\right], & \text{if } u \geq 0.1, \end{cases} \\ f(u) &= \frac{u^2}{u^2 + \frac{5}{4}(1-u)^2} \left[1 + 5\left(1 - u^2\right)\right], \end{aligned} \tag{4.4.7}$$

which is shown in figure 4.4.19. The analytical solutions look slightly different for the "homogeneous" part than the ones presented in Experiment C4, but in principle they are the same. Hence we refer to that experiment for the solution procedure. From figure 4.4.20 we see that EO and G follow the optimal entropy solution at the interface, as expected. UM, however, does not follow the optimal entropy solution. As we clearly see in figure 4.4.20c, UM follows LLxF, and both schemes approximates the minimal jump entropy solution $u = u_\chi = 0.65$. This contradicts the results presented in the last experiments where UM, qualitatively speaking, followed the optimal entropy solution.

In figure 4.4.21 we have plotted the numerical fluxes for all schemes at $t = 1.5$. From this figure we see that UM and LLxF approximates the same numerical fluxes, which is lower than the approximated fluxes of EO and G. As we observed under Experiment C5 the mass accumulated in the medium is higher for UM and LLxF than for the other schemes. Hence, we again have the situation where a lower flux value is approximated to fulfill the mass conservation principle, which is the basis for conservative schemes.

Experiment C7
We use the same mobility functions as the last experiment

$$\lambda_w^L = \begin{cases} \approx 161.4u^2, & \text{if } u < 0.1, \\ \approx 0.14u + 1.6, & \text{if } u \geq 0.1, \end{cases}$$
$$\lambda_o^L = 5\left(1 - u^2\right),$$

and modify the right mobility functions as follows

$$\lambda_w^R = 4u^2, \qquad \lambda_o^R = 2.9\left(1 - u^2\right),$$

giving the flux functions

$$\begin{aligned} g(u) &= \begin{cases} \frac{u^2}{u^2 + \frac{5}{161.4}(1-u^2)}\left[1 + 5\left(1 - u^2\right)\right], & \text{if } u < 0.1, \\ \frac{0.14u+1.6}{0.14u+1.6+5(1-u^2)}\left[1 + 5\left(1 - u^2\right)\right], & \text{if } u \geq 0.1, \end{cases} \\ f(u) &= \frac{u^2}{u^2 + \frac{2.9}{4}(1-u)^2}\left[1 + 2.9\left(1 - u^2\right)\right], \end{aligned} \tag{4.4.8}$$

Figure 4.4.22 shows the flux functions, and we note that this is a similar experiment as the previous one, but now $f(u)$ has a lower maximum value, thus the optimal connection is $(A_o, B_o) = \left(\bar{\theta}_f, \theta_f\right)$. The analytical solution for this experiment is similar to Experiment C5, although here the flux function $g(u)$ is slightly differently shaped. Since $g(u)$ is equal to the previous experiment, we omit the "homogeneous" part of the numerical approximations, and focus on the solutions when $t > t_h$ for each method. The numerical solutions is

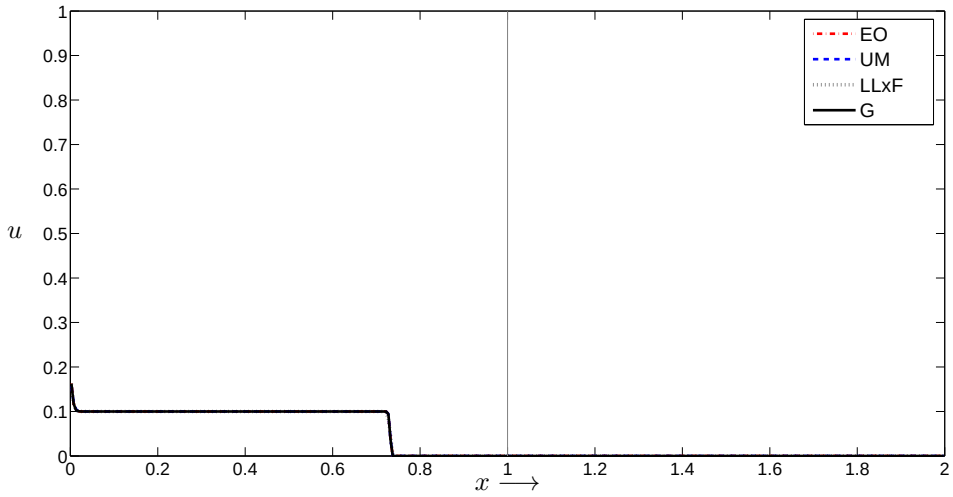

(a) $t = 0.05$

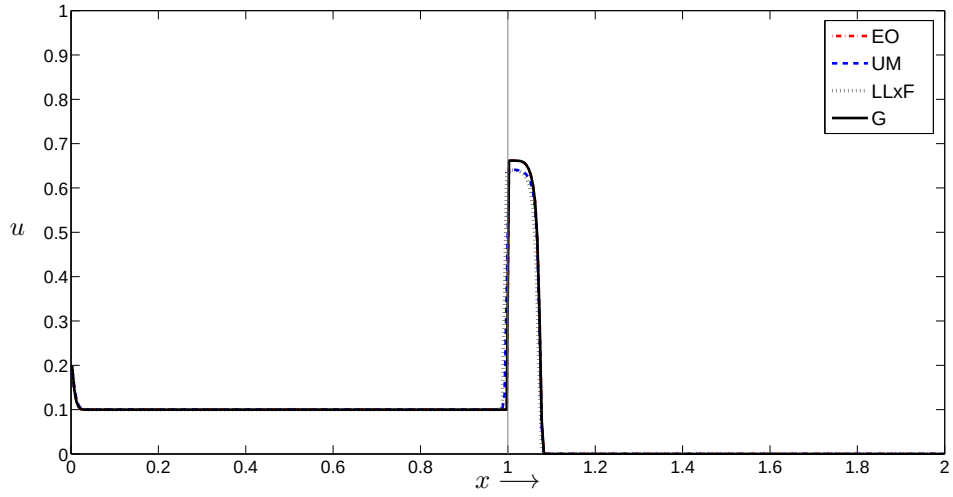

(b) $t = 0.1$

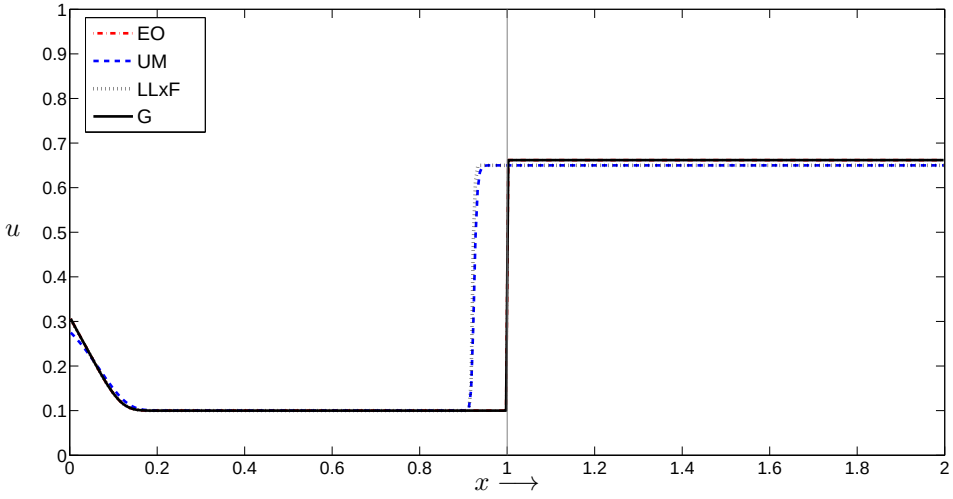

(c) $t = 1.5$

Figure 4.4.20: The numerical solutions for Experiment C6 at $t = 0.05$, $t = 0.1$ and $t = 1.5$

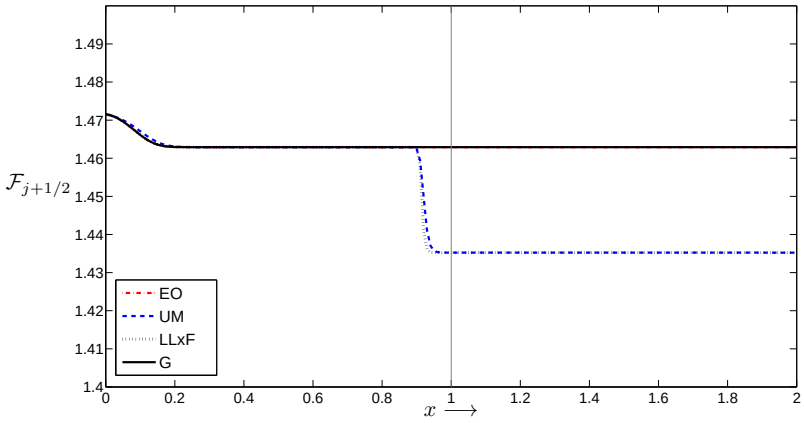

Figure 4.4.21: Numerical flux approximations for Experiment C6 at $t = 1.5$

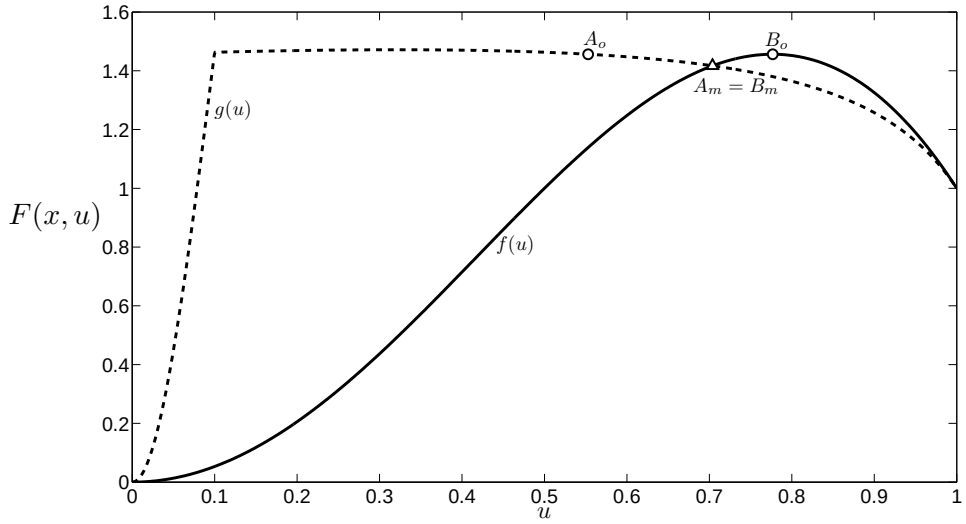

Figure 4.4.22: Flux functions for Experiment C7 with $(A_o, B_o) = \left(\bar{\theta}_f, \theta_f\right)$ ($\circ$) and $(A_m, B_m) = (u_\chi, u_\chi)$ ($\triangle$) indicated

shown in figure 4.4.23. Here we see that EO and G approximates a similar solution as in Experiment C5, with a left-going shock wave developing over time. LLxF approximates the minimal jump solution with a left-going shock wave with $u = u_\chi$. UM, however, does not follow any of the interface entropy solutions, not even qualitatively. The jump UM approximates, is from $u_{-1} \approx 0.82$ to $u_1 \approx 0.65$, which is far from both $(A_o, B_o) \approx (0.56, 0.78)$ and $(A_m, B_m) \approx (0.7, 0.7)$.

To investigate the results of UM further, we plot the function values of u_{-1} and u_1, and also the numerical fluxes in figure 4.4.24. From figure 4.4.24a we see that the jump from $g(u)$ to $f(u)$ approximated by UM, is such that

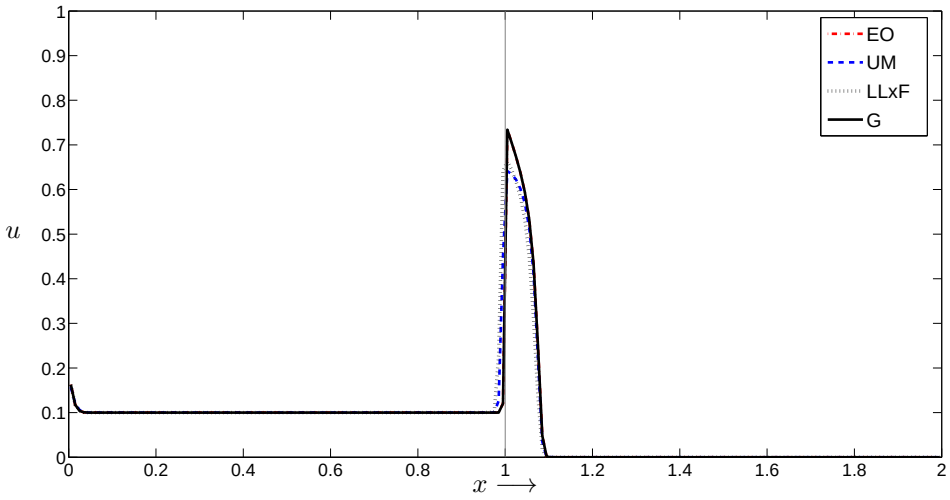

(a) $t = 0.1$

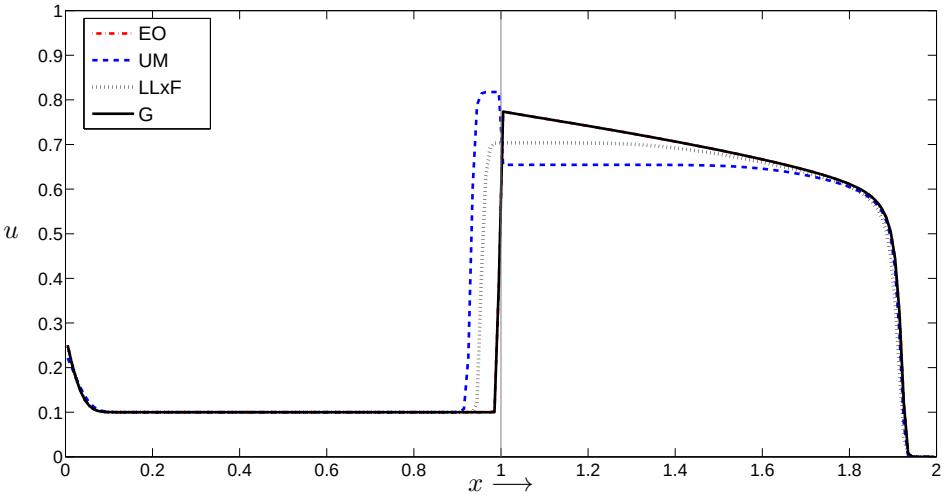

(b) $t = 0.5$

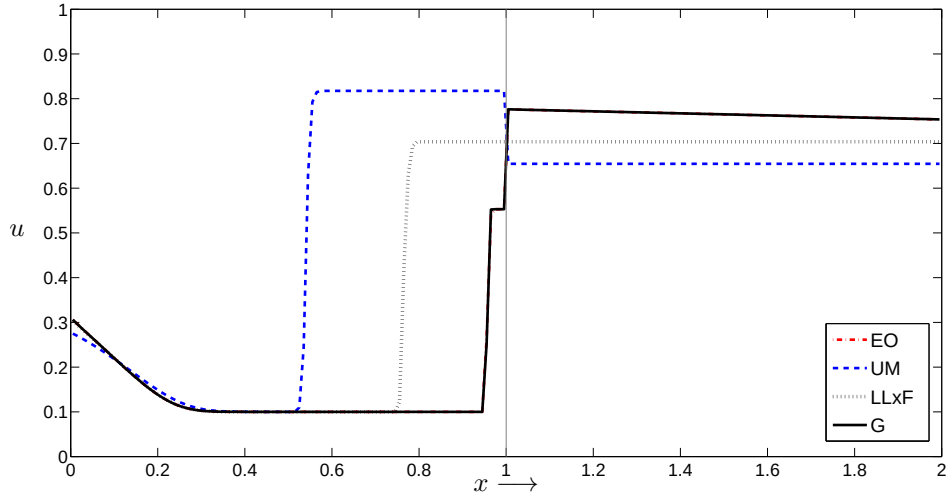

(c) $t = 3$

Figure 4.4.23: The numerical solutions for Experiment C7 at $t = 0.1$, $t = 0.5$ and $t = 3$

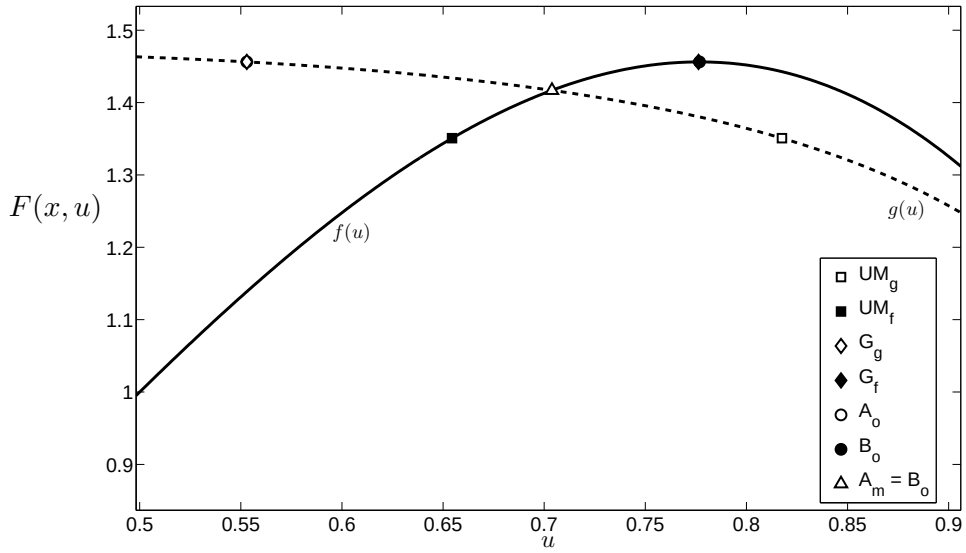

(a) The jump from u_{-1} and u_1 approximated by UM and G for Experiment C7. Recall that the subscripts g and f refers to $g(u_{-1})$ and $f(u_1)$, respectively.

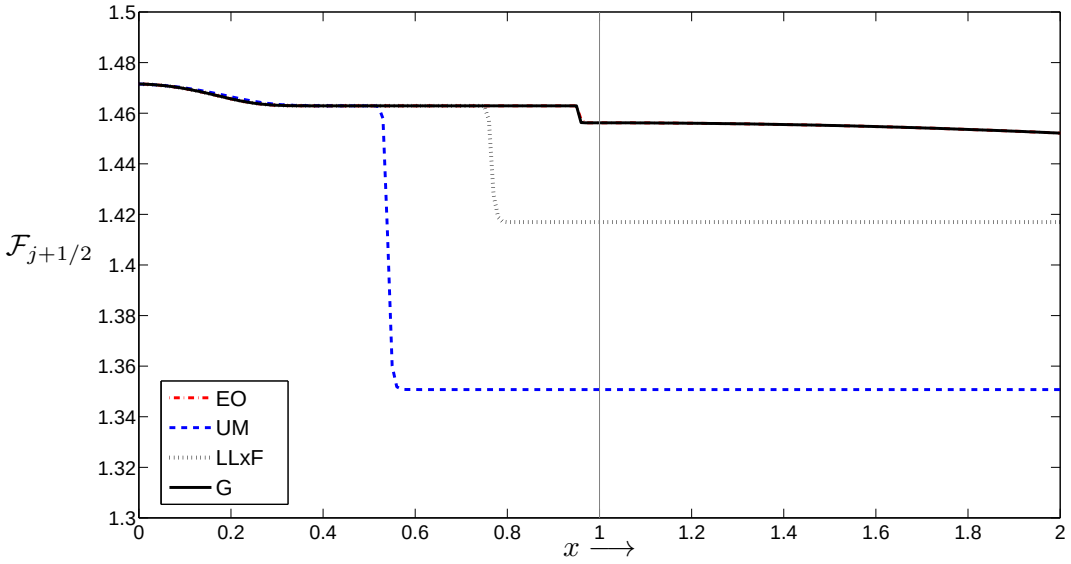

(b) Numerical flux approximations for Experiment C7 at $t = 3$

Figure 4.4.24: The function values of u_{-1} and u_1 for UM and G, and numerical fluxes for all scheme drawn for Experiment C7 at $t = 3$.

$g(u_{-1}) = f(u_1)$, $\theta_g < u_{-1} < 1$ and $0 < u_1 < \theta_f$, thus making it a valid jump in the sense of definition 4.4.21. The numerical fluxes in figure shows an interesting situation. Here UM and LLxF differs from the EO and G fluxes, but also from each other. The UM numerical flux is the lowest, followed by LLxF, and EO and G has the highest flux approximation. This suggest that the mass accumulated by UM is higher than for the LLxF, which again is higher than both EO and G. The same conclusion can be made if we look at figure 4.4.23c, where the area under the solution for UM is greater than the area under the LLxF solution, which again is greater than the area under the solutions made by EO and G.

4.5 Discussion of Downdip Flow

We have seen in the test scenarios for downdip flow that UM have some difficulties approximating the correct solution. It is therefore useful to discuss how UM solves the problem of downdip flow, and try to explain the behavior of the scheme. We will not give any condition for the UM scheme, or set some restriction on the solution, but only indicate a new way on looking at the solution procedure in downdip flow regimes.
From the numerical method section, we know that UM first evaluates which direction the phases are flowing through the sign of θ_1 and θ_2 (c.f. section 3.5), and based on the results, chooses which saturation value (u-value) to use for the water and oil mobility functions. In downdip flow the phases may move in opposite direction of each other, depending on the flux functions. This is indeed the situation in all of our experiments under test scenario C, mainly because we have chosen the gravity influence to be significant. If we assume countercurrent flow, the saturation values on both sides of the heterogeneity, $x = x_h$, is calculated by the following equations for UM (see (3.1.6) and section 3.5):

$$\begin{aligned} u_{-1}^{n+1} = u_{-1}^n - \frac{\Delta t}{\Delta x}\Bigg[& \frac{\lambda_w^L\left(u_{-1}^n\right)}{\lambda_w^L\left(u_{-1}^n\right) + \lambda_o^R\left(u_1^n\right)}\left[1 + \lambda_o^R\left(u_1^n\right)\right] \\ & - \frac{\lambda_w^L\left(u_{-2}^n\right)}{\lambda_w^L\left(u_{-2}^n\right) + \lambda_o^L\left(u_{-1}^n\right)}\left[1 + \lambda_o^L\left(u_{-1}^n\right)\right]\Bigg], \end{aligned} \tag{4.5.1}$$

$$\begin{aligned} u_1^{n+1} = u_1^n - \frac{\Delta t}{\Delta x}\Bigg[& \frac{\lambda_w^R\left(u_1^n\right)}{\lambda_w^R\left(u_1^n\right) + \lambda_o^R\left(u_2^n\right)}\left[1 + \lambda_o^R\left(u_2^n\right)\right] \\ & - \frac{\lambda_w^L\left(u_{-1}^n\right)}{\lambda_w^L\left(u_{-1}^n\right) + \lambda_o^R\left(u_1^n\right)}\left[1 + \lambda_o^R\left(u_1^n\right)\right]\Bigg]. \end{aligned} \tag{4.5.2}$$

We know that $\Delta t/\Delta x$ is restricted by the CFL-condition, and is generally a fixed factor. Thus, if we want to know when $u_{-1}^{n+1} = u_{-1}^n$ and $u_1^{n+1} = u_1^n$, we can study when the flux terms cancel each other. From this observation we see that we can calculate for which u_{-2}, u_{-1} and u_1 in (4.5.1) and u_{-1}, u_1 and u_2 in (4.5.2) this happens.
One possible way the flux terms can cancel each other is if

$$\lambda_w^L(u_{-2}) = \lambda_w^L(u_{-1}), \quad \lambda_o^L(u_{-1}) = \lambda_o^R(u_1), \tag{4.5.3}$$

for (4.5.1) and

$$\lambda_w^L(u_{-1}) = \lambda_w^R(u_1), \quad \lambda_o^L(u_1) = \lambda_o^R(u_2), \tag{4.5.4}$$

for (4.5.2). Generally, under assumption of countercurrent flow, the flux terms can cancel each other if

$$\lambda_w(u_{j-1}) = \lambda_w(u_j), \quad \lambda_o(u_j) = \lambda_o(u_{j+1}), \tag{4.5.5}$$

when calculating u_j. From the properties of λ_l given in section 4.1, we can deduce the that $\lambda_w(u_{j-1}) = \lambda_w(u_j)$ if $u_{j-1} = u_j$ and $\lambda_o(u_j) = \lambda_o(u_{j+1})$ if $u_j = u_{j+1}$, *except* for $\lambda_w^L(u_{-1}) = \lambda_w^R(u_1)$ and $\lambda_o^L(u_{-1}) = \lambda_o^R(u_1)$ which does not imply $u_{-1} = u_1$. Thus, if the flux terms cancel each other due to equal mobility functions, the reservoir will stabilize at $u = u_{-1}$ for $x < x_h$ and $u = u_1$ for $x > x_h$. We stress that this is only *one* possible way the flux terms can cancel each other.
To simplify the notation, we define

$$\begin{aligned}\Delta_-\mathcal{F} =& \frac{\lambda_w^L\left(u_{-1}^n\right)}{\lambda_w^L\left(u_{-1}^n\right) + \lambda_o^R\left(u_1^n\right)}\left[1 + \lambda_o^R\left(u_1^n\right)\right] \\ &- \frac{\lambda_w^L\left(u_{-2}^n\right)}{\lambda_w^L\left(u_{-2}^n\right) + \lambda_o^L\left(u_{-1}^n\right)}\left[1 + \lambda_o^L\left(u_{-1}^n\right)\right],\end{aligned} \tag{4.5.6}$$

$$\begin{aligned}\Delta_+\mathcal{F} =& \frac{\lambda_w^R\left(u_1^n\right)}{\lambda_w^R\left(u_1^n\right) + \lambda_o^R\left(u_2^n\right)}\left[1 + \lambda_o^R\left(u_2^n\right)\right] \\ &- \frac{\lambda_w^L\left(u_{-1}^n\right)}{\lambda_w^L\left(u_{-1}^n\right) + \lambda_o^R\left(u_1^n\right)}\left[1 + \lambda_o^R\left(u_1^n\right)\right].\end{aligned} \tag{4.5.7}$$

In the sense of (3.1.6), $\Delta_-\mathcal{F} = \overline{F}\left(u_{-1}^n, u_1^n\right) - G\left(u_{-2}^n, u_{-1}^n\right)$ and $\Delta_+\mathcal{F} = F\left(u_1^n, u_2^n\right) - \overline{F}\left(u_{-1}^n, u_1^n\right)$. In the following we investigate the experiments in test scenario C to see if the (A, B)-connections is included in the possible u_{-1} and $\underline{u_1}$ which makes $\Delta_-\mathcal{F} = 0$ and $\Delta_+\mathcal{F} = 0$. This is done in anticipation that we can say something about the solution UM approximates. We also check if (4.5.5) is valid for any of the experiments. Note that, the analytical solution for the downdip flow stabilizes at the (A, B)-connection when $t \to \infty$ and the initial conditions are $u_L = 1$ and $u_R = 0$. To easily see when $\Delta_-\mathcal{F} = 0$ and $\Delta_+\mathcal{F} = 0$, we plot the implicit functions with respect to their u-values, and analyze them in the (u_{-1}, u_1)-plane.

Experiment C1
In figure 4.5.1 we see the plots of $\Delta_-\mathcal{F} = 0$ and $\Delta_+\mathcal{F} = 0$ in the (u_{-1}, u_1)-plane with $(A, B) = \left(\bar{\theta}_f, \theta_f\right)$ indicated. From figure 4.5.1a we see that there is no u_{-2} such that $\Delta_-\mathcal{F} = 0$ with $(u_{-1}, u_1) = (A, B)$. From the conclusions made in experiment C1, we know that refining the grid, UM seemed to converge towards the correct physical solution, (A, B), at the interface. This suggest that the analysis of $\Delta_-\mathcal{F}$ and $\Delta_+\mathcal{F}$ might not be a sufficient tool for completely describing the UM scheme for downdip flow. On the other hand, we noted that the left and right traces were $(u_{-1}, u_1) \approx (0.81, 0.76)$ even with $\Delta x = 0.001$, which according to figure 4.5.1 is within the area such that $\Delta_-\mathcal{F} = 0$ and $\Delta_+\mathcal{F} = 0$. Thus, if for some reason the scheme does not converge to the (A, B)-solution (which we believe it does), $(u_{-1}, u_1) \approx (0.81, 0.76)$ might be the solution it converges to. Checking (4.5.5) we get $\lambda_o^L(u_{-1}) = \lambda_o^R(u_1)$, but $\lambda_w^L(u_{-1}) \neq \lambda_w^R(u_1)$ and $u_2 \neq u_1$. Thus, the flux terms cancel each other in a different manner than the one suggested in (4.5.5).

Experiment C2
In this experiment, we obtain the same results as the previous. There exist no u_{-2} such that $\Delta_-\mathcal{F} = 0$ with u_{-1} and u_1 equal to A and B, respectively (c.f. figure 4.5.2a). In figures 4.4.6, 4.4.7a and 4.4.7b we saw that the left and right traces for UM was $(u_{-1}, u_1) \approx (0.71, 0.76)$. These values lies within the region such that $\Delta_-\mathcal{F} = 0$ and $\Delta_+\mathcal{F} = 0$. Hence, it seems that UM converges towards this jump at the interface as $t \to \infty$. If we check (4.5.5), we get the same conclusions as in Experiment C1. There is no equality of the mobility functions at x_h.

Experiment C3
We see from figure 4.5.3 that $(u_{-1}, u_1) = (A, B)$ is a possibility, but from the numerical solution presented in figure 4.5.3, wee see that UM still chooses a different jump across x_h. To investigate this we need to look at which u_{-2}- and u_2-values is needed such that $\Delta_-\mathcal{F} = 0$ and $\Delta_+\mathcal{F} = 0$ if $(u_{-1}, u_1) = (A, B)$. By inserting $(u_{-1}, u_1) = (A, B)$ in (4.5.6) and (4.5.7), and then solving $\Delta_-\mathcal{F} = 0$ and $\Delta_+\mathcal{F} = 0$, we get the results $u_{-2} \neq A$ and $u_2 \neq B$. This means that if UM were to approximate the (A, B)-solution it would not have stabilized the solution as $u = A$ for $x < x_h$ and $u = B$ for $x > x_h$, if our observation on the flux terms holds. In our numerical results, UM approximates the jump $(u_{-1}, u_1) \approx (0.76, 0.59)$. Inserting these values in $\Delta_-\mathcal{F} = 0$ and $\Delta_+\mathcal{F} = 0$ we get $u_{-2} \approx u_{-1}$ and $u_2 \approx u_1$, which we also observe in figure 4.4.11. Checking the mobility functions in (4.5.5), we get $\lambda_w^L(u_{-1}) = \lambda_w^R(u_1)$ and $\lambda_o^L(u_{-1}) = \lambda_o^R(u_1)$. Thus, the flux terms in UM cancel each other out, because (4.5.5) is fulfilled.

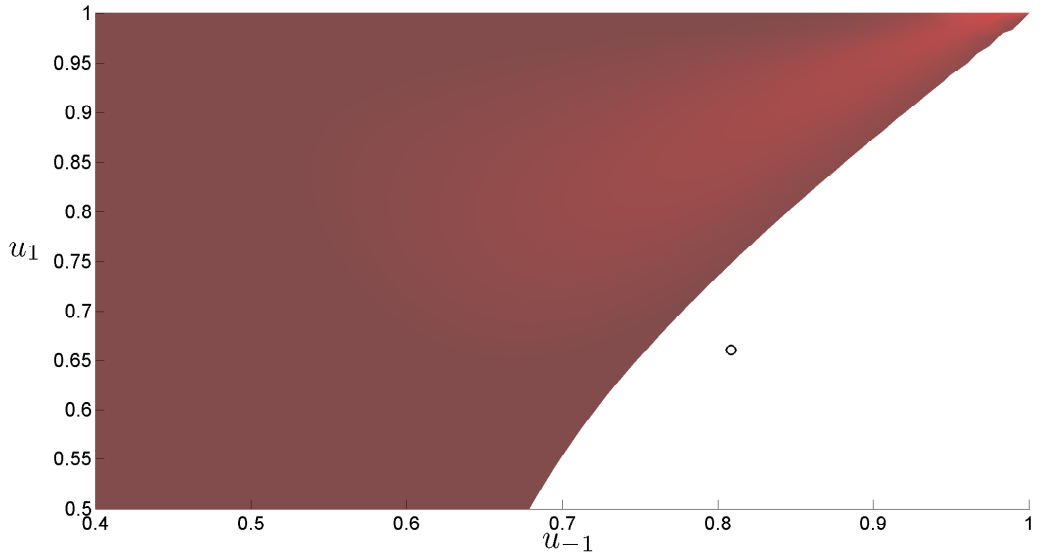

(a) $\Delta_{-}\mathcal{F} = 0$

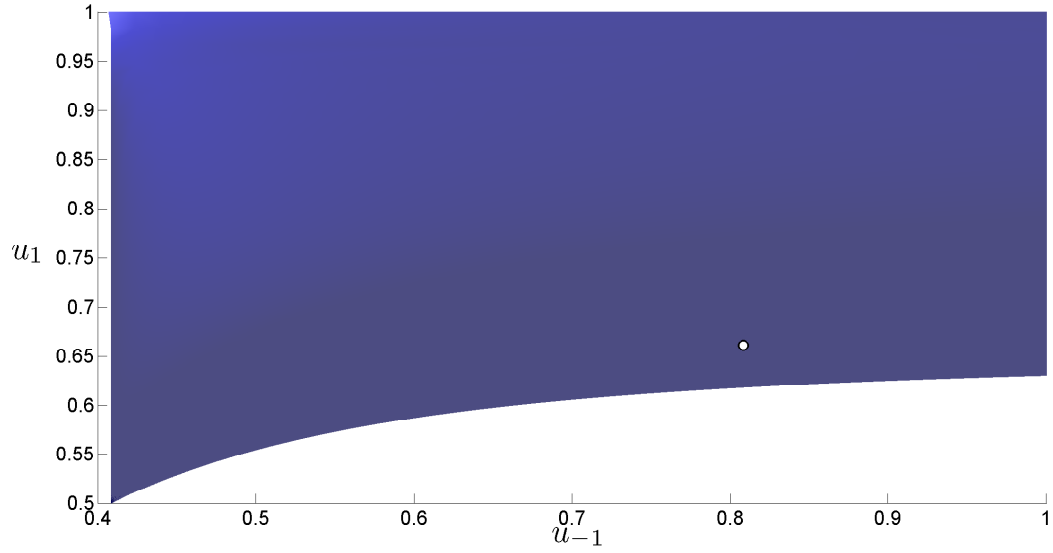

(b) $\Delta_{+}\mathcal{F} = 0$

Figure 4.5.1: Plot of $\Delta_{-}\mathcal{F} = 0$ and $\Delta_{+}\mathcal{F} = 0$ for Experiment C1 with $(A, B) = \big(\bar{\theta}_f, \theta_f\big)(\circ)$ indicated

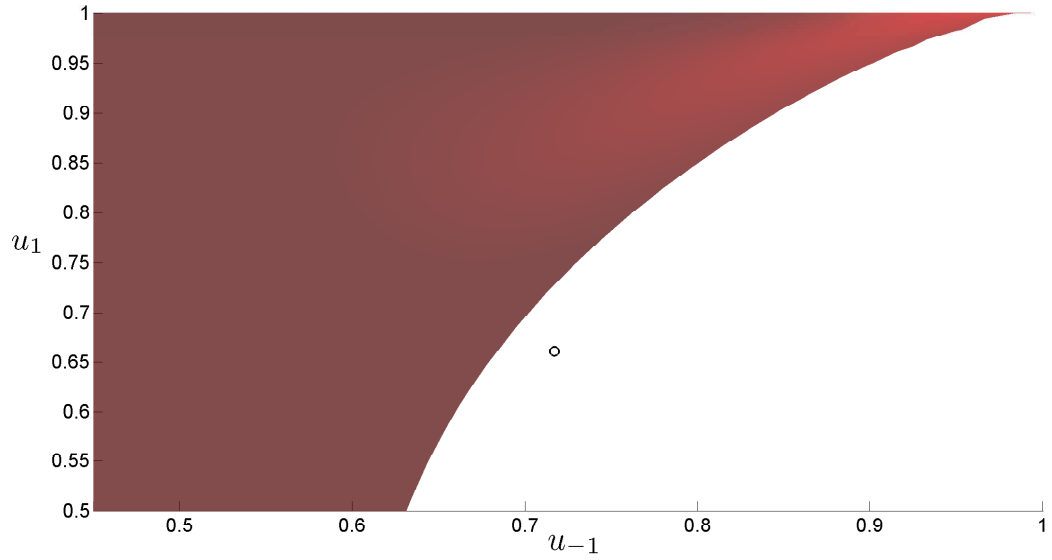

(a) $\Delta_{-}\mathcal{F} = 0$

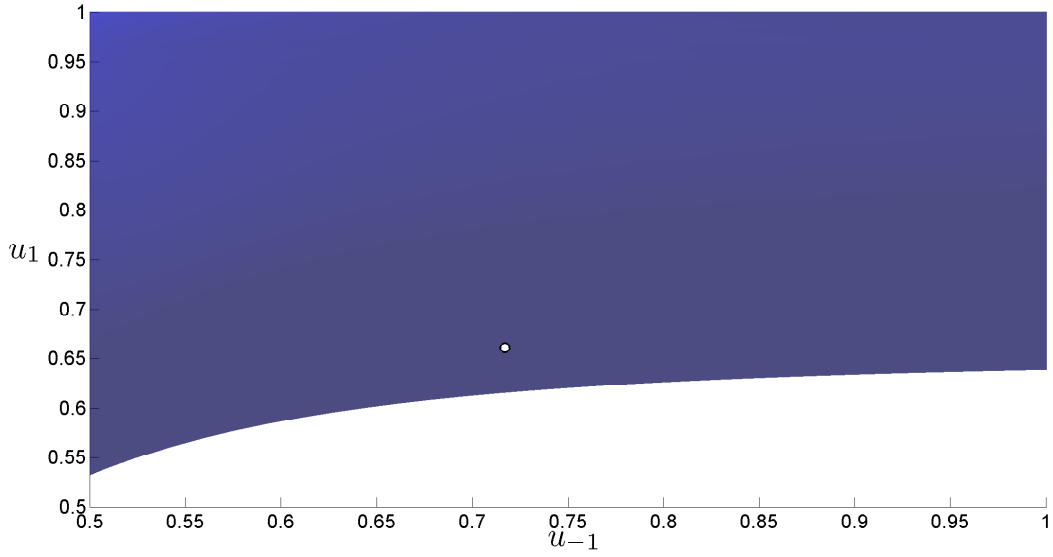

(b) $\Delta_{+}\mathcal{F} = 0$

Figure 4.5.2: Plot of $\Delta_{-}\mathcal{F} = 0$ and $\Delta_{+}\mathcal{F} = 0$ for Experiment C2 with $(A, B) = \big(\bar{\theta}_f, \theta_f\big)(\circ)$ indicated

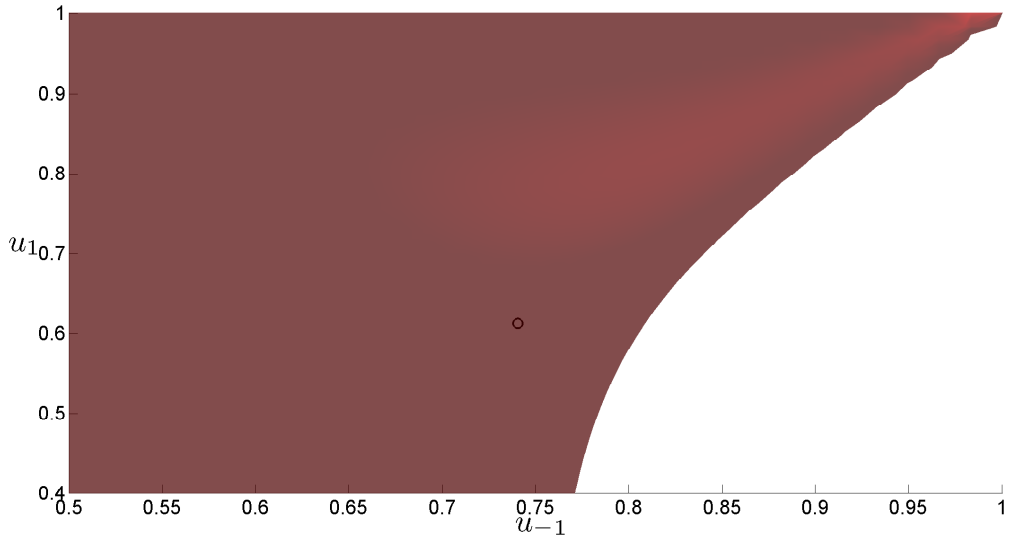

(a) $\Delta_- \mathcal{F} = 0$

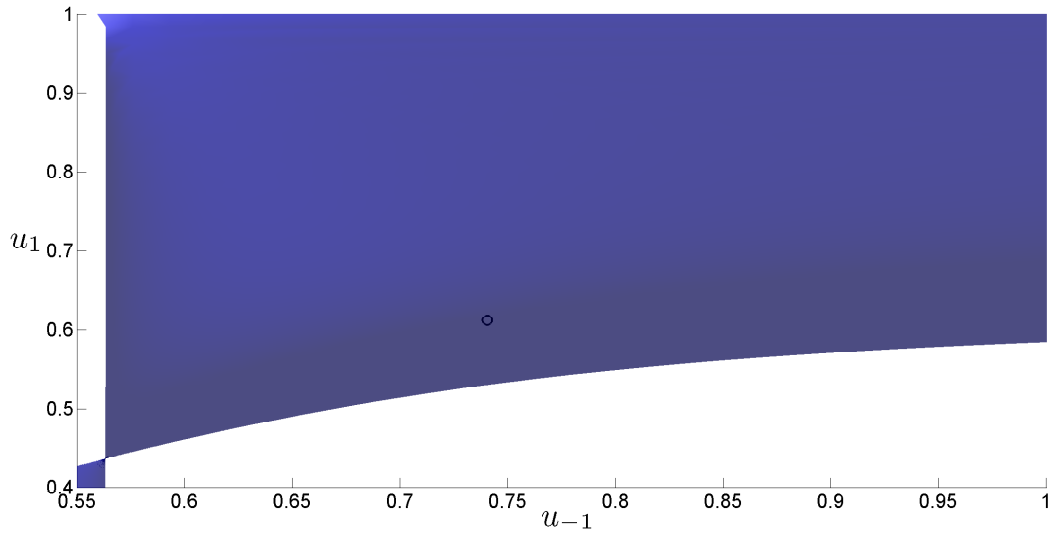

(b) $\Delta_+ \mathcal{F} = 0$

Figure 4.5.3: $\Delta_- \mathcal{F} = 0$ and $\Delta_+ \mathcal{F} = 0$ for Experiment C3 with $(A, B) = (\theta_g, \theta_f)(\circ)$ indicated

Experiment C4

In this experiment both interface entropy conditions where possible solutions at x_h, but as we see in figure 4.5.4, both $(u_{-1}, u_1) = (A_o, B_o)$ and $(u_{-1}, u_1) = (A_m, B_m)$ is not included in the area where $\Delta_- \mathcal{F} = 0$ and $\Delta_+ \mathcal{F} = 0$. The numerical solution of UM we got in experiment C4 (c.f. figure 4.4.14) was a "spike" at the left side of x_h, and an u-value almost equal to the one approximated by EO and G, on the right side. The "spike" had the value $u_{-1} \approx 0.39$ which together with $u_1 \approx B$ is enough for the approximate solution to be in the area such that $\Delta_- \mathcal{F} = 0$ and $\Delta_+ \mathcal{F} = 0$. This suggests that the solution UM approximate at x_h is the one it converges towards when $t \to \infty$. Since we have a "spike" at the left side of x_h, (4.5.5) is obviously not fulfilled.

Experiment C5

In figure 4.5.5, we again see that there is no u_{-2} such that UM can stabilize at the optimal entropy or minimal jump connection. UM approximates a "spike on the right side of x_h with the value $u_1 \approx 0.9$ and a left trace of value $u_{-1} \approx A$. As $t \to \infty$, UM seems to approximate the jump seen in figure 4.4.16 at the interface. As for Experiment C4, (4.5.5) is not fulfilled because of the "spike" in the solution.

Experiment C6

This experiment was made with a special property of the mobility functions

$$\lambda_w^L(u_\chi) = \lambda_w^R(u_\chi), \qquad \lambda_o^L(u_\chi) = \lambda_o^R(u_\chi)$$

Thus, this experiment was made such that (4.5.5) is fulfilled with $u_{-1} = u_1 = u_\chi$. Figure 4.5.6 confirms that the minimal jump solution lies within the area such that $\Delta_- \mathcal{F} = 0$ and $\Delta_+ \mathcal{F} = 0$.

Experiment C7

Here we have the same left mobility functions as the previous experiment, but now the right flux functions is lower than the left. The equality of the mobility functions at u_χ is not present here. We saw in figure 4.4.23, that the numerical solution of UM was completely different than EO and G which approximated the optimal entropy solution, and LLxF which approximated the minimal jump solution. If we look at figure 4.5.7a, we see that there is a narrow area where $\Delta_- \mathcal{F} = 0$, and (A_o, B_o) and (A_m, B_m) is not included in this area. The jump UM approximated was $(u_{-1}, u_1) \approx (0.82, 0.65)$. These traces lies within the area where $\Delta_- \mathcal{F} = 0$ and $\Delta_+ \mathcal{F} = 0$, thus, might explain why UM approximates this solution for this experiment. We check (4.5.5). Solving $\lambda_w^L(u_{-1}) = \lambda_w^R(u_1)$ and $\lambda_o^L(u_{-1}) = \lambda_o^R(u_1)$, we get $u_{-1} \approx 0.82$ and $u_1 \approx 0.65$. This is exactly the solution UM approximated, c.f. figure 4.4.23.

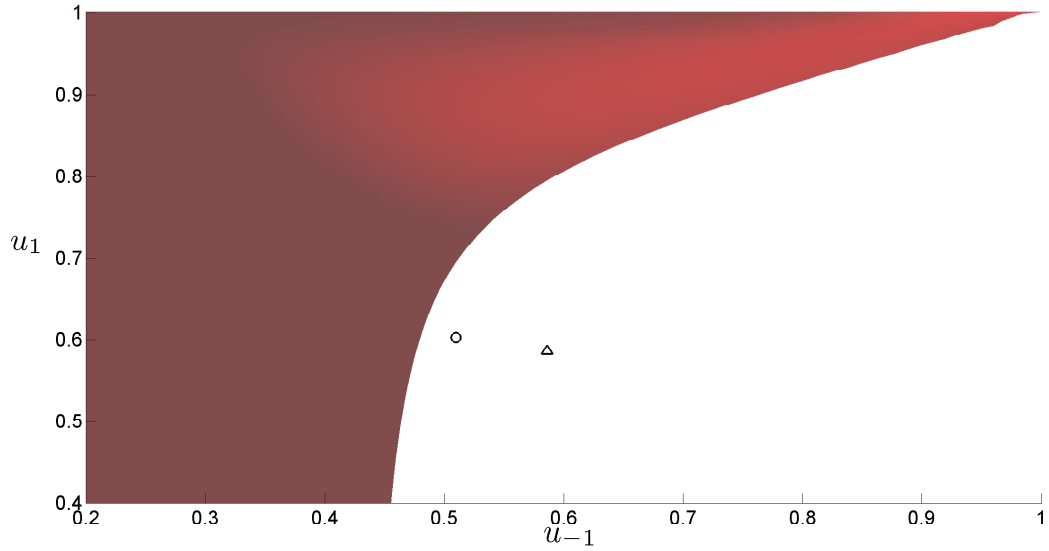

(a) $\Delta_{-}\mathcal{F} = 0$

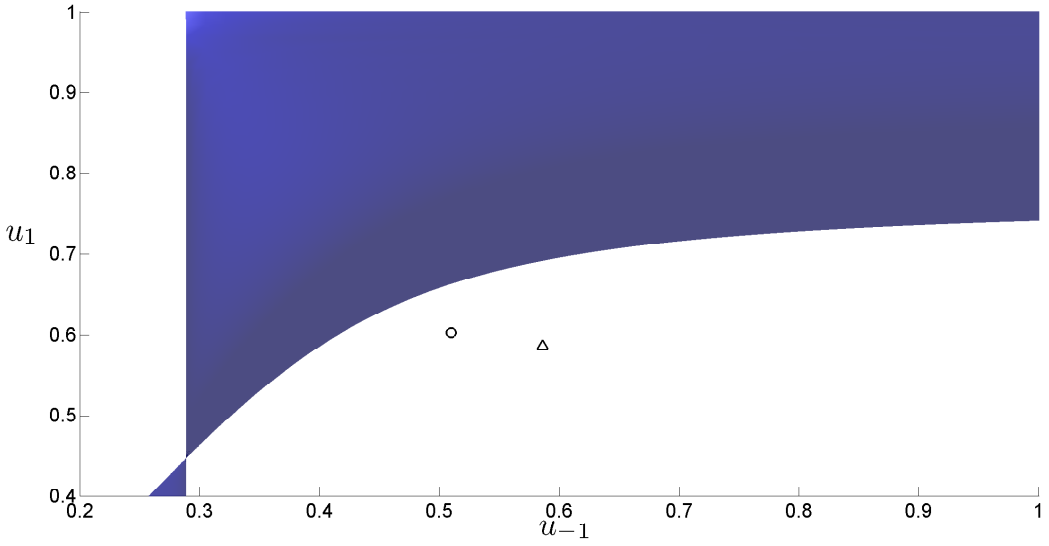

(b) $\Delta_{+}\mathcal{F} = 0$

Figure 4.5.4: $\Delta_{-}\mathcal{F} = 0$ and $\Delta_{+}\mathcal{F} = 0$ for Experiment C4 with $(A_o, B_o) = \big(\theta_g, \bar{\theta}_g\big)(\circ)$ and $(A_m, B_m) = (u_\chi, u_\chi)$ $(\triangle)$ indicated

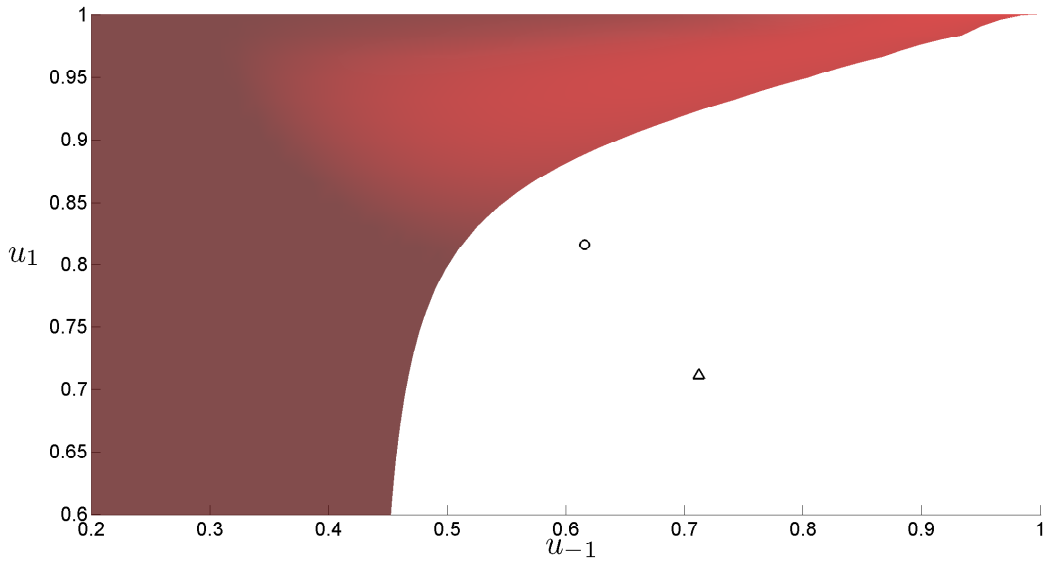

(a) $\Delta_- \mathcal{F} = 0$

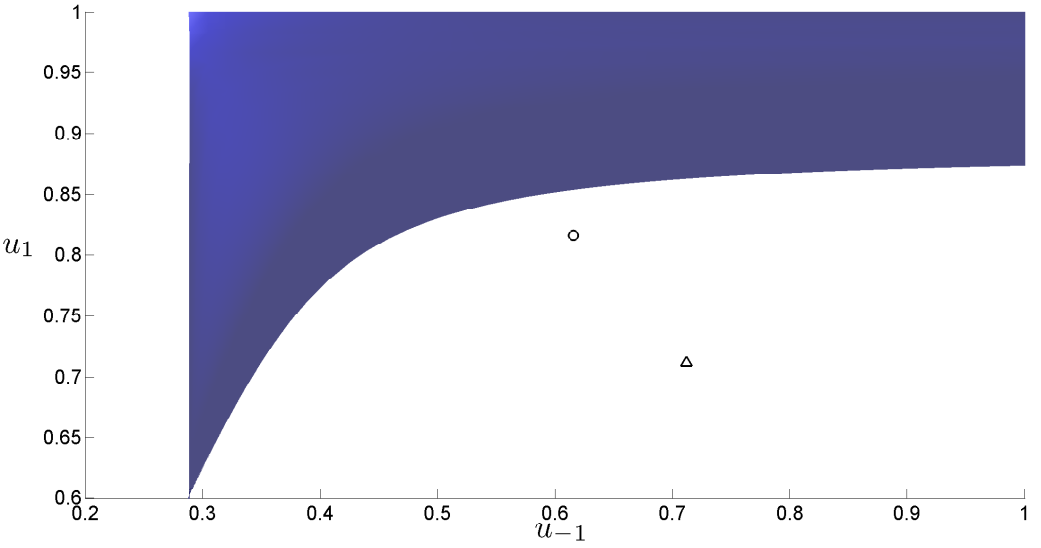

(b) $\Delta_+ \mathcal{F} = 0$

Figure 4.5.5: $\Delta_- \mathcal{F} = 0$ and $\Delta_+ \mathcal{F} = 0$ for Experiment C5 with $(A_o, B_o) = \big(\bar{\theta}_f, \theta_f\big)(\circ)$ and $(A_m, B_m) = (u_\chi, u_\chi)$ $(\triangle)$ indicated

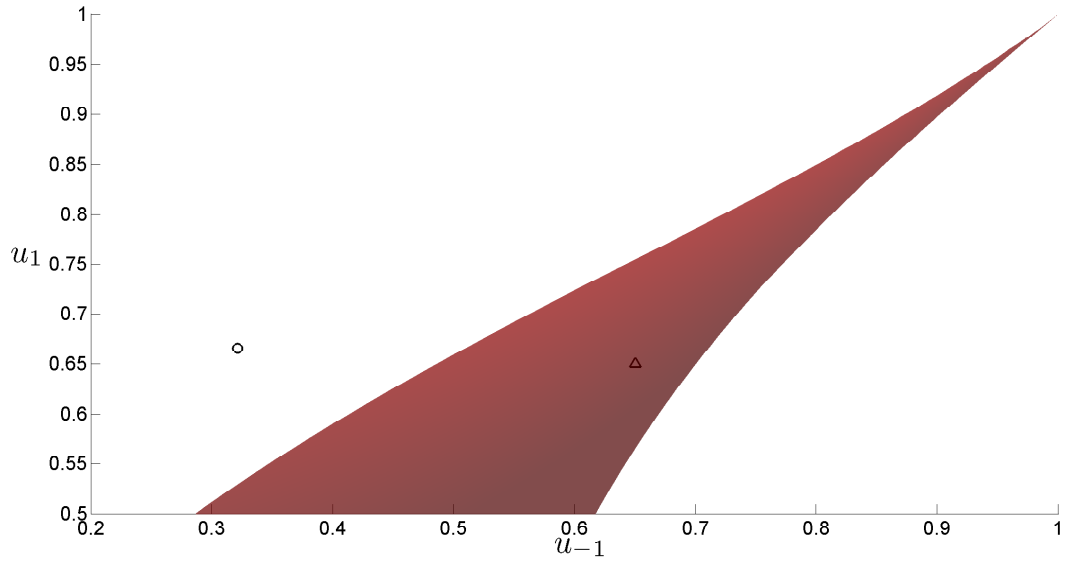

(a) $\Delta_- \mathcal{F} = 0$

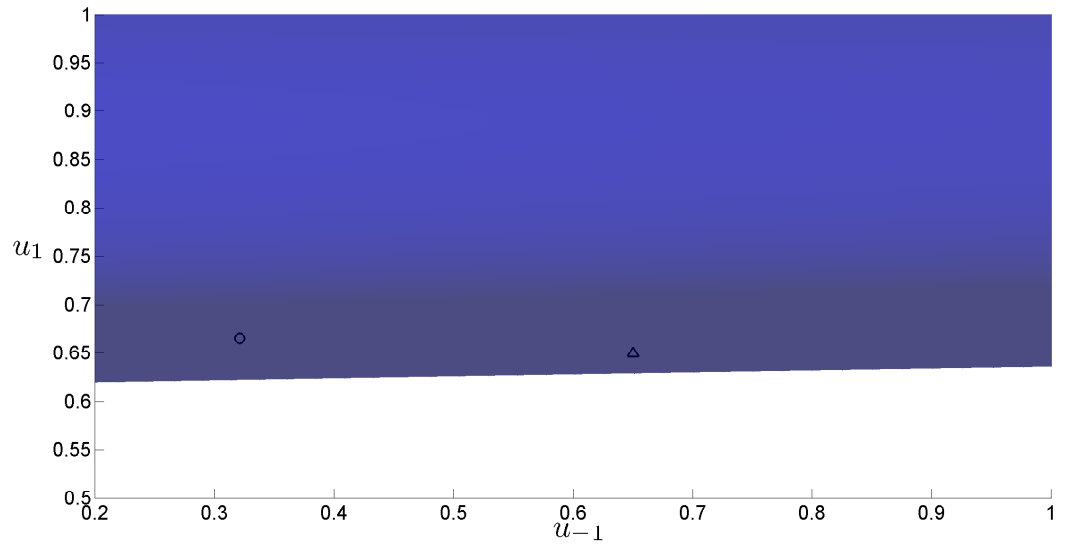

(b) $\Delta_+ \mathcal{F} = 0$

Figure 4.5.6: $\Delta_- \mathcal{F} = 0$ and $\Delta_+ \mathcal{F} = 0$ for Experiment C6 with $(A_o, B_o) = \big(\theta_g, \bar{\theta}_g\big)(\circ)$ and $(A_m, B_m) = (u_\chi, u_\chi)$ $(\triangle)$ indicated

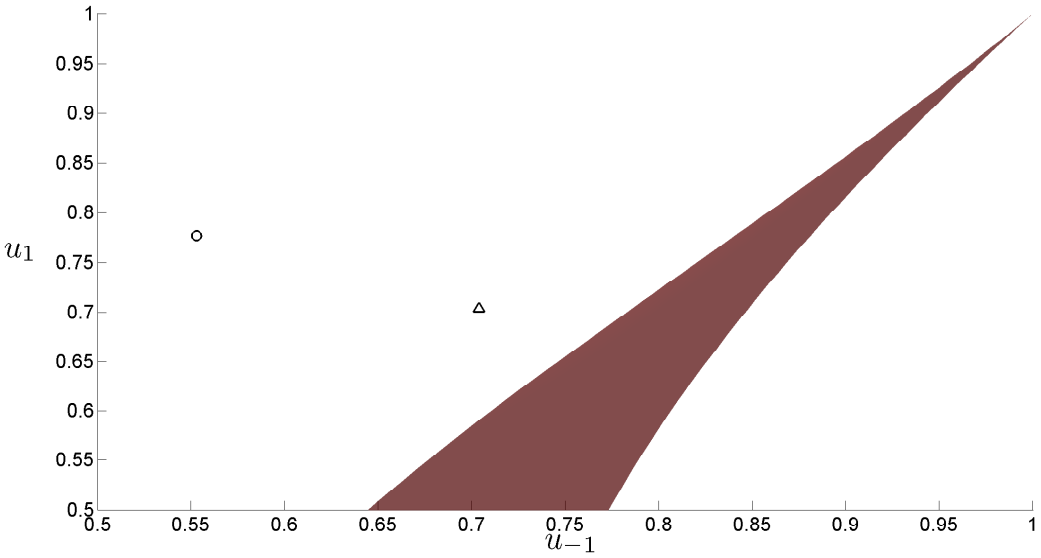

(a) $\Delta_{-}\mathcal{F} = 0$

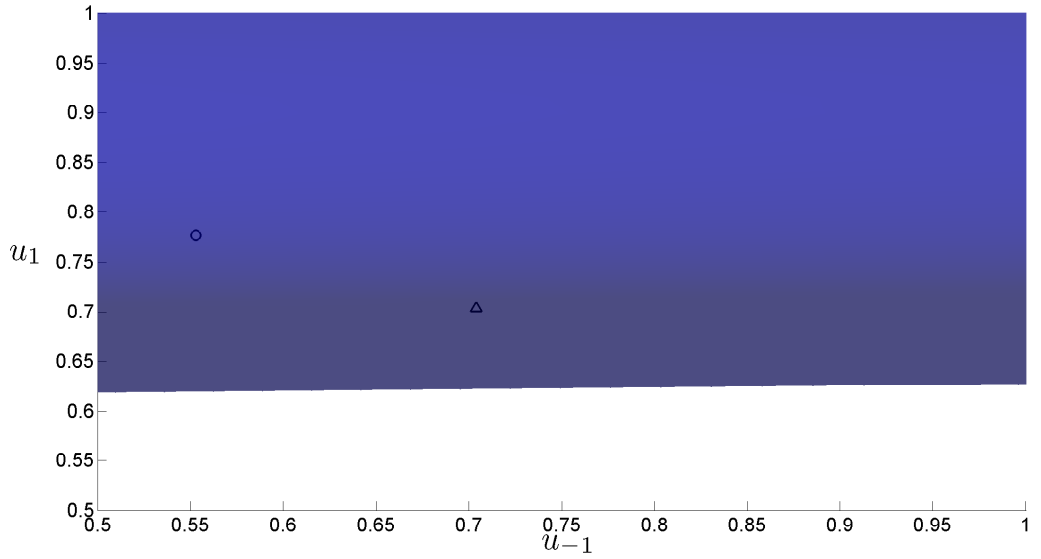

(b) $\Delta_{+}\mathcal{F} = 0$

Figure 4.5.7: $\Delta_{-}\mathcal{F} = 0$ and $\Delta_{+}\mathcal{F} = 0$ for Experiment C7 with $(A_o, B_o) = \big(\bar{\theta}_f, \theta_f\big)(\circ)$ and $(A_m, B_m) = (u_\chi, u_\chi)$ $(\triangle)$ indicated

4.6 Summary of Results

We end the numerical experiment section with a summary of the results:

- For test scenario A and B, UM approximated the same solution as both EO and G. LLxF experience some numerical dispersion, and does not resolve the interface discontinuity ($x = x_h$) as good as the other schemes.
- The first experiment (C1) in test scenario C showed that UM missed the interface discontinuity, but refinement of the grid suggested that the scheme would converge to the physically correct solution as $\Delta x \to 0$. LLxF followed EO and G, qualitatively speaking, and improved when the grid step was reduced.
- Experiment C2 showed that UM produced a "spike"-solution, which is unphysical in the sense of heterogeneous two-phase flow. Refinement of the grid did not remove the the "spike". LLxF performed similarly as for Experiment C1.
- Experiment C3 (overcompressive flux crossing) showed that UM solved the interface discontinuity well, but stabilized at a different jump from u_{-1} to u_1 than the correct (A, B)-jump, which EO and G approximated. The discussion is section 4.5 could explain why the jump was approximated differently. LLxF followed EO and G away from the interface discontinuity. At x_h, it approximates the jump with some numerical dispersion.
- Experiment C4 and C5 showed how UM solves the problem of undercompressive flux crossing, where $g(\theta_g) < f(\theta_f)$ (C4) and $g(\theta_g) > f(\theta_f)$ (C5). UM follows the solution of EO and G reasonably well, but approximates a "spike" either to the left (C4 and C5 before the left-going shock wave occurs) or to the right (C5 after the shock wave propagates leftward) of x_h. In the discussion we suggested why the (A_o, B_o) - or (A_m, B_m)-connection could not be approximated by UM. LLxF approximated the minimal jump solution in both C4 and C5.
- Experiment C6 was constructed such that $\lambda_w^L(u_\chi) = \lambda_w^R(u_\chi)$, $\lambda_o^L(u_\chi) = \lambda_o^R(u_\chi)$ and $g(\theta_g) < f(\theta_f)$. Here UM followed the minimal jump solution, together with LLxF. This results differ from C4 where the flux functions also had the property of $g(\theta_g) < f(\theta_f)$, and theoretically the solutions should have been similar.
- Experiment C7 involved the same left flux function, but now we did not have the equality of the mobility functions at the u_χ, and $g(\theta_g) > f(\theta_f)$. Here, UM approximated a different jump from u_{-1} to u_1 than the other

schemes. EO and G followed (A_o, B_o) and LLxF followed (A_m, B_m). Since this experiment can be compared to C5, we expected the UM scheme to approximate similar results. In the discussion we suggested that only a small number of left and right traces can be used at the interface.

Chapter 5

Summary and Conclusions

In this thesis we have studied numerical methods for the hyperbolic problem of conservation laws with a spatial discontinuous flux function. The methods used for the numerical approximations were Godunov's, Engquist-Osher's, Local Lax-Friedrichs' (Rusanov's) and Upstream Mobility scheme. The schemes were used to simulate Riemann problems associated with two-phase flow in porous medium, including horizontal, updip and downdip flow. The performance of the schemes were observed with emphasize on the Upstream Mobility scheme.

We presented the theory of hyperbolic conservation laws with a spatial discontinuous flux functions (Chapter 2). In the weak sense, the problem is split into two conservation laws at the discontinuity. Since discontinuities can occur in the solutions as well, entropy conditions must be met to get a unique solution. Oleinik's entropy condition from classical theory is not enough to ensure a unique solution across the interface (spatial discontinuity). The entropy condition across the interface were split into to parts: a general interface entropy condition called (A, B)-connections, and a specified (A, B)-connection based on the physical model we wanted the entropy solution for. We only looked at two such physical models: two-phase flow and clarifier thickener model. We use these models to derive and explain the different entropy solutions. In the end we saw that they only differed when the flux functions crossed in a *under-compressive manner*, i.e. $g'(u_\chi) < 0$ and $f'(u_\chi) > 0$, where u_χ is the point of intersection.

Based on the theory, the Godunov and Engquist-Osher scheme were modified to approximate the (A, B)-connections ([2, 3] and [9]). A simplified version of Godunov's method was presented from [18], and inspired by this, the same simplification was done to Engquist-Osher's method. The Local Lax-Friedrichs methods was presented as a new scheme for approximating the hyperbolic problem. Lastly, the Upstream Mobility scheme was presented with a explicit

formulation for choosing the correct upstream saturation ([5, 18]). Consistency was shown for all the schemes, and monotonicity was shown for Godunov's, Engquist-Osher's and the Upstream Mobility scheme.

From the numerical experiments (Chapter 4), we saw that the Upstream Mobility scheme approximated horizontal (Test scenario A) and updip (Test scenario B) flow with the same accuracy as Godunov's and Engquist-Osher's scheme. As anticipated, the countercurrent flow in a downdip porous medium (Test scenario C) caused problems for the Upstream Mobility scheme. The experiments showed that the scheme misses the interface discontinuity and produces a "spike"-solution (Experiments C2, C4 and C5), and approximates a different jump across the interface (Experiments C3 and C7). In Experiment C1 it follow the desired entropy solution, qualitatively speaking, but with some manipulations in the flux functions, the scheme also followed the undesired minimal jump solution (Experiment C6).
With the abovementioned solutions produced by the Upstream Mobility scheme in mind, we tried to analyze how the scheme solves the problem of countercurrent flow, and which jump across the interface discontinuity the flux terms cancel each other. From this analysis we could suggest that often, the Upstream mobility scheme could not approximate the desired (A, B)-connection for the different experiments. Hence, we could also explain the "spikes" observed in the experiment results. We can also make another interesting observation with this analysis. It seems that the scheme stabilizes at a single value to the left and right of the interface discontinuity when $\lambda_w^L(u_{-1}) = \lambda_w^R(u_1)$ and $\lambda_o^L(u_{-1}) = \lambda_o^R(u_1)$, where u_{-1} and u_1 are the last node before and first node after x_h, respectively. This observation is backed up by the results in Experiment C3, C6 and C7, which is the only experiments where the "spikes" are not present in the solution. Hence, the scheme stabilized the solution at u_{-1} on the left side of x_h and u_1 at the right side. We are careful on making $\lambda_w^L(u_{-1}) = \lambda_w^R(u_1)$ and $\lambda_o^L(u_{-1}) = \lambda_o^R(u_1)$ a condition for a stable UM solution. More analytical work on the UM scheme must be done in order to make a valid condition. The conclusions we can make, are that the UM scheme can produce results for downdip flow which seems reasonable if no knowledge on the correct solution is given, but clearly is wrong compared to the physical solution. Hence, making the scheme unreliable in this flow situation.
Mathematically speaking, the above observations and conclusions suggests to us that the Upstream mobility scheme, in general, does not satisfy the interface entropy condition as it is defined in definition 5. Instead, it seems that the numerical solution strongly depends on the mobility functions, λ_l, and thereby the flux functions.

The secondary objective of this thesis was studying the Local Lax-Friedrichs scheme. From the numerical experiments, we see that it experience much numerical dispersion, especially when approximating the interface discontinuity. It chooses the minimal jump solution when the (A, B)-entropy conditions dif-

fer. Overall, the scheme performs reasonably well, and the numerical results suggest that the scheme is monotone.

Chapter 6

Future Work

Many interesting topics can be investigated, based on the results of this thesis:

- Numerical experiments for two and three dimensions for more realistic flow situations a in porous medium. In more than one dimension, the geometry of the porous medium affects the numerical solution. Thus, the heterogeneity may have complex structures where the Upstream Mobility may have difficulties, solving the problem correctly.
- In several dimension, a coupling of the pressure equation and saturation equation must be done. Complex heterogeneities may give a singularity in the pressure equation with unknown effects on the saturation equation.
- The Local Lax-Friedrichs scheme is only tested numerically in this thesis, thus theoretical justification of the scheme must be done. Also, investigate if the scheme can be extended to include a general (A, B)-solution as done with the Godunov and Engquist-Osher scheme.

Appendix A

The Engquist-Osher scheme at the spatial discontinuity

In this appendix, we write the full expression of the interface flux, $\overline{F}_{AB}^{EO}(u_L, u_R)$. To make the derivation easier to follow, we have included figures of some $g(u)$ and $f(u)$, shown in figure A.0.1.

Consider the interface flux $\overline{F}_{AB}^{EO}$ defined in (3.3.4) for flux functions satisfying the hypothesis (H_2) (concave type fluxes), and from definition 3: $s \leq A \leq \theta_g$ and $\theta_f \leq B \leq S$. Also, recall from definition 3 that $f(B) = g(A)$ from the Rankine-Hugoniot condition, and notice in the following that we separate the formulae when the function values of f and g are above or below $f(B)$ and $g(A)$ respectively .

- $g'(u_L), f'(u_R) \geq 0$

1. $u_R < B$

$$\overline{F}_{AB}^{EO} = \tfrac{1}{2}\left[\cancel{f(u_R)} + \tilde{g}(u_L)\right] - \tfrac{1}{2}\left[\cancel{f(u_R)} - f(B) - \int_A^{u_L} |\tilde{g}'(w)|dw\right],$$

   (a) $g(u) < g(A)$

$$\overline{F}_{AB}^{EO} = \tfrac{1}{2}g(u_L) - \tfrac{1}{2}\left[-\cancel{f(B)} - g(u_L) + \cancel{g(A)}\right] = g(u_L),$$

      i. $g(u) \geq g(A)$

$$\overline{F}_{AB}^{EO} = \tfrac{1}{2}g(A) - \tfrac{1}{2}\left[-f(B)\right] = g(A),$$

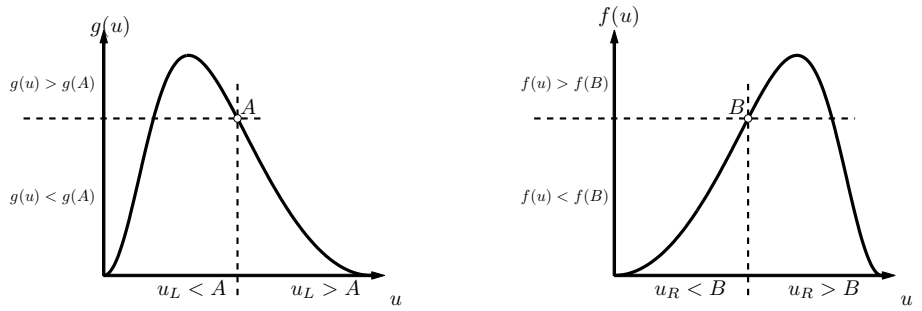

(a) Example of $g(u) \in CC(I)$ with $u = A$ and $g(u) = g(A)$ indicated for analysis purposes

(b) Example of $f(u) \in CC(I)$ with $u = B$ and $f(u) = f(B)$ indicated for analysis purposes

Figure A.0.1: An example of $g(u)$ and $f(u)$ satisfying (H_2)

(b) $u_R > B$

$$\overline{F}_{AB}^{EO} = \tfrac{1}{2}\left[f(B) + \tilde{g}(u_L)\right] - \tfrac{1}{2}\left[-\int_A^{u_L} |\tilde{g}'(w)|dw\right],$$

i. $g(u) < g(A)$

$$\overline{F}_{AB}^{EO} = \tfrac{1}{2}\left[\cancel{f(B)} + g(u_L)\right] - \tfrac{1}{2}\left[-g(u_L) + \cancel{g(A)}\right] = g(u_L),$$

ii. $g(u) \geq g(A)$

$$\overline{F}_{AB}^{EO} = \tfrac{1}{2}\left[f(B) + g(A)\right] = g(A),$$

- $g'(u_L), f'(u_R) \leq 0$

1. $u_L < A$

$$\overline{F}_{AB}^{EO} = \tfrac{1}{2}\left[g(A) + \tilde{f}(u_R)\right] - \tfrac{1}{2}\left[\int_B^{u_R} |\tilde{f}'(w)|dw\right],$$

(a) $f(u_R) < f(B)$

$$\overline{F}_{AB}^{EO} = \tfrac{1}{2}\left[\cancel{g(A)} + f(u_R)\right] - \tfrac{1}{2}\left[\cancel{f(B)} - f(u_R)\right] = f(u_R),$$

(b) $f(u_R) \geq f(B)$

$$\overline{F}_{AB}^{EO} = \tfrac{1}{2}\left[g(A) + f(B)\right] = f(B),$$

2. $u_L > A$

$$\overline{F}_{AB}^{EO} = \tfrac{1}{2}\left[\cancel{g(u_L)} + \tilde{f}(u_R)\right] - \tfrac{1}{2}\left[\cancel{g(u_L)} - g(A) + \int_B^{u_R} |\tilde{f}'(w)|dw\right],$$

(a) $f(u_R) < f(B)$

$$\overline{F}_{AB}^{EO} = \tfrac{1}{2} f(u_R) - \tfrac{1}{2}\left[\cancel{f(B)} - f(u_R) - \cancel{g(A)}\right] = f(u_R),$$

(b) $f(u_R) \geq f(B)$

$$\overline{F}_{AB}^{EO} = \tfrac{1}{2}\left[g(A) + f(B)\right] = f(B),$$

- $g'(u_L) \geq 0\,,\ f'(u_R) \leq 0$

1. $g(u_L) < g(A)\,,\ f(u_R) < f(B)$

$$\begin{aligned}\overline{F}_{AB}^{EO} &= \frac{1}{2}\left[g(u_L) + f(u_R)\right] - \frac{1}{2}\left[g(A) - g(u_L) + f(B) - f(u_R)\right] \\ &= g(u_L) + f(u_R) - g(A),\end{aligned}$$

2. $g(u_L) < g(A)\,,\ f(u_R) \geq f(B)$

$$\overline{F}_{AB}^{EO} = \tfrac{1}{2}\left[g(u_L) + f(B)\right] - \tfrac{1}{2}\left[g(A) - g(u_L)\right] = g(u_L),$$

3. $g(u_L) \geq g(A)\,,\ f(u_R) < f(B)$

$$\overline{F}_{AB}^{EO} = \tfrac{1}{2}\left[g(A) + f(u_R)\right] - \tfrac{1}{2}\left[f(B) - f(u_R)\right] = f(u_R),$$

4. $g(u_L) \geq g(A)\,,\ f(u_R) \geq f(B)$

$$\overline{F}_{AB}^{EO} = \tfrac{1}{2}\left[g(A) + f(B)\right] = g(A),$$

- $g'(u_L) \leq 0\,,\ f'(u_R) \geq 0$

1. $u_R < B\,,\ u_L < A$

$$\overline{F}_{AB}^{EO} = \tfrac{1}{2}\left[g(A) + f(u_R)\right] - \tfrac{1}{2}\left[f(u_R) - f(B)\right] = g(A),$$

2. $u_R < B\,,\ u_L > A$

$$\overline{F}_{AB}^{EO} = \tfrac{1}{2}\left[g(u_L) + f(u_R)\right] - \tfrac{1}{2}\left[f(u_R) - f(B) + g(u_L) - g(A)\right] = g(A),$$

3. $u_R > B$, $u_L < A$

   $\overline{F}^{EO}_{AB} = \frac{1}{2}\left[g(A) + f(B)\right] = g(A),$

4. $u_R > B$, $u_L > A$

   $\overline{F}^{EO}_{AB} = \frac{1}{2}\left[g(u_L) + f(B)\right] = g(A),$

Bibliography

[1] I. Aavatsmark, *Bevarelsesmetoder for Hyperbolske Differensialligninger*, Department of Mathematics, University of Bergen, 2004. Lecture notes in Norwegian.

[2] Adimurthi, J. Jaffré, and G. Gowda, *Godunov-Type Methods for Conservation Laws with a Flux Function Discontinuous in Space*, SIAM Journal on Numerical Analysis, 42 (2004), p. 179.

[3] Adimurthi, S. Mishra, and G. D. Veerappa Gowda, *Optimal Entropy Solutions for Conservation Laws with Discontinuous Flux-Functions*, Journal of Hyperbolic Differential Equations, 2 (2005), pp. 783–837.

[4] Adimurthi and G. D. Veerappa Gowda, *Conservation Laws with Discontinuous Flux*, J. Math. Kyoto Univ., 43 (2003), pp. 27–70.

[5] Y. Brenier and J. Jaffré, *Upstream Differencing for Multiphase Flow in Reservoir Simulation*, SIAM Journal on Numerical Analysis, 28 (1991), pp. 685–696.

[6] R. Brooks and A. Corey, *Hydraulic Properties of Porous Media*, Hydrology Papers, Colorado State University, (1964).

[7] R. Bürger, K. Karlsen, C. Klingenberg, and N. Risebro, *A Front Tracking Approach to a Model of Continuous Sedimentation in Ideal Clarifier-Thickener Units*, Nonlinear Analysis: Real World Applications, 4 (2003), pp. 457–481.

[8] R. Bürger, K. Karlsen, H. Torres, and J. Towers, *Second-Order Schemes for Conservation Laws with Discontinuous Flux Modelling Clarifier-Thickener Units*, Numerische Mathematik, pp. 1–39.

[9] R. Bürger, K. Karlsen, and J. Towers, *An Engquist-Osher-Type Scheme for Conservation Laws with Discontinuous Flux Adapted to Flux Connections*, Siam J. Numer. Anal, 47 (2009), pp. 1684–1712.

[10] T. Gimse and N. Risebro, *Riemann Problems with a Discontinuous Flux Function*, in Proc. 3rd Internat. Conf. Hyperbolic problems Studentlitteratur, Uppsala, 1991, pp. 488–502.

[11] ——, *Solution of the Cauchy Problem for a Conservation Law with a Discontinuous Flux Function*, SIAM Journal on Mathematical Analysis, 23 (1992), p. 635.

[12] E. F. Kaasschieter, *Solving the Buckley-Leverett Equation with Gravity in a Heterogeneous Porous Medium*, Comput. Geosci, 3 (1999), pp. 23–48.

[13] S. Kružkov, *First Order Quasilinear Equations in Several Independent Variables*, Sbornik: Mathematics, 10 (1970), pp. 217–243.

[14] A. Kurganov and E. Tadmor, *New High-resolution Central Schemes for Nonlinear Conservation Laws and Convection-Diffusion Equations*, Journal of Computational Physics, 160 (2000), pp. 241–282.

[15] G. Kynch, *A Theory of Sedimentation*, Transactions of the Faraday society, 48 (1952), pp. 166–176.

[16] P. Lax and B. Wendroff, *Systems of Conservation Laws*, Communications on Pure and Applied Mathematics, 13 (1960), pp. 217–237.

[17] R. LeVeque, *Finite volume Methods for Hyperbolic Problems*, Cambridge Univ Pr, 2002.

[18] S. Mishra and J. Jaffré, *On the Upstream Mobility Scheme for Two-phase Flow in Porous Media*, Computational Geosciences, 14 (2010), pp. 105–124.

[19] S. Osher, *Riemann Solvers, the Entropy Condition, and Difference Approximations*, SIAM Journal on Numerical Analysis, 21 (1984), pp. 217–235.

[20] Ø. Pettersen, *Grunnkurs i Reservoarmekanikk*, Department of Mathematics, University of Bergen, 1990. Lecture notes in Norwegian.

[21] V. Rusanov, *Calculation of Interaction of Non-Steady Shock Waves with Obstacles*, Vychislitel'noi Mathematicheskoi Fiziki, 1 (1961), pp. 267–279.

[22] P. Sammon, *An Analysis of Upstream Differencing*, SPE Reservoir Engineering, 3 (1988), pp. 1053–1056.

[23] E. Tadmor, *Numerical Viscosity and the Entropy Condition for Conservative Difference Schemes*, Mathematics of Computation, 43 (1984), pp. pp. 369–381.

[24] B. Temple, *Global Solution of the Cauchy Problem for a Class of 2×2 Nonstrictly Hyperbolic Conservation Laws*, Adv. in Appl. Math, 3 (1982), pp. 335–375.